TECHNISCHE UNIVERSITÄT WIEN
Vienna | Austria

ivoclar

DIPLOMA THESIS

Synthesis and evaluation of novel MAPO-based photoinitiators

Performed at

Institute of Applied Synthetic Chemistry

TU Wien

IAS
Institute of Applied Synthetic Chemistry

under the supervision of

Univ. Prof. Dipl.-Ing. Dr. techn. Robert Liska

Senior Scientist Dipl.-Ing. Dr.techn. Patrick Knaack

by

Jelena NIKOLIC, BSc

01528556

_____

Jelena Nikolic, BSc

Danksagung

Zuerst möchte ich mich bei **Univ. Prof. Dr. Robert Liska** bedanken, dass ich meine Diplomarbeit in der Forschungsgruppe „Makromolekulare Chemie“ am Institut für angewandte Synthesechemie durchführen durfte. Vielen Dank Robert, für die interessante Themenstellung, für die hervorragende Betreuung und Unterstützung während der gesamten Diplomarbeit. Die Arbeit am Projekt mit der Firma Ivoclar Vivadent, bei der ich mich ebenfalls bedanken möchte, hat mein Interesse an der Polymerchemie zusätzlich vertieft. Besonders hervorzuheben ist auch die angenehme und offene Arbeitsatmosphäre, auf die Du immer großen Wert legst. Vielen Dank!

Ein besonderer Dank gilt auch **Dr. Patrick Knaack.** Danke dass du als direkte Betreuer meiner Diplomarbeit mir immer mit gutem Rat zur Seite gestanden bist. Danke, dass du dir immer Zeit genommen hast, um mich zuzuhören und mit deinen Ideen meine Arbeit in die richtige Richtung getrieben hast.

Bei **Dipl.-Ing. Stefan Helfert** möchte ich mich für die Betreuung während meine Bachelorarbeit bedanken. Du hast mir das spannende Gebiet der Polymerchemie gezeigt.

Vielen Dank möchte ich auch **Dipl.-Ing. David Bassenheim** aussprechen, der mir beim Einstieg in die Thematik meiner Diplomarbeit eine große Hilfe war. Danke für deine tolle Ideen, Ratschläge als auch deine Hilfe bei den praktischen Durchführungen.

Zusätzlich möchte ich mich an alle **Mitglieder der FBMC** bedanken. Danke für das tolle Arbeitsklima, für eure wertvolle Ratschläge und Engagement. Ein besonderer Dank gilt auch **Selina** und **Kaja**, die als meine direkte Laborkolleginnen immer mit Rat und Tat zur Seite standen und den Arbeitsalltag im Labor bereichert haben. Ich freue mich auch in Zukunft mit euch als Laborkolleginnen Zeit zu verbringen.

Am Ende möchte ich mich bei meiner Familie bedanken. An erste Stelle möchte ich mich bei meinen Eltern **Bojan** und **Biljana** bedanken. Danke an erste Stelle, dass Sie mir ermöglicht haben in Wien meine Chemieinteresse zu erweitern, danke dass ihr immer an mich geglaubt habt und danke für die nie endende Unterstützung. Ich möchte mich auch bei meinen Schwestern **Olivera** und **Ivana** bedanken, die mich immer motiviert, unterstützt und zum Lachen gebracht haben. Hvala!

Abstract

For very long, amalgam was the material of choice when it comes to dental restoratives. However, because of its greyish color and health concerns the research focuses on developing of suitable alternatives. Because of their superior aesthetic appearance, photopolymerizable composites are in the focus of the research as the new dental restoratives of choice.

In the photopolymerizable formulations, photoinitiators play a crucial role because they directly influence the final properties of the polymerized product. The requirement for the photoinitiators is therefore high reactivity, good compatibility, and solubility in formulations, as well as low toxicity, and no yellowing.

Acylphosphine oxides represent promising Type I photoinitiators that can be applied in dentistry. These photoinitiators are highly efficient, show long wavelength absorption and excellent bleaching behavior. Typically, they show an absorption maximum at 350 to 380 nm with tailing to 420 nm. Because of these properties, they are widely used in industrial coatings, especially for the curing of thick and highly pigmented formulations, including white coatings. The commercially available und well-established monoacylphosphine oxide MAPOs are TPO (2,4,6-trimethylbenzoyldiphenylphosphine oxide) and TPO-L (ethyl(2,4,6-trimethylbenzoyl) phenylphosphinate).

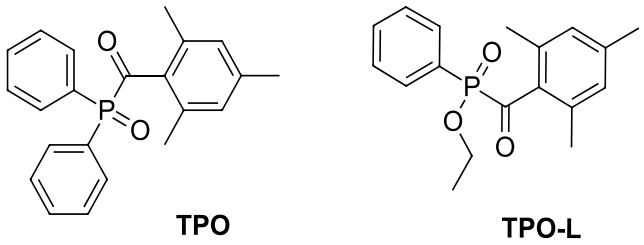

2,4,6-Trimethylbenzoyldiphenyl phosphine oxide (TPO) and Ethyl (2,4,6-trimethylbenzoyl)phenylphosphinate (TPO-L).

TPO shows high efficiency and degree of conversion, however it has some drawbacks like higher migration ratio and absorption maximum that is not compatible with the currently used dental lamps. Furthermore, the toxicity of TPO makes it unsuitable for clinical applications. TPO-L on the other hand, shows much lower toxicity, excellent color stability, however, has a lower efficiency than TPO. Therefore, the current

research focuses on developing new MAPO derivatives that would have an improved absorption behavior, lower migration ratio and better biocompatibility than TPO and TPO-L.

In this work, we focused on synthesis of new MAPO derivatives, that would preferably have an improved efficiency and absorption capabilities than the established MAPO photoinitiators TPO and TPO-L. The current research mainly focuses on the development of new MAPO derivatives through modification of acyl side of the MAPO molecule. In this work, we focused on the synthesis of new MAPO derivatives with modified phosphonyl side of the molecule. Since the phosphonyl radical shows a higher reactivity when compared to benzoyl radical, generated from α-cleavage, the modifications of phosphonyl side of the molecule can influence the overall efficiency of photoinitiators. Furthermore, responsible for the bathochromic shift in MAPO molecules is the nπ*-transition caused by interaction between the empty d-orbital of phosphorus and π*-orbital of carbonyl-carbon atom. The incorporation of heteroatoms that can interact with the d-orbital of phosphorus, can significantly influence the absorption spectra of photoinitiators. To investigate these influences, we focused on the synthesis of new derivatives with heteroatoms that have a higher electronegativity than phosphorus. For this purpose, synthesis of new MAPOs modified with amines, thiols, selenols, phosphines, sterically hindered alcohols, isocyanates and pseudohalides was performed.

For the synthesis of new photoinitiators, two approaches were investigated: the nucleophilic and electrophilic.

For the nucleophilic reactions, a simple literature known method was used, which enables the synthesis of a wide range of hetero-substituted MAPOs with different electronic structure than carbon-substituted MAPOs.

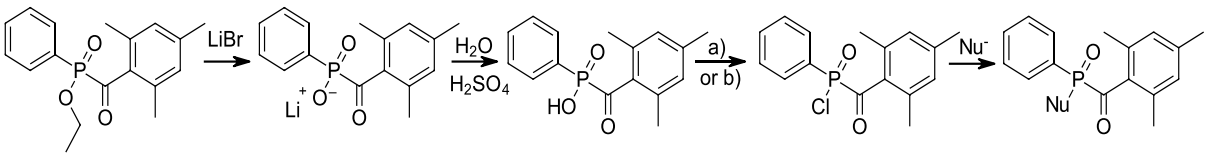

General method for the nucleophilic reactions

a) oxalyl chloride b) thionyl chloride

The electrophilic reactions were performed from mesitoylhydrogenphosphane as starting material which was reacted with the corresponding electrophile and oxidated to give the final hetero-substituted MAPO molecule.

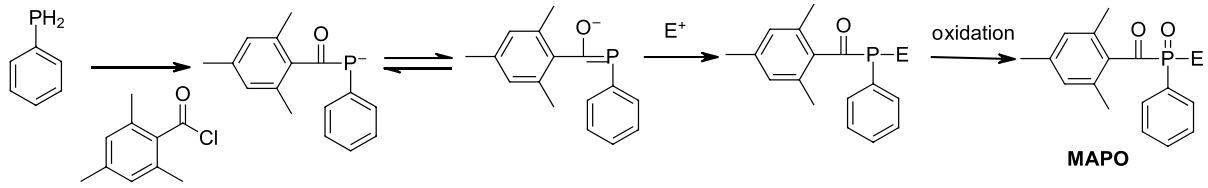

General method for the electrophilic reactions

The obtained MAPO molecules were characterized using UV-Vis spectroscopy and their performance and efficiency examined by photo-DSC.

Kurzfassung

Amalgam war lange Zeit das Material der Wahl in der Zahnmedizin. Aufgrund seiner grauen Farbe und gesundheitlichen Bedenken konzentriert sich die Forschung jedoch darauf, geeignete Alternativen zu entwickeln. Aufgrund ihres ästhetischen Erscheinungsbilds stehen photopolymerisierbare Komposite im Fokus der Forschung als die neuen bevorzugten zahnärztlichen Restaurationsmaterialien.

In den photopolymerisierbaren Formulierungen spielen Photoinitiatoren eine entscheidende Rolle, da sie direkt die endgültigen Eigenschaften des polymerisierten Produkts beeinflussen. Die Anforderungen an die Photoinitiatoren sind daher eine hohe Reaktivität, gute Verträglichkeit und Löslichkeit in den Formulierungen sowie geringe Toxizität und keine Gelbfärbung.

Acylphosphinoxide stellen vielversprechende Typ-I-Photoinitiatoren dar, die in der Zahnmedizin eingesetzt werden können. Diese Photoinitiatoren sind sehr effizient, zeigen Absorption im langwelligen Bereich und ausgezeichnetes Bleichverhalten. Typischerweise weisen sie ein Absorptionsmaximum im Bereich von 350 bis 380 nm auf, mit einem Abfall bis zu 420 nm. Aufgrund dieser Eigenschaften werden sie weitgehend in industriellen Beschichtungen verwendet, insbesondere für die Aushärtung von dickflüssigen und stark pigmentierten Formulierungen, einschließlich weißer Beschichtungen. Die kommerziell erhältlichen und etablierten Monoacylphosphinoxide (MAPOs) sind 2,4,6-Trimethylbenzoyldiphenylphosphinoxid (TPO) und Ethyl(2,4,6-trimethylbenzoyl) phenylphosphinat (TPO-L).

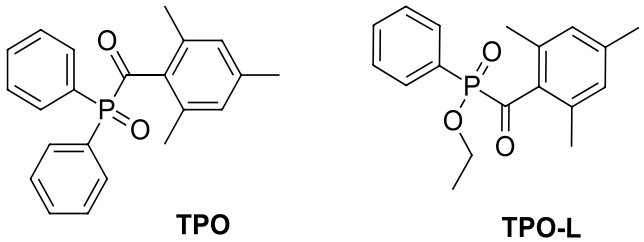

TPO **TPO-L**

2,4,6-Trimethylbenzoyldiphenylphosphinoxid (TPO) and Ethyl (2,4,6-trimethylbenzoyl)phenylphosphinat (TPO-L).

TPO zeigt eine hohe Effizienz, hat jedoch einige Nachteile wie ein höheres Migrationsverhältnis und ein Absorptionsmaximum, das nicht mit den derzeit verwendeten Zahnarztlampen kompatibel ist. Darüber hinaus macht die Toxizität von TPO es für klinische Anwendungen ungeeignet. TPO-L hingegen zeigt eine deutlich

geringere Toxizität, eine ausgezeichnete Farbstabilität, hat jedoch eine geringere Effizienz als TPO. Daher konzentriert sich die aktuelle Forschung darauf, neue MAPO-Derivate zu entwickeln, die ein verbessertes Absorptionsverhalten, ein geringeres Migrationsverhältnis und eine bessere Biokompatibilität als TPO und TPO-L aufweisen würden.

In dieser Arbeit haben wir uns darauf konzentriert, neue MAPO-Derivate zu synthetisieren, die idealerweise eine verbesserte Effizienz und Absorptionsfähigkeiten im Vergleich zu den etablierten MAPO-Photoinitiatoren TPO und TPO-L aufweisen würden. Die aktuelle Forschung konzentriert sich hauptsächlich auf die Entwicklung neuer MAPO-Derivate durch Modifikation der Acyl-Seite des MAPO-Moleküls. In dieser Arbeit haben wir uns auf der Synthese neuer MAPO-Derivate mit modifizierter Phosphonyl-Seite des Moleküls fokussiert. Da das Phosphonyl-Radikal im Vergleich zum Benzyl-Radikal, das durch α-Spaltung erzeugt wird, eine höhere Reaktivität zeigt, können Modifikationen an der Phosphonyl-Seite des Moleküls die Gesamteffizienz der Photoinitiatoren beeinflussen. Darüber hinaus ist für den bathochromen Shift in MAPO-Molekülen der nπ*-Übergang verantwortlich, der durch die Wechselwirkung zwischen dem leeren d-Orbital von Phosphor und dem π*-Orbital des Carbonyl-Kohlenstoffatoms verursacht wird. Die Einbindung von Heteroatomen, die mit dem d-Orbital von Phosphor wechselwirken können, kann die Absorptionsspektren von Photoinitiatoren signifikant beeinflussen. Um diese Einflüsse zu untersuchen, konzentrierten wir uns auf die Synthese neuer Derivate mit Heteroatomen, die eine höhere Elektronegativität als Phosphor aufweisen. Zu diesem Zweck wurde die Synthese neuer MAPOs mit Aminen, Thiolen, Selenolen, Phosphinen, sterisch gehinderten Alkoholen, Isocyanaten und Pseudohalogeniden durchgeführt.

Für die Herstellung neuer Photoinitiatoren wurden zwei Synthesestrategien untersucht: die nukleophile und die elektrophile Methode.

Für die nukleophilen Reaktionen wurde eine einfache, in der Literatur bekannte Methode verwendet. Mit dieser Methode können verschiedene hetero-substituierte MAPO-Moleküle hergestellt werden, die eine unterschiedliche elektronische Struktur als kohlenstoffsubstituierte MAPOs aufweisen.

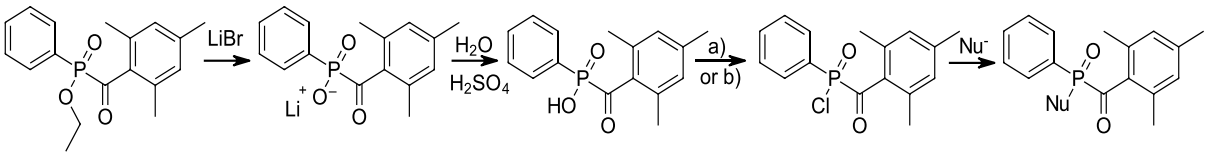

Allgemeine Synthesestrategie für nucleophile Reaktionen

Die elektrophilen Reaktionen wurden von Mesitoylhydrogenphosphan als Ausgangsmaterial durchgeführt, das mit dem entsprechenden Elektrophil umgesetzt wurde. Anschließend, um das endgültige hetero-substituierte MAPO-Molekül zu erhalten, das Zwischenprodukt wurde oxidiert.

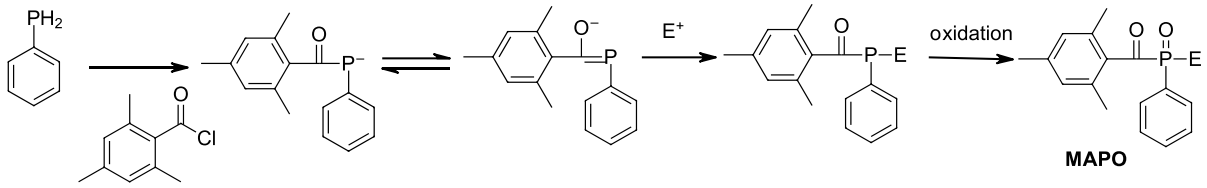

Allgemeine Synthesestrategie für elektrophile Reaktionen

Die erhaltenen MAPO-Moleküle wurden mittels UV-Vis-Spektroskopie charakterisiert, und ihre Leistung und Effizienz wurden durch Photo-DSC untersucht.

TABLE OF CONTENTS

INTRODUCTION

Despite considerable promotion of dental health and success in preventing dental caries, oral health remains a major global health problem. Therefore, there is an increasing interest in better treatment of oral health issues.[1] Over the last 200 years, the material of choice for dental fillings was amalgam.[2] Dental amalgam is a mercury alloy consisting of about 50 % mercury and other metals such as silver and smaller amounts of copper, tin, or zinc.[2] The first concerns about the health and environmental aspects of amalgam fillings started rising in the middle of the 19th century.[2] However, back then the analytical data about the released amounts of neurotoxic mercury in the human body were not available since the more sensitive analytic techniques were still underdeveloped.[2] Therefore, the concern about the possible health hazards of amalgam fillings has intensified over the last 25 years.[2] For this purpose, global organizations such as the World Health Organization (WHO) and the United Nations Environment Program (UNEP) have started the investigation of possible ways to reduce the risks from the use and release of mercury to human health and the environment.[1] The reached agreement of the so-called “phase-down” should lead to an enhanced shift from amalgam fillings to alternative dental restoratives.[1]

The tooth decay starts with the formation of a small hole in the outer tooth layer called enamel.[3] The enamel is the hardest tissue in the human body, it consists of almost 100 % inorganic material and its main purpose is the protection of the tooth from external influences.[3,4] However, when the decay passes the hard enamel and reaches a much softer underlayer, the so-called dentin, decay proceeds further much faster. The reason for this is that dentin consists in difference to enamel in some part of organic materials e.g., collagen and fluids located in microscopic channels called dentinal tubules.[3,4] Therefore, in a dental restoration, the dental filling should narrow the natural tooth substance as much as possible and should fulfill the following characteristics[4]

- High stability in acidic environments
- Remarkable mechanical characteristics in terms of both hardness and toughness for long-term durability
- Full covering of the cavity to prevent bacterial contamination.

- Low abrasion to maintain the shape of the filling.
- Easy and fast processing
- Optical resemblance to natural tooth substance
- Biocompatibility
- Low cost

Although amalgam fulfills most of these requirements, especially when it comes to its processability, mechanical properties, longevity, and price, its setbacks such as biocompatibility and dark grey color have given rise to some new alternative dental filling materials. Some of the newly developed materials are groceries (organically modified ceramics), glass ionomer types of cement, polymer-modified glass ionomer cement, dental compomers, and dental composites.[4]

Dental composites are materials that consist of a mixture of inorganic fillers and organic matrix.[5] The inorganic filler materials are responsible for the enhanced mechanical properties of the composites and are mainly composed of grinded glasses and micro fillers such as highly dispersed silicon dioxide and hybrid materials. [5] The organic matrix, on the other hand, consists of polymer networks, based mostly on dimethacrylate which can form the three-dimensional networks through free radical polymerization.[5] The methacrylate matrix usually consists of monomers like urethane dimethacrylate (UDMA), decanediol dimethacrylate (D_3MA), and bisphenol A diglycidylmethacrylate (bis-GMA) represented in following Scheme 1.

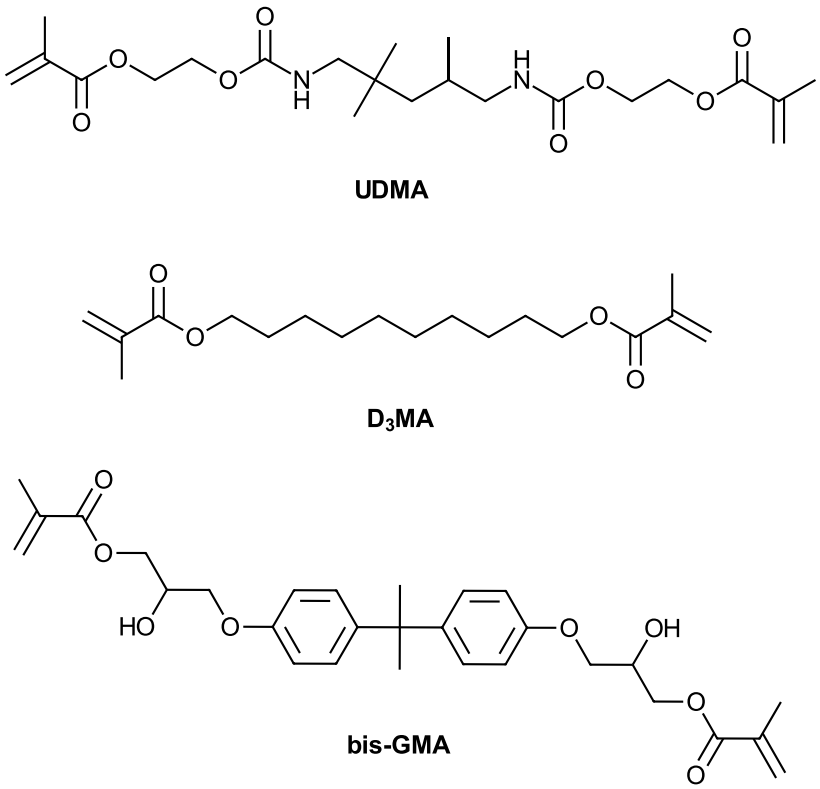

Scheme 1: Common monomers used in dental composites.

The choice of monomer plays a very important role since it defines the viscosity and shrinkage of the system. Therefore, by choosing the correct components of the matrix, the reactivity, mechanical properties, and biocompatibility of the final material can be optimized.[6]

Usually, the hardening of these formulations is performed via light-induced radical polymerization (photopolymerization), which represents one of the fastest-growing polymerization processes, as it presents several advantages including solvent-free working, high curing speed, better mechanical properties of the photocured products, and low energy costs.[7,8] Besides monomers, for the photopolymerization of the formulations, photoinitiators play a key role. The photoinitiators are molecules that can absorb the energy of a photon either directly or indirectly (by photosensitizer) and transform it into chemical energy.[7,9]

After the formation, the radicals can either start the chain reaction, recombine, or lead to the termination and chain transfer reactions. The first step of the chain reaction is the addition of the initiating radical to the monomer (Scheme 2).

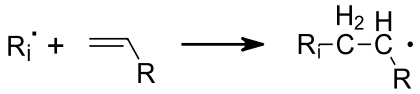

Scheme 2: Start of the chain reaction (R_i – initiator radical)

In the second step of the reaction, propagation, new monomers can be added to the growing polymer chain radical leading to the increase of the chain length. The monomer's addition can occur following the 1,3-addition mechanism (a preferred mechanism) or 1,2-addition. (Scheme 3)

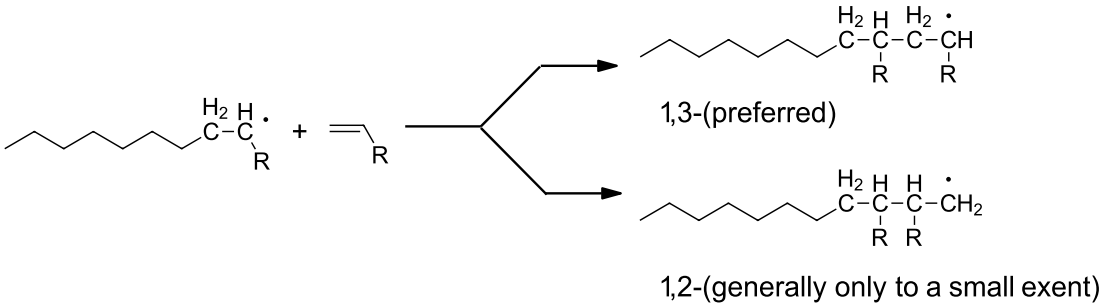

Scheme 3: Propagation mechanism

Two different termination mechanisms can occur recombination or disproportionation. (Scheme 4)

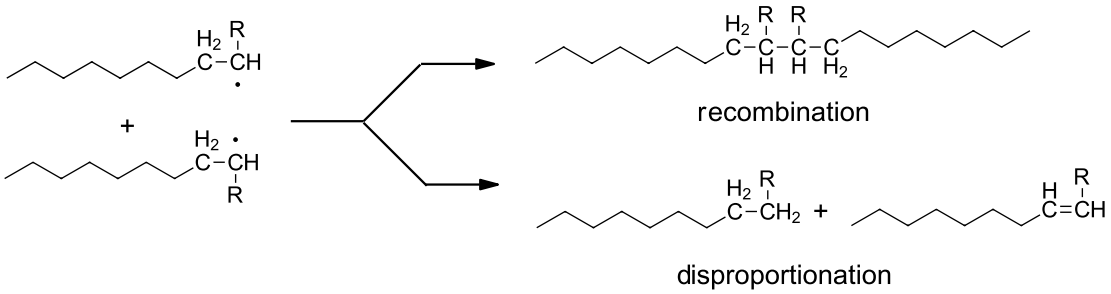

Scheme 4: Chain termination.

The type of termination mechanism depends on the used monomer and polymerization temperature. Lower temperatures lead to recombination and lastly polymers with higher molecular weight. The higher polymerization temperatures, lead on the other side to disproportionation mechanism and unchanged polymer molecular weight.

Chain transfer reactions play a vital role as well. The transfer reactions on monomers or initiators do not have as much influence as the transfer reactions on solvent molecules and polymer chains. The chain transfer reactions between polymer chains cause the branching of the polymers. If the chain transfer reaction happens intermolecular between two molecules, a long chain branching occurs. If on the other

side, an intramolecular transfer occurs short chain branched polymers are formed. (Scheme 5)

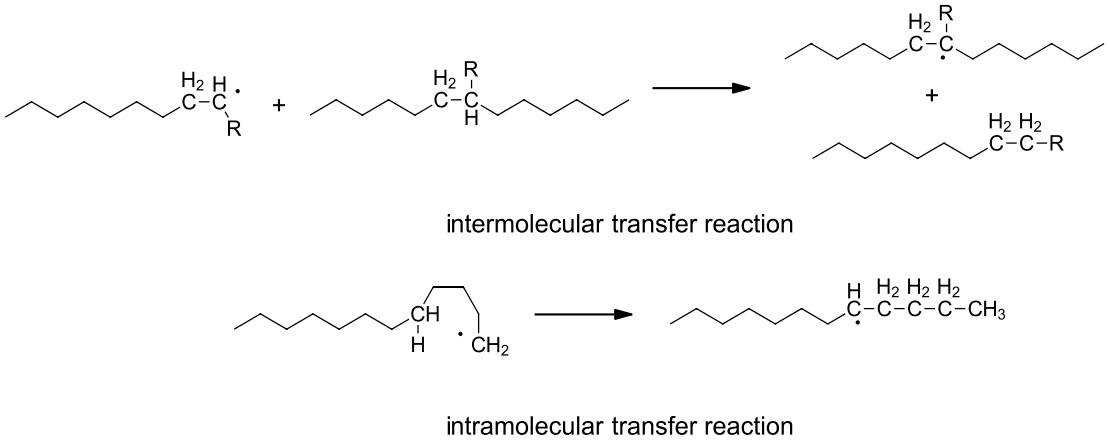

Scheme 5: Chain transfer reactions

Responsible for the absorption of light in a photoinitiator are the so-called chromophore groups consisting mainly of conjugated double or triple bonds and moieties like the carbonyl group.[7,10] For a photoinitiator to absorb the light, the emitted line of the light source must overlap with the absorption band of the photoinitiator.[7,10]

Upon the light absorption, the photoinitiator (PI) is promoted from its ground state (S_0) into its excited singlet state (S_1). From this short lifetime state ($<10^{-8}$ s), the photoinitiator can either regain its ground state (S_0) by fluorescence or radiation-free deactivation, or it can convert to its triplet state via intersystem crossing.[7] The triplet state has a longer lifetime (10^{-6} s) and leads therefore to the formation of radical species.[7] Competing with the formation of active species are deactivation processes such as phosphorescence, radiation-free deactivation, and bimolecular quenching processes.[7] These processes are summarized in a Jablonski diagram, represented in Figure 1.

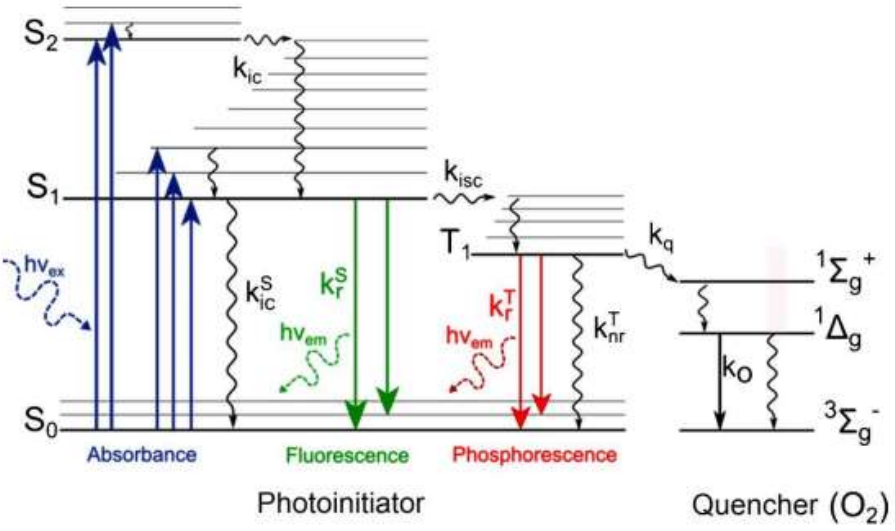

Figure 1: Jablonski diagram[11]

As mentioned, the chromophores of photoinitiators consist mainly of conjugated systems containing a carbonyl group.[7,9] The absorption properties of molecule can be controlled and influenced by structural modifications of the π-conjugated system.[12] The change of the absorption capabilities of a molecule without changing its parent structure, can be achieved through donor or acceptor substituents, or extending of the π-conjugation.[12] Therefore, through different substituents attached to the carbonyl group, the absorption of the photoinitiator can be influenced to either shift the maximum absorption to longer (bathochromic red-shift) or shorter wavelengths (hypsochromic blue-shift).[9,12] This ability to vary the absorption maxima through conjugation and introduction of functional groups enables the synthesis of photoinitiators with specific photo response and therefore the synthesis of photoinitiators for specific use.[9] Many commercially available photoinitiators consist of chromophores with n→π* and π→π* transitions.[9]

Based on the mechanism of radical formation there are two types of photoinitiators. The first type of photoinitiators undergo unimolecular reactions (Norrish Type 1) where the initiating radicals are formed directly through the fragmentation, and the second undergoes bimolecular reactions (Norrish Type 2) where the cleavage of the photoinitiator does not occur, but either H-abstraction or electron transfer via so-called co-initiator.

As mentioned, Type I photoinitiators when irradiated undergo fragmentation leading to the formation of initiating radicals. For fragmentation to occur, the dissociation energy

of the photoinitiator bond must be lower than that of the excited state.[7,9] However, the dissociation energy should be high enough for the photoinitiator not to cleave at the used temperature. Therefore, a certain equilibrium between photoreactivity and thermal stability must be reached.[9]

The Type I photoinitiators consist normally of aromatic carbonyl moiety that acts as the chromophore and suitable substituents that can facilitate the fragmentation. Based on the position and type of the substituent the cleavage of the molecule can either occur on α or β-position of the molecule.[7,9,10]

In the case of α-cleavage, the bond directly adjacent to a carbonyl moiety is cleaved. These photoinitiators tend to be more reactive due to the formation of two radicals: a highly reactive benzoyl radical and a radical whose structure depends on the substituents in the α-position.[7,9] This represents an advantage as both radicals can initiate polymerization processes. The important group of Type I photoinitiators that undergo α-cleavage are benzoin ether derivatives, alkyl aryl ketones, hydroxyalkylphenones, α-aminoketones, and acylphosphine oxide.[8,13] The cleavage of the C-C bond between the carbonyl group and alkyl residue requires sufficient initiation energy, typically provided through UV irradiation. Nevertheless, through the introduction of functionalities containing weaker bonds, the α-cleavage can be achieved with longer wavelength irradiation.[9]

The rate of α-cleavage is mainly determined by the configuration of the excited state ($n\pi^*$ or $\pi\pi^*$) and the type of substituent in α-position. The reactivity of the triplet state $n\pi^*$ exhibits higher reactivity towards α-cleavage than $\pi\pi^*$ state. Consequently, structural changes in the molecule that lead to a configuration shift from $n\pi^*$ to $\pi\pi^*$ can result in a loss of reactivity. Substituents in the α-position play a crucial role in influencing the rate of α-cleavage. Molecules with higher substitution generally undergo fragmentation more rapidly, as do molecules with substituents capable of stabilizing the positive charge on the α-carbon. Therefore, to enhance the rate of cleavage, many Type I photoinitiators possess hetero substituents such as hydroxyl, ether, amine, or possible aryl moieties.[9]

Due to this characteristic, Type I photoinitiators containing heteroatoms typically undergo cleavage upon exposure to longer wavelength light compared to aryl ketones. Consequently, photoinitiator classes such as acylphosphine oxide, acylsilane, and acylgermane are particularly valuable for photopolymerizations using visible light. [14–16]

Represented in Figure 2 is a Type I photoinitiator used in dentistry, the germanium-based Ivocerin®. [14–16]

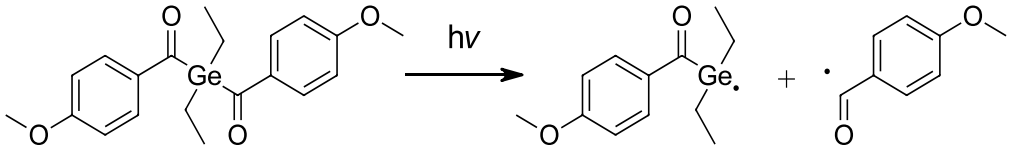

Figure 2: α-cleavage of the Type I photoinitiator Ivocerin®.

In addition to Type I photoinitiators that undergo α-cleavage, there are Type I photoinitiators that can undergo a β-cleavage.[10] β-Scission can occur in molecule when there is a weak bond present between the carbonyl-α-carbon and a heteroatom, and in β-position to a conjugated system.[10] A typical example of these photoinitiators is α-haloketone (Figure 3). Upon irradiation, highly reactive chlorine radicals are generated. These radicals can initiate polymerization or abstract a hydrogen from other compounds within the formulation. [7]

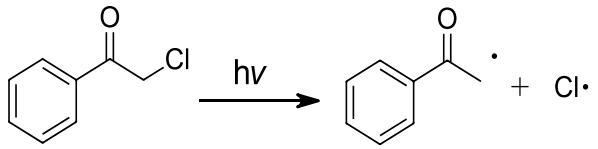

Figure 3: α-Chloro acetophenone, Type I photoinitiator that undergoes β-cleavage.

The Type II photoinitiators undergo a different mechanistic pathway from Type I photoinitiators. These molecules cannot undergo fragmentation in their excited state and therefore the initiating radicals are created through a bimolecular reaction with a so-called co-initiator.[7,9] Typical Type II photoinitiators are a large number of aromatic ketones such as benzophenone, substituted benzophenone, camphorquinone, xanthone, and thioxanthone.[13] These molecules can primarily follow two mechanistic pathways: either they undergo hydrogen abstraction by the excited initiator (such as benzophenone, as depicted in Figure 4), or they engage in photoinduced electron transfer leading to fragmentation (Figure 5).[7,9] In the latter case, the photoexcited compound acts either as an electron donor and the co-initiator as an electron acceptor or vice versa.[7]

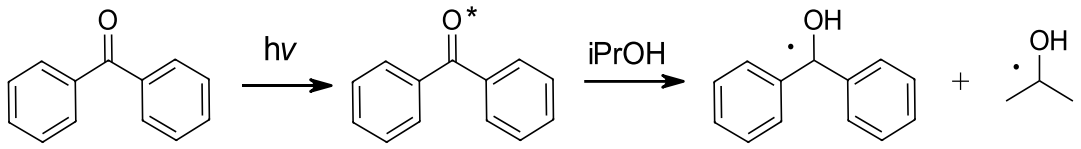

Figure 4: Photoinduced H-abstraction in benzophenone/isopropanol (iPrOH) Type II system

In this bimolecular reaction, the metastable excited triplet-state of benzophenone can react with a suitable donor compound, such as alcohol or phenol, leading to hydrogen atom abstraction. [7,17] As represented in Figure 4 isopropanol can act as such donor.[17] As the product of reaction two radicals are formed: a ketyl radical with a lower reactivity and a highly reactive donor radical.

The second type of bimolecular reaction is illustrated on an example of a CQ/DMAB system. In this system, the CQ contains a chromophore and, upon irradiation, transitions from its ground state to its excited singlet state. Subsequently, an electron transfer occurs to the suitable co-initiator, DMAB. This electron transfer is followed by the proton transfer, resulting in the formation of two radicals: a highly reactive amine radical capable of initiating the polymerization, and a less reactive CQ-radical that typically undergoes either dimerization or hydrogen abstraction.

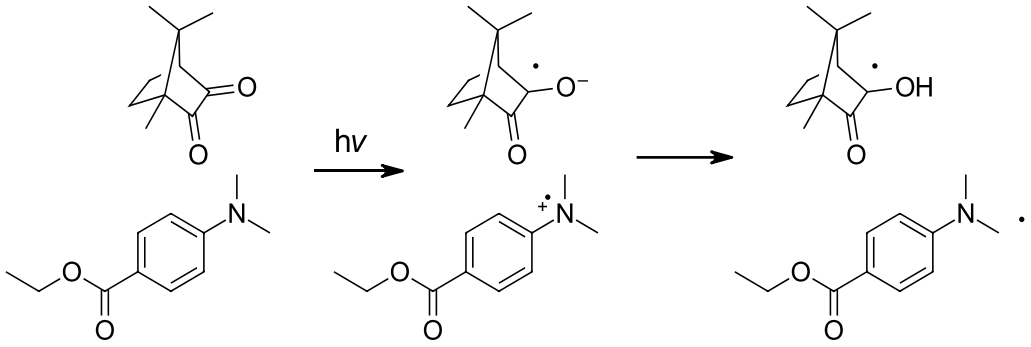

Figure 5: Photoinduced electron transfer followed by proton transfer and radical formation in CQ/DMAB Type II system.

When comparing the reactivity of Type I and II photoinitiators, Type I photoinitiators show a higher efficiency since no bimolecular processes are involved.[9,10] Furthermore, since the Type II photoinitiators have a much longer triplet lifetime, which is required for a bimolecular process to occur, they are much more prone to inhibition and quenching reactions.[9] Additionally, the bimolecular reactions are much more affected by the properties of the surrounding medium such as viscosity than Type I photoinitiators.[9]

The CQ/DMAB system (Figure 5), is a state-of-the-art photo-initiating system in dental applications.[14–16] This Type II photoinitiator shows absorption in the visible range of the UV-Vis spectrum with an absorption maximum of 468 nm which is compatible with the maximum emission wavelength of the LED dental lamps.[14,16] This is suitable for the curing of thick composite layers.[16] However, like other Type II photoinitiators, they show a lower reactivity due to their bimolecular nature and are strongly affected by the surrounding environment, making them problematic for applications in aqueous media.[14,16] Their major disadvantage is, however, the yellow color of the restoratives originating from CQ and the interaction of tertiary amines with acidic monomers.[19,20] Additionally, the large amounts of tertiary amines can impact the color of the restorative, as they have the potential to cause a long-term darkening.[19] Therefore, to overcome not only the disadvantages of the CQ/DMAB system but general disadvantages of the Type II photoinitiators, the more efficient Type I photoinitiators alternatives were developed.[14,16]

For this purpose, Ivocerin, represented in Figure 2, was developed. Ivocerin undergoes α-cleavage, generating a benzoyl radical and a highly efficient germanium radical. This photoinitiator shows an absorption range from 390 to 445 nm with maximum absorption at 418 nm. [19] Additionally, in contrast to CQ-systems, Ivocerin does not require the presence of an amine in the formulation, which leads to color-stable formulations and no interactions with acidic monomers.[21] However, Ivocerin faces some drawbacks, such as very poor water solubility and high cost due to the presence of germanium compounds.

Therefore, when it comes to choosing the appropriate photoinitiator for dental fillings various factors must be considered. Besides high reactivity, good compatibility, and solubility within the formulation, factors such as low toxicity, photobleaching, and yellowing must be considered as well.[9]

The important criteria that must be fulfilled by the dental filling is their color. To achieve white coatings, it is important to have a non-yellowing formulation and long-term color stability of the cured coatings. The yellowing of the cured materials can be caused either by photoproducts or more importantly by residues of the used photoinitiator.[9] Given that the substantial portion of the photoinitiator may remain unreacted in the cured material, this can lead to secondary reactions contributing to undesirable yellowing of the cured material.[7]

Another important aspect that must be considered when choosing the appropriate photoinitiator is photobleaching. Namely, as the initiating reaction progresses, the photoinitiator is consumed, potentially changing the absorption spectrum of the formulation resulting in photobleaching.[7] If the photoinitiator contains a visible light chromophore and undergoes fragmentation, the fragments usually have less extended chromophores and cannot therefore absorb long-wavelength light anymore, which is particularly desired in dental applications.[18]

Moreover, the ability of photoinitiator to absorb light at longer wavelengths is as well an essential requirement. This capability is crucial for enabling the curing of thicker layers, as it allows irradiation to penetrate more deeply into the material.[7] The photobleaching plays an important role here as well, since the photoinitiator in the layers nearest to irradiation source is consumed, light can penetrate easily through the sample.[22,23]

Acylphosphine oxides are the Type I photoinitiators that were introduced as a class of highly efficient photoinitiators suitable for curing thick films and white-pigmented formulations that show long wavelength absorption.[7,9] These Type I photoinitiators show attractive advantages like photobleaching and they can undergo a very efficient α-cleavage into benzoyl and phosphonyl radicals through a triplet excited state.[24,25]

Regarding the stability of these molecules, they exhibit thermal stability up to 180°C, preventing premature thermal polymerization of the formulation.[7,9] The primary challenge of acylphosphine oxide lies in their susceptibility to nucleophilic attack from water, amines, or alcohols, resulting in the solvolytic cleavage of the carbon-phosphorus bond.[7,9] This presents a significant issue, given that oligomers and additives used in UV formulations often possess nucleophilic properties.[7,9] Nonetheless, this drawback has been successfully resolved through the incorporation of sterically demanding substituents in the *ortho* position of benzoyl side of the molecule, which serve to shield the carbonyl group, preventing it from undergoing nucleophilic attack.[7,9,20] For this reason, all mono and bisacylphosphine oxides of practical significance have ortho-disubstituted benzoyl moieties.[9]

What distinguishes the acylphosphine oxides from (most) other Type I photoinitiators is their enhanced absorption in the near UV-Vis region. These molecules show an absorption maximum typically ranging from 350-380 nm with tailing to about 420 nm.[7,9] This long wavelength absorption is attributed to an nπ* transition, which is red-shifted

due to conjugation between the phosphonyl group and carbonyl group. The overlap of the free d-orbital of phosphorus with the π*-orbital of the carbonyl carbon atom leads to a reduction in orbital energy, consequently causing a bathochromic redshift of the absorption maxima.[9] Therefore, by varying substituents, it is possible to influence the nπ* absorption band.[9] The long wavelength absorption of acylphosphine oxide is bleached during irradiation, as the carbon-phosphorus bond is broken in the process, eliminating the previously described interaction in the photoproduct.[9] Consequently, the decreasing optical density enables a much deeper penetration of the irradiation light, facilitating the curing of thicker layers.[7,9] The combination of long-wavelength absorption, photobleaching effect, very little yellowing of the cured materials, and the ability to cure thicker layers makes these photoinitiators suitable for a variety of applications including dentistry.

Two important groups of acylphosphine oxide are the so-called monoacylphosphine oxide (**MAPO**) and bisacylphosphine oxide (**BAPO**). In Figure 6 represented are typical, commercially available representatives of **MAPO** and **BAPO** molecules.

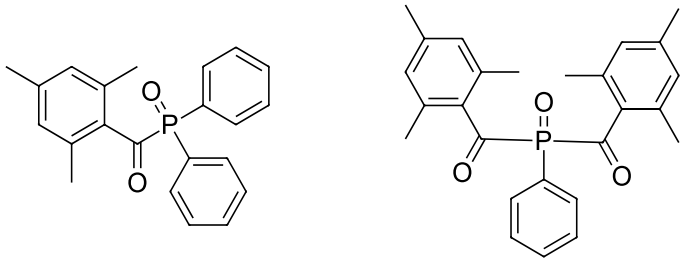

MAPO BAPO

*Figure 6: 2,4,6-trimethylbenzoyldiphenylphosphine oxide (**TPO**, **MAPO**) and bis-(2,4,6-trimethylbenzoyl) phenyl phosphine oxide (Irgacure 819®, **BAPO**)*

BAPO-derivatives such as Irgacure 819® represented in Figure 6 show compared to **MAPO**-derivatives a higher reactivity. The reason for this is the formation of four instead of only two radicals during the photolysis. As represented in Figure 7, the **BAPO** molecules undergo two-step fragmentation.

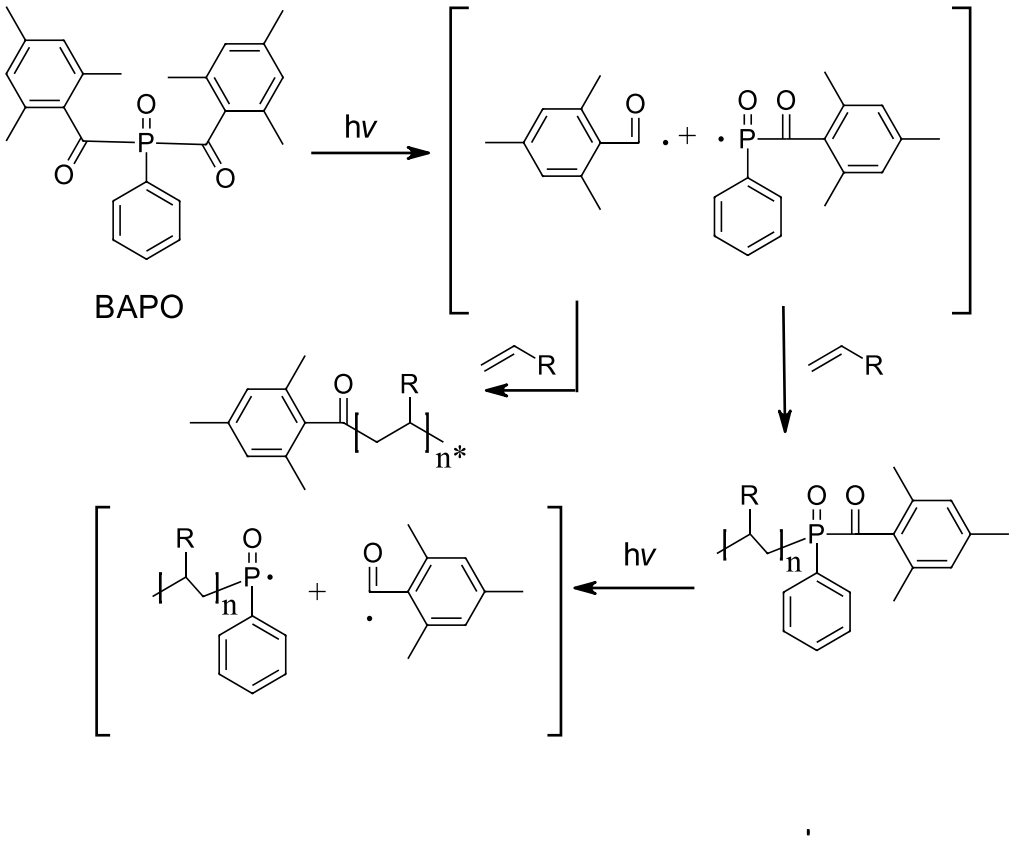

*Figure 7: Initiation mechanism for bis-(2,4,6-trimethylbenzoyl) phenyl phosphine oxide (Irgacure 819®, **BAPO**)*

Furthermore, compared to **MAPO** they show a bathochromic shift with an absorption range of 365-416 nm and an absorption maximum of 400 nm.[19] However, their absorption band does not overlap very well with the emission band of the currently used dental lamps.[16] The major disadvantage of the **BAPO** derivatives is however their poor solubility in a variety of monomers and oligomers.[19] Additionally, **BAPO** photoinitiators show higher cytotoxicity than CQ and **TPO** at the same concentration.[26]

A commercially available and widely used **MAPO** derivative is 2,4,6-trimethylbenzoyldiphenylphosphine oxide (**TPO**). (Figure 6) **TPO** is a Type I photoinitiator which when irradiated with UV-light, undergoes α-cleavage to form 2,4,6-trimethylbenzoyl radical and diphenylphosphinoyl radical (Figure 8).

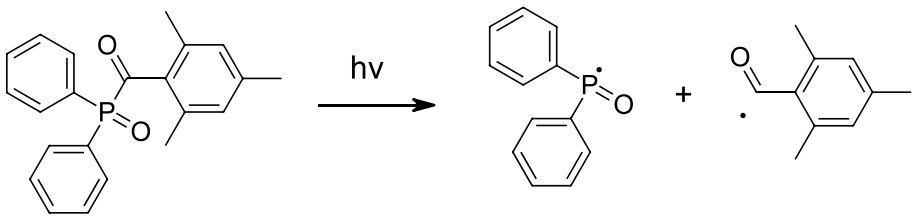

*Figure 8: α-cleavage of 2,4,6-trimethylbenzoyldiphenylphosphine oxide (**TPO**)*

The **MAPO** photoinitiators exhibit compatibility with a broad spectrum of monomers, including acrylates, methacrylates, acrylonitrile, vinyl ethers, or styrene.[9] As mentioned, in the photoinitiation process, both benzoyl and phosphonyl radicals are formed. Studies have shown that the phosphonyl radical displays significantly higher efficiency (two to three times) in adding to double bonds of monomer, compared to benzoyl radicals.[7,9] This enhanced reactivity is attributed to the tetrahedral structure of the phosphorus radical, which, upon meeting the olefinic group, encounters fewer hindrances by steric constraints.[7,9]

TPO is a commercially available **MAPO** photoinitiator that comes with several advantages, including the ability to polymerize in thick layers. Compared to CQ systems, **TPO** shows a higher degree of conversion and greater efficiency.[19] Furthermore, **TPO**-based materials demonstrate excellent color stability, which makes them well-suited for use in dental restoratives.[19] Because of these advantages, they are also widely used in UV-LED curable coatings, inks, and biomedical materials.[27]

Because their absorption range is shorter than that of CQ-systems (absorption maximum at 468 nm)[14], using formulations containing **TPO** would require new dental lamps, as standard dental lamps typically emit light between 420-490 nm.[19] Furthermore, in comparison to mixtures containing CQ, they exhibit a lower depth of cure and may lead to higher polymerization stress.[19] Additionally, **TPO** possesses a high migration ratio, making it unsuitable for some industrial applications such as environmentally friendly coatings and food packaging ink.[27] In these applications, the high migration ratio of **TPO** after curing is problematic, because it presents harm to human health, especially since **TPO** shows cytotoxic and genotoxic effects.[26,28]

A commercially available **MAPO** photoinitiator that overcomes this disadvantage of **TPO** is ethyl (2,4,6-trimethylbenzoyl) phenylphosphinate **TPO-L**. (Figure 9)

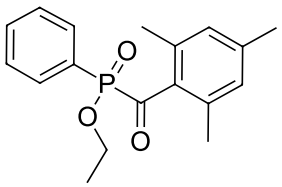

*Figure 9: Structure of ethyl(2,4,6-trimethylbenzoyl)phenylphosphinate **TPO-L***

TPO-L is a liquid Type I photoinitiator and like **TPO** shows an absorption wavelength band at 350-430 nm.[26] Compared to **BAPO** and **TPO**, **TPO-L** shows a much higher

biocompatibility. The lower cytotoxicity is a major advantage since the widespread use of photoinitiators has raised awareness of their possible toxic effects on humans, which makes **TPO-L** more promising for application in clinical practice including dental 3D-printed resins.[26,29] Furthermore, it shows excellent color stability, good volatility[29], transparency, and relatively high reactivity.[26] However, compared to **TPO**, **TPO-L** shows somewhat lower efficiency.[30] Because of these properties, **TPO-L** is currently being used in white-pigmented UV lacquers and UV overprint varnishes.[29]

However, to improve the disadvantages like lower reactivity, further developments of **MAPO** photoinitiators are still being researched.

OBJECTIVE

The objective of this work is the development of novel Type I monoacylphosphine oxide (**MAPO)**-based photoinitiators suitable for application in dentistry.

MAPO molecules, including **TPO** (2,4,6-trimethylbenzoyldiphenylphosphine oxide) and **TPO-L** (ethyl (2,4,6-trimethylbenzoyl) phenylphosphinate), meet the essential requirements for a photoinitiator suitable for use in dental restorations. These photoinitiators show excellent color stability, photobleaching effect, and high reactivity. Despite these advantages, the primary challenge associated with **MAPO** molecules is their absorption range, which has to be optimized for the currently used LED dental lamps. Furthermore, the biocompatibility of **TPO** represents a challenge when it comes to clinical applications.

Therefore, this work focuses on the development of novel **MAPO** photoinitiators with a bathochromic shift when compared to existing state-of-the-art **MAPO** molecules. Given the ability of heteroatoms on phosphorus to impact the efficiency of photolysis and absorption range, our focus is on exploring the effects of various substituents with different electronic influences. In this work, we focus primarily on synthesis of derivatives containing new phosphorus-heteroatom bonds, where the heteroatoms show either higher or comparable electronegativity to carbon, that is present in **TPO** molecules. For this reason, synthesis with substituents like amines, thiols, selenols, phosphines, sterically hindered alcohols, isocyanates and pseudohalides should be investigated. The goal is thereby to understand how these substituents influence the absorption and overall performance of the newly synthesized photoinitiators when compared to the established **MAPO** photoinitiators **TPO** and **TPO-L**.

The aim of this study is furthermore to investigate the photoinitiation of the newly synthesized **MAPO** derivatives in comparison to the established **MAPO**s **TPO** and **TPO-L**. To investigate the absorption capabilities of the new photoinitiators UV-Vis spectroscopy should be measured. The initiation efficiency of the new **MAPO** derivatives should be evaluated by photo-DSC measurements in UDMA formulation and compared to commercially available photoinitiators **TPO** and **TPO-L**. To furthermore understand and assess the efficiency of the photoinitiators, steady state photolysis should be performed, and quantum yields determined.

STATE OF THE ART

Over the past decade, the use of visible light for cross-linking processes has increased due to its ability to perform efficient curing with low energy consumption. Therefore, the research of novel photoinitiators that show high efficiency at these wavelengths has become a very important area of research.

During the last decade, the research has shifted from the use of bimolecular initiating systems such as CQ/DMAB to one-component systems. Due to their numerous benefits such as excellent UV and near-UV absorption, high reactivity, and photobleaching effect, acyl phosphine oxides have come forth as highly promising photoinitiators in modern photopolymerization techniques. Introduced in the 1980s, these photoinitiators have found a wide range of applications, particularly in industrial coatings and biomedical applications.[31] They are particularly effective in the curing of thick, pigmented, and white coatings which makes them highly interesting for application in dental restoratives. [31,32]

1 Synthesis of **MAPO**-derivatives

One of the reactions commonly used for the synthesis of acylphosphine oxide is the Arbuzov type reaction represented in Figure 10.[33]

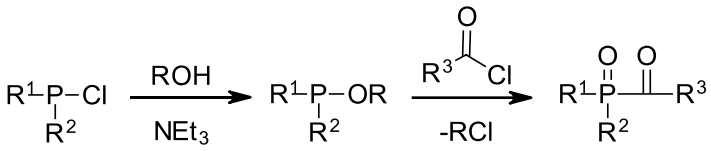

Figure 10: Arbuzov-type reaction for the synthesis of acyl phosphine oxide[33]

The desired acyl phosphine oxide is synthesized from corresponding alkoxy phosphines and acyl chloride. The synthesis of the precursor-alkoxyphosphine is performed through a coupling of chlorophosphine and corresponding alcohol. However, there are some major disadvantages of this reaction. Firstly, the needed chlorophosphine for the synthesis of alkoxyphosphine is not a widely available compound. Furthermore, the synthesized alkoxyphosphine shows a very high sensibility to air and moisture making their synthesis additionally complicated. Lastly, during the synthesis, chloroalkane is built as a by-product which represents an environmental issue when the large-scale synthesis is being considered.[33]

These disadvantages were addressed in further research and new synthesis methods were developed. Therefore, the synthesis of acyl phosphine oxide using α-hydroxy phosphine oxide was developed. [33]

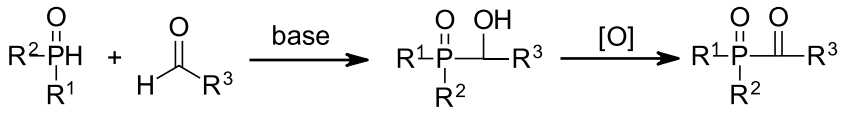

Figure 11: Synthesis of MAPO-derivatives by oxidation of α-hydroxy phosphine oxide[33]

In the first step of the reaction represented in Figure 11, α-hydroxy phosphine oxide is synthesized from secondary phosphine oxide and aldehyde in the presence of the base. Following this step, oxidation of the intermediate to obtain the desired product is performed. However, these reactions report a lower efficiency and high amounts of oxidants like MnO_2 needed to increase the yield of the desired product. [33]

Zhang et al.[33] report a successful synthesis that can overcome the drawbacks of the previously mentioned synthesis. They report a successful coupling of hydrogen phosphine oxide and acyl chloride (Figure 12). As the catalyst in the reaction chlorosilane is used.

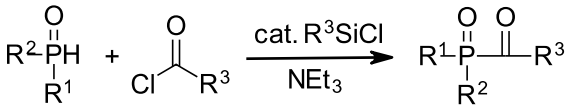

Figure 12: Synthesis of MAPO-derivatives reported by Zhang et al.

The new research focuses on modifying the already known **MAPO** photoinitiators to overcome their disadvantages. The synthesis of the new derivatives is based mainly on introducing structural modifications on the **TPO** molecule.[32]

Most conducted studies focus on the development of new **MAPO**-based photoinitiators by structurally modifying the benzoyl moiety in **TPO**. However, when a **MAPO** molecule, such as **TPO**, undergoes homolytic cleavage, a phosphonyl radical is formed that is two to three times more reactive than the benzoyl radical. [9] Therefore, understanding the impact of modifications on the phosphonyl moiety in **MAPO** molecules could yield interesting results.

However, very few studies have concentrated on the modification of the phosphonyl moiety and how this would influence the overall performance of the photoinitiator.[32] In Duan et al.[32] the structural modification of the phosphonyl moiety was performed. The used synthesis path is already mentioned and presented in Figure 12 where the addition

product of the aromatic aldehyde with corresponding diarylphosphine oxide was oxidized by MnO_2.[32] The synthesized photoinitiators are represented in Figure 13.

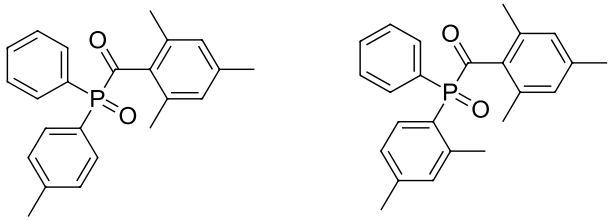

Figure 13: MAPO-derivatives synthesized in Duan et al. 2021

The results of this study showed firstly that the methyl groups on phosphonyl rest cause a similar positive effect against the nucleophilic cleavage as the methyl groups on the benzoyl moiety. Furthermore, they show lower migration and better absorption abilities compared to **TPO**. The introduction of the methyl group in para positions showed an improvement in molar extinction coefficient and the methyl group in ortho position was shown to be beneficial for long-wavelength absorption.[32]

Compared to the mentioned synthesis strategies for **MAPO** molecules, Roszkowski et al.[34] reports a synthesis method for new **MAPO** molecules with modified phosphonyl moieties using a simple and efficient synthesis strategy (Figure 14). Furthermore, compared to other methods it offers a synthesis that can be performed under mild reaction conditions and with commercially available starting materials. [34]

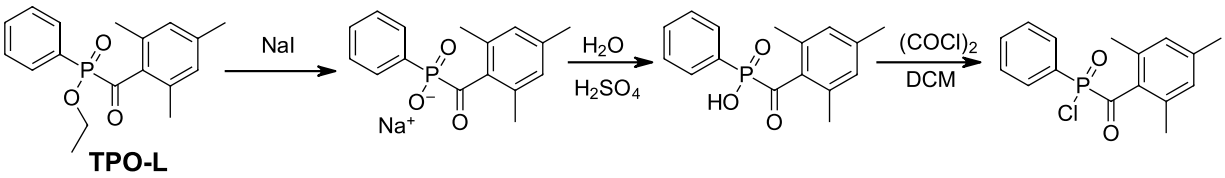

Figure 14: Synthesis route of new MAPO derivatives applied in Roszkowski et al.

The starting compound **TPO-L** was first reacted with sodium iodide and afterward hydrolyzed in the presence of an acid. The obtained free acid was then reacted with oxalyl chloride into corresponding phosphinic acid chloride.[34]

The development of new **MAPO** derivatives, which compared to **TPO** have a modified phosphonyl moiety is still to be researched. Especially when it comes to phosphonyl modifications where the new substitutes are directly attached to the phosphorus atom. While some studies have focused on the synthesis of **MAPO** derivatives with alkyl chains with varying lengths directly attached to phosphorus, there are almost no

studies into the influence of electronic properties of substituents, where a heteroatom is directly attached to phosphorus.

2 Improvement of the known **MAPO**s

Besides their numerous advantages, the **MAPO** photoinitiators have certain drawbacks that need to be addressed:

- Low solubility in water[31]
- Migration of unreacted species[35]

  As a significant portion of the photoinitiator remains unreacted in the formulation, these unconsumed species have the potential to migrate to the materials surface. This represents a major problem, especially in certain potential applications such as the food industry, or in applications within the human body, such as dentistry. [35]

- Low absorption of visible light[7,9,32,36]

  Responsible for the bathochromic shift of the **MAPO** molecules is the n→π* transition caused by the interaction between the empty d-orbital of the phosphorus atom with the π*-orbital of the carbon atom in the carbonyl group.[9] The **MAPO** photoinitiators typically show absorption maximum ranging from 350-380 nm with tailing to about 420 nm.[9] These wavelengths however do not overlap very well with the momentarily used dental lamps.

Several conducted studies, presented in the following, have managed to address the mentioned disadvantages of **MAPO** molecules.

As mentioned, one of the drawbacks of acyl phosphine oxide photoinitiators is their low solubility in water. This characteristic is however highly required for not only industry but also biomedical applications. To increase the water-solubility of **MAPO** molecules, ionic photoinitiators such as lithium phenyl-2,4,6-trimethylbenzoylphosphinate (Li-TPO, Figure 15) were developed. [31]

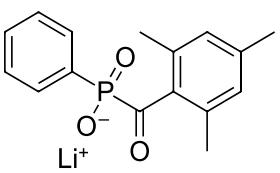

Figure 15: Structure of Li-TPO

Besides their enhanced water solubility, these photoinitiators showed very good efficiency and polymerization at longer wavelengths. Further research in enhancing the water solubility of acylphosphine oxide was performed by derivatization of the molecules with hydrophilic and electron-donating groups.[31] For example, the derivatization of **BAPO** molecules with oligo- and poly(ethylene glycol) (Figure 16) has resulted in water-compatible photoinitiators with red-shifted absorption wavelengths. [31]

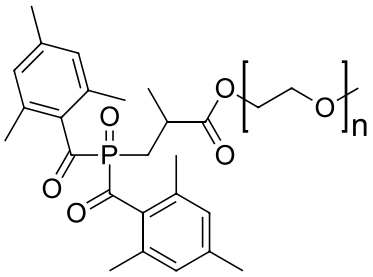

Figure 16: Structure of PEG-BAPO

The disadvantage of higher migration was addressed in Liu et al.[35] This research focused on developing new **MAPO** photoinitiators that would show reduced migration to the material surface compared to **TPO**. To achieve this, the researchers developed **MAPO** molecules containing various naphthyl groups instead of benzoyl moiety (Figure 17).

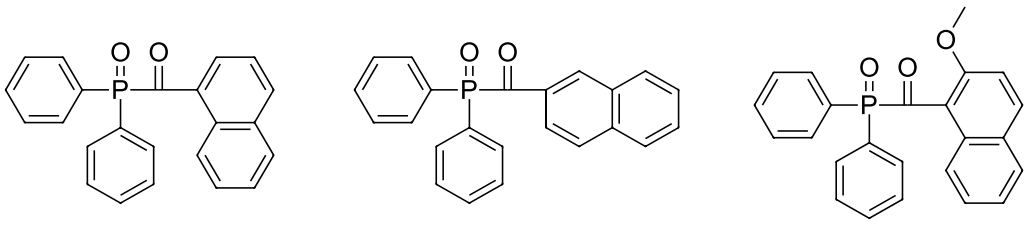

Figure 17: Structures of naphthyl-based acyl phosphine oxide photoinitiators[35]

The results of this study showed that the naphthyl-based photoinitiators possess higher molar absorption coefficients and better-initiating efficiency than **TPO**. Furthermore, the migration characteristics of these molecules compared to **TPO** were reduced as well. [35]

On the other side, the research described by Xie et al.[36] focuses on improving the absorption capabilities of **MAPO** molecules. To achieve a bathochromic shift, they propose introduction of an electron-donating substituent, diethyl amine, on the benzoyl moiety of **TPO** (Figure 18).

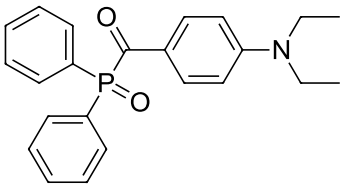

Figure 18: Structure of diethylamine MAPO derivative DEAPO[36]

The results of this research report a bathochromic shift of the new photoinitiator compared to **TPO**. The electron-donating substituent has caused a red shift of the absorption into the visible range (400-440 nm).[36] Additionally, the research reports a higher efficiency and lower migration compared to **TPO**.[36]

The synthesis of electron-donating substituents on acyl side of **TPO** molecule was performed as well in research performed by Nazir et al.[37] where the possible use of these photoinitiators for two photon induced polymerization was investigated. They have shown that through a suitable donor group a push pull system can be achieved which leads to an absorption increase up to 440 nm.[10] For this purpose, they have performed the synthesis of dimethyl and dihexyl amine derivatives of **TPO**. (Figure 19)

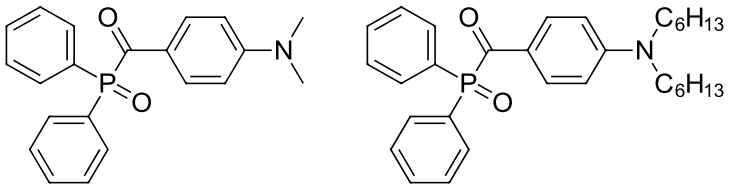

Figure 19: Structures of DMAPO (left) and DHAPO (right)[37]

Both photoinitiators showed absorption range varying from 325 nm to 435 nm.[38] When comparing the three modifications, the DMAPO with the shortest dimethylamine chain showed the lowest absorption maximum of 380 nm, followed by diethylamine modified DEAPO (Figure 18) with an absorption maximum of 386 nm and finally dihexylamine derivative DHAPO with 390 nm.[38]

GENERAL PART

NOVEL MONOACYLPHOSPHINE OXIDES

General synthesis strategy

For the synthesis of desired derivatives of monoacylphosphine oxide (**MAPO**s) two synthetic pathways were investigated: nucleophilic (Scheme 6) and electrophilic (Scheme 7).

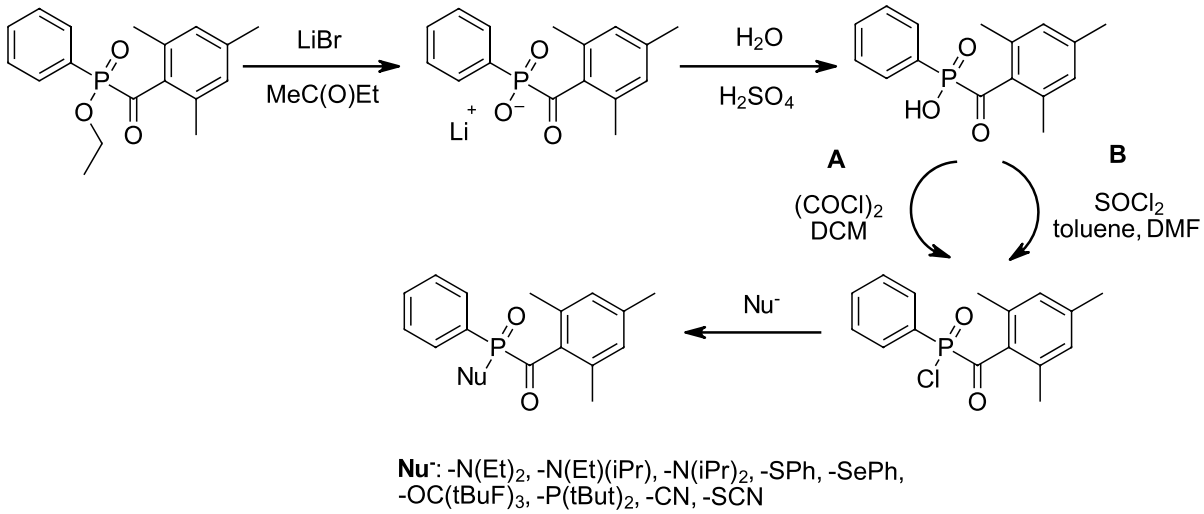

*Scheme 6: Potential synthesis pathway for new **MAPO** derivatives using nucleophilic approach.*

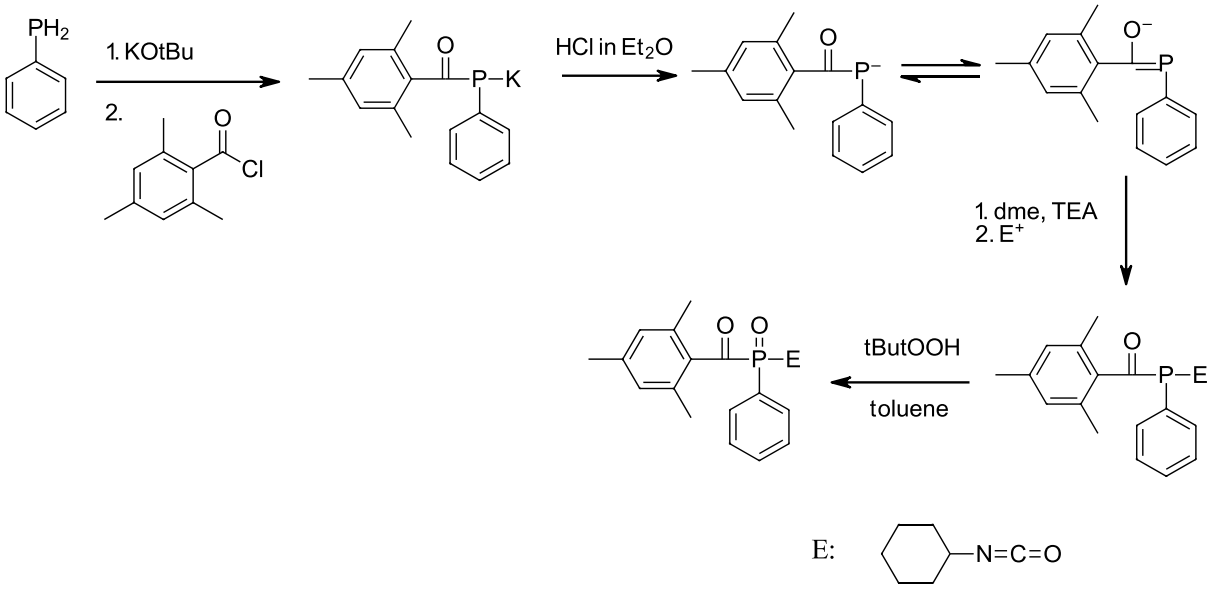

*Scheme 7: Potential synthesis pathway for new **MAPO** derivatives using electrophilic approach.*

1 Nucleophilic Reactions

One of the goals of this research was to find and investigate a simple and efficient synthesis approach for new **MAPO** photoinitiators. The main part of the research relies on a well-established synthetic pathway that offers a precursor that can undergo nucleophilic reactions and yield the desired new **MAPO** derivatives.

There are two known approaches for the synthesis of α-carbonylphosphine oxide.[37] The classical synthesis route is represented in Figure 12 (page 18) where the corresponding acid chloride is reacted with alkoxyphosphine oxide. However, even though this synthesis method is straightforward, it suffers from some drawbacks like the availability of the proper acyl chloride.[37] The second widely used synthesis approach (Figure 11, page 18) is a two-step reaction. In the first step, aldehyde is added to corresponding diphenyl phosphine in the presence of a catalyst. The synthesis of α-hydroxyphosphine oxide is then followed by oxidation with MnO_2 to yield the desired acylphosphine oxide. However, this method, as discussed, comes as well with some drawbacks like a lower efficiency and the higher amounts of MnO_2 needed for the reaction. [33,37]

For these reasons, for the synthesis of new **MAPO** photoinitiators we applied the synthesis method reported by Roszkowski et al. and represented in Figure 14 (page 19) that can be performed under mild reaction conditions and starting from commercially available products.

1.1 General procedure for precursor synthesis (**3**)

New **MAPO-based** photoinitiators which compared to **TPO** have a modified phosphonyl rest that desirably shows better absorption and reactivity a general procedure described in the following was used. The synthesis pathway starts with a commercially available derivative of **TPO**, **TPO-L**. The general procedure for the synthesis of precursor **3** is represented in Figure 20.

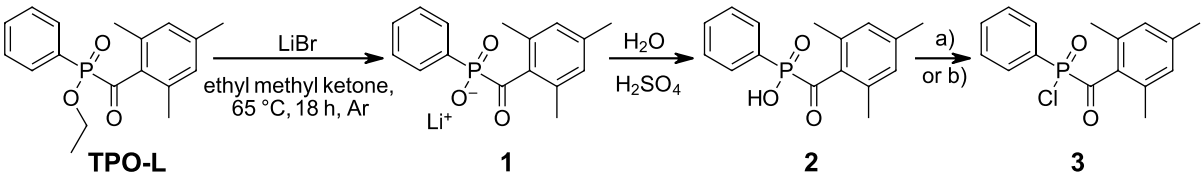

*Figure 20: General Procedure for the synthesis of precursor **3**. a) Oxalyl chloride, DCM, rt b) Thionyl chloride, toluene, DMF, 110°C*

Following the literature-known synthesis of **1**,[39] **TPO-L** was reacted with lithium bromide to synthesize the corresponding salt. The crude product was precipitated during the reaction. After washing the crude product, the final purification of **1** was performed by recrystallization from diethyl ether. Pure product **1** was obtained with a good yield (82 % of the theory).

The synthesis of acid **2**, was performed following the standard procedure described in the literature. [39,40] The lithium salt **1** was hydrolyzed under acidic conditions and the desired product **2** was precipitated during the reaction. After the final evaporation of the solvent product **2** was obtained as a pure pale-yellow solid with excellent yield (99 % of the theory).

The last step of the general procedure was the synthesis of acid chloride **3**. There are various literature-known approaches for the synthesis of **3**. In this work, two synthetic pathways were applied. In the first approach described by Roszkowski et al. [34] the phosphonic acid **2** was transformed into corresponding acid chloride **3** with oxalyl chloride. Therefore, the starting material **2** (1 eq.) was suspended in DCM and oxalyl chloride (2 eq.) was added dropwise. The reaction was performed at room temperature and under an argon atmosphere for 18 h. Finally, the acid excess was removed *in vacuo* and the product was obtained as a pale brown liquid (93 % of the theory).

The second synthesis approach was described in Oesterreicher et al.[39] where the phosphonic acid **2** was reacted with thionyl chloride. The starting material **2** (1 eq.) was suspended in toluene and thionyl chloride (20 eq.) was added dropwise. The temperature was raised to 110 °C and the reaction was completed in 3 h. After the removal of acid excess, the product was obtained as a dark brown liquid (71 % of the theory).

Since the first pathway to desired acid chloride, **3** had higher yields (93 % vs. 71 % of the theory) and was performed under milder reaction conditions such as room temperature and lower amount of acid, the synthesis of choice was the synthesis

reported by Roszkowski et al.[34] Both approaches, however, yielded impure crude products. Nevertheless, these crude products were directly used in the following synthesis step.

Following the described procedure for precursor synthesis, the novel **MAPO**-based photoinitiators were synthesized. The synthesis approach involved carrying out nucleophilic substitution on precursor acid chloride **3**, following the S_N2 mechanism, where chloride acted as the leaving group.

Initially, the reactions were conducted with electron-donating compounds, like amines. Nazir et al. showed that electron-donating amines on acyl side of the acylphosphine oxide (Figure 18 (page 21) and Figure 19 (page 22)) significantly influence the absorption capabilities of the photoinitiators, with the absorption of the π→π* transition shifted up to 440 nm.[10] Therefore, the introduction of amine substituents on phosphonyl side of the molecule and their influence on the absorption capability compared to **TPO** should be investigated.

The bathochromic shift that could possibly be achieved through this modification, could be explained by the fact that electron-donating substituents are able to stabilize d-orbital of phosphorus, that overlaps with the π*-orbital of the carbonyl group. This interaction should lead to an increase in energy of bonding π and decrease in energy of anti-bonding π* orbital (Figure 21). Since the energy of the non-bonding orbital n is unchanged through this interaction, the energy difference between n and π* orbital decreases. This means that the light with longer wavelength is needed for nπ* transition to occur.

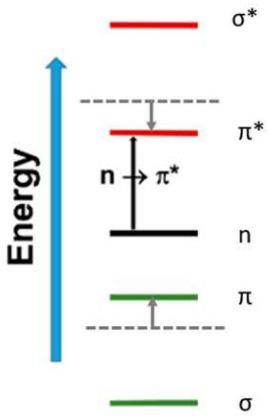

Figure 21: Bathochromic shift of the nπ transition due to the introduction of heteroatoms with higher electronegativity on phosphorus atom next to carbonyl group.*[41]

1.2 Nitrogen-substituted MAPOs

For the synthesis of new **MAPO**-based photoinitiators containing phosphorus-nitrogen bond nucleophilic substitution on **3** with amin was performed. In Figure 22 represented amines were used to investigate not only their electronic effects on performance and absorption compared to standard **MAPO** photoinitiators but also the influence of different steric demands exhibited by these molecules. The characterization of the synthesized photoinitiators was performed via UV-Vis spectroscopy and photo-DSC analysis.

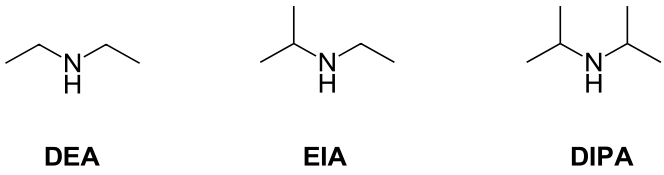

*Figure 22: Amine used in nucleophilic reactions with precursor **3**.*

1.2.1 Phosphinic acid amide **4**

*1.2.1.1 Synthesis of phosphinic acid amide **4***

Roszkowski et al. report a successful synthesis of trialkoxysilyl terminated photoinitiators from precursor **3** which could be immobilized on different surfaces such as the surface of nanoparticles. The reported synthesis was performed under an inert atmosphere and mild reaction conditions. Following this research[40] synthesis of **4** was performed.

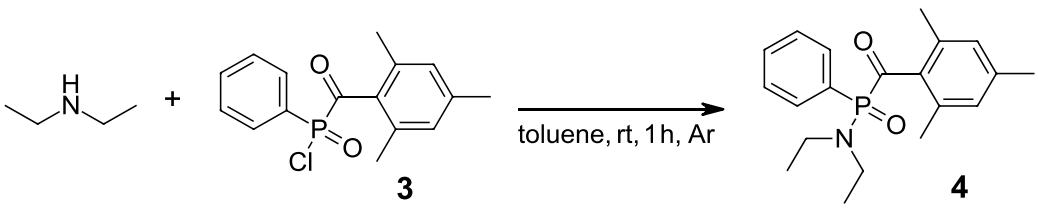

The synthesis was performed by nucleophilic substitution, where chloride was separated as the leaving group and the desired product was synthesized. The reaction was performed under an inert atmosphere, in toluene, and at room temperature. Reaction control was performed with ^{31}P-NMR and UPLC-MS. It was concluded that the desired product was formed within 1 h of the reaction.

The reaction was monitored by ^{1}H-NMR and UPLC-MS. Since **MAPO** molecules are known to be unstable in the presence of nucleophiles, besides the desired product **4**, two byproducts of nucleophilic cleavage were identified (see Figure 23) as well as the hydrolysis product **2**.

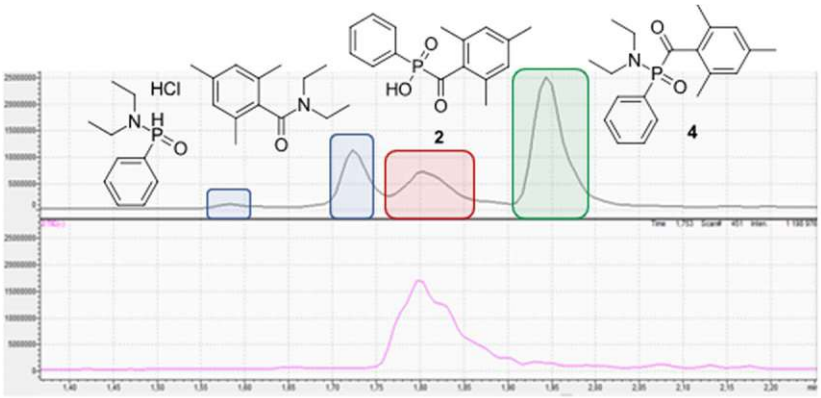

Figure 23: UPLC-MS measurement after 1 h of reaction time

The purification of the crude product was performed in two steps. In the first step, the excess of the base was removed to stop further cleavage of the product. For this purpose, the crude product was washed with diluted acid solution and then evaporated to dryness. During this purification step, the phosphorus byproduct, and the hydrolysis product **2** were removed from the crude product.

Finally, to remove the carbonyl byproduct, the second step of purification was recrystallization from petroleum ether. The pure product was separated as a pale-yellow solid with a good yield (65 % of the theory).

The characterization of absorption and performance of the new **MAPO** photoinitiator **4** as well as its parent photoinitiators **TPO** and **TPO-L** was carried out via UV-Vis spectroscopy and photo-DSC.

1.2.1.2 UV-Vis Spectroscopy

To investigate the absorption capabilities of the new photoinitiator **4** UV-Vis measurements were performed. As reference molecules, **TPO** and **TPO-L** were used. The samples were prepared as 1 mM solutions in acetonitrile. The results are presented in the following Figure 24.

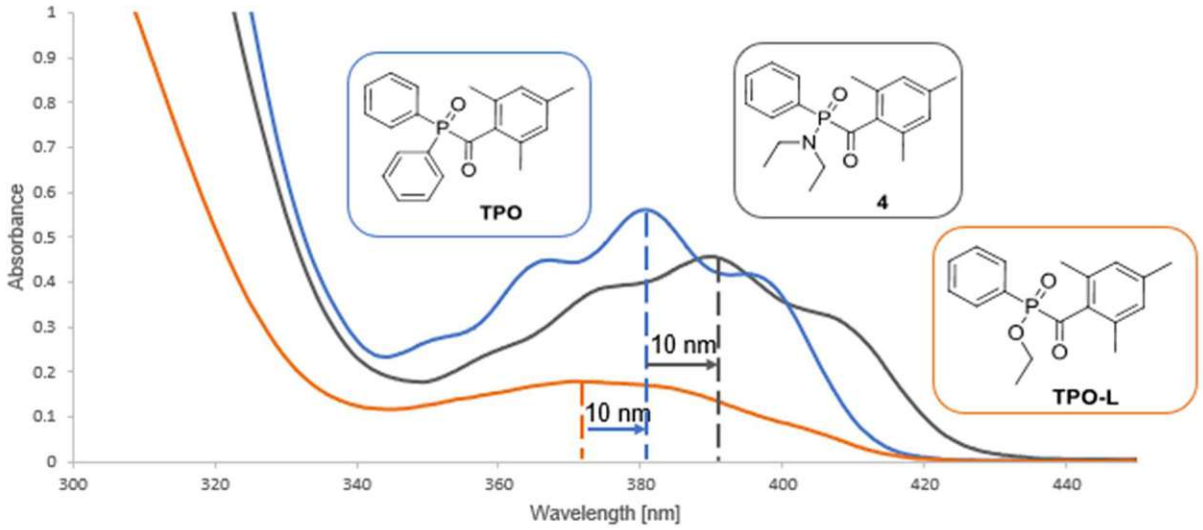

*Figure 24: UV-Vis spectra of 1 mM solutions of **TPO** (blue), **TPO-L** (orange) and **4** (grey) in acetonitrile.*

As in Figure 24 represented, the new photoinitiator **4** shows a maximum absorbance at 390 nm and therefore a bathochromic shift of 10 nm compared to **TPO**. This result was expected since the bathochromic shift in **MAPO** molecules is primarily attributed to the n→π* transition. This shift is red-shifted due to the interactions between the d-orbital of phosphorus and the π*-orbital of the carbonyl carbon atom. Electron-donating substituents, such as amines, can stabilize the d-orbital of phosphorus. Consequently, this stabilization affects its interaction with the π*-orbital of the carbon atom in the carbonyl group, resulting in the observed bathochromic shift of the n→π*-transition.

When comparing the bathochromic shifts of **TPO-L** and **4**, the stronger influence of the amine can be attributed to the stronger electron-donating effect of nitrogen in amine compared to oxygen in alkoxy groups. Consequently, this effect of amines enhances the stabilization of the d-orbital, thereby influencing its interaction with the π*-orbital of the carbon atom in the carbonyl group and contributing to the observed bathochromic shift in the n→π*-transition.

What is visible as well is that **4** shows a small decrease in the maximum absorbance which could be explained by the more flexible phosphorus substituent in **4** compared to the sterically demanding phenyl ring found in **TPO**. This reduced sensitivity to the light source influences the efficiency of the photoinitiator. Therefore, in the following, the performance of the photoinitiator **4** was characterized using photo-DSC measurements.

1.2.1.3 Photo-DSC measurements

Photo-differential scanning calorimetry (photo-DSC) is a very quick experiment that can determine the performance of the given formulation. To compare the results of the new photoinitiator **4** with industrially applied photoinitiators, **TPO** and **TPO-L** were used as references.

To quantify the measurements, after the evaluation of the collected data, several parameters were collected/determined to compare the performance of the measured photoinitiators. The performance was evaluated based on the heat of polymerization (derived from peak area), the time until heat flow maximum is reached (t_{max}), peak height (directly proportional to the rate of polymerization R_p), double bond conversion (DBC), and time to reach 95 % of the total heat flow ($t_{95\%}$). Photo-DSC studies were conducted using broad and narrow-band irradiation.

For the calculation of the double bond conversion (DBC), the following Equation 1 was used:

$$DBC\ [\%] = \frac{\Delta H_P * M_M * W_M}{\Delta H_0}$$

Equation 1: Calculation of DBC [%]

ΔH_P *polymerization heat [J/g]*
M_M *molecular weight of the monomer [g/mol].*
M_M(UDMA)=470.56 g/mol
W_M *weight percentage of the monomer [%]*
ΔH_0 *theoretical polymerization heat of the monomer [J/mol].*
ΔH_0(UDMA)=112000 J/mol

The rate of polymerization R_P is determined by Equation 2.

$$R_P[mmols^{-1}L^{-1}] = \frac{h * \rho}{\Delta H_0} * 1000$$

Equation 2: Calculation of R_p [$mmols^{-1}L^{-1}$]

h *height of the photo-DSC signal [mW/mg]*
ρ *density of the monomer [g/L]*
ρ(UDMA)=1100 g/L
ΔH_0 *theoretical polymerization heat of the monomer [J/mol].*
ΔH_0(UDMA)=112000 J/mol

Photo-DSC studies using broadband irradiation

The first performance study was conducted with broadband irradiation. The measurements were carried out in UDMA as monomer and the samples consisted of 1 mol% of corresponding photoinitiator. The samples were irradiated for 300 s with UV-light in the range of 320 nm to 500 nm. The irradiation was performed with an intensity of 60 $mWcm^{-2}$ and under nitrogen atmosphere (20 $mLmin^{-1}$).

In the following Figure 25 the measured heat flow of the polymerization for **TPO**, **TPO-L,** and **4** is represented.

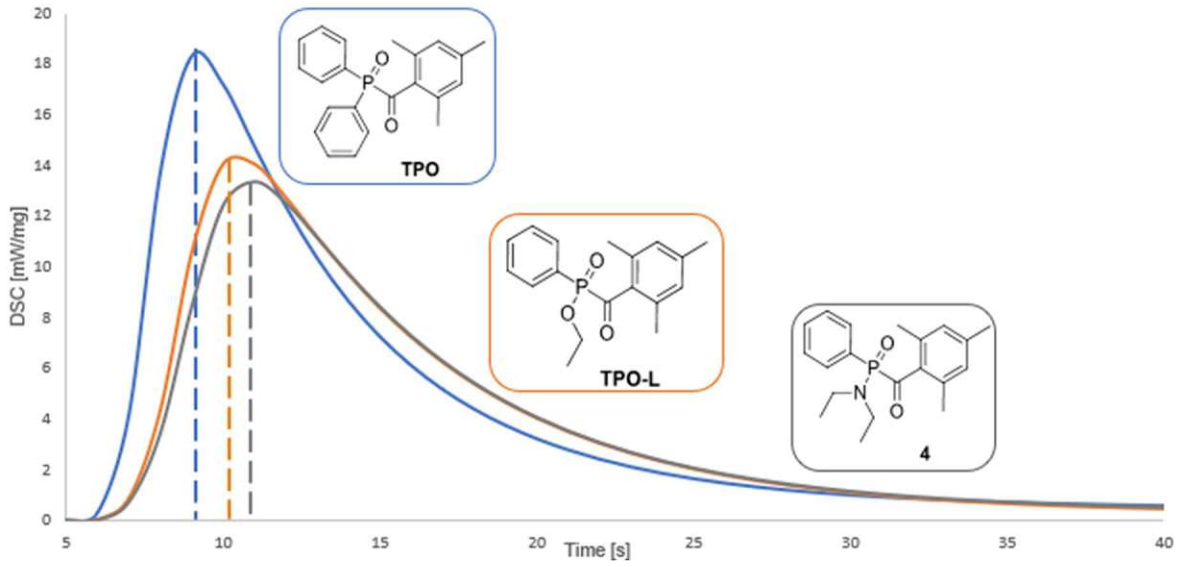

*Figure 25: Photo-DSC analysis of formulations consisting of 1 mol% **TPO** (blue), **TPO-L** (orange), and **4** (grey) in UDMA at room temperature using broadband irradiation.*

When comparing the results of the conducted measurements depicted in Figure 25, it is apparent that **TPO** exhibits greater polymerization heat compared to both **TPO-L** and **4**. Furthermore, it is as well visible that **TPO** needs 9 s to reach the peak maximum whereas **TPO-L** needs 10 s and **4** 11 s. Therefore, **TPO** shows a better performance than **TPO-L** or **4** under the measuring conditions.

To further characterize and understand the abilities of the new photoinitiator **4** and to compare these to **TPO** and **TPO-L**, double bond conversion (DBC) and rate of polymerization (R_p) were determined as well using Equation 1 and Equation 2.

The calculated DBC for the photoinitiators **TPO**, **TPO-L,** and **4** are represented in Figure 26.

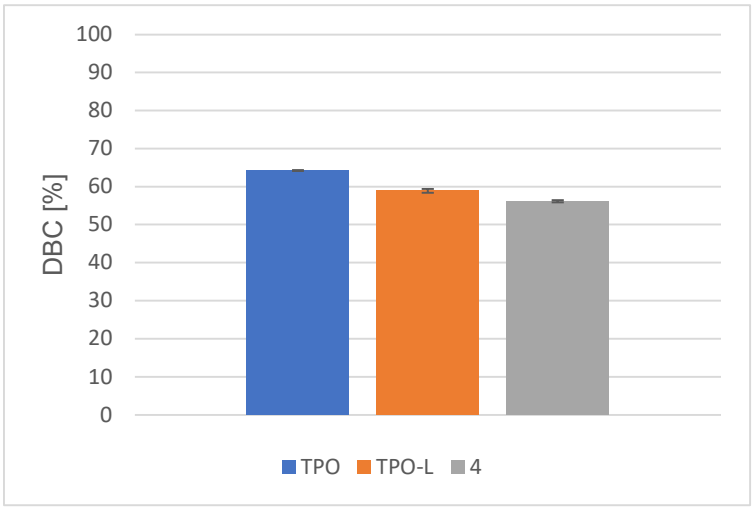

*Figure 26: Comparison of DBC values for **TPO, TPO-L,** and **4** obtained from broadband photo-DSC measurements.*

When comparing the efficiency in the conversion of the monomer to the desired polymer, **TPO** shows the highest performance, followed by **TPO-L** and finally photoinitiator **4**. The calculated rates of polymerization are represented in Figure 27.

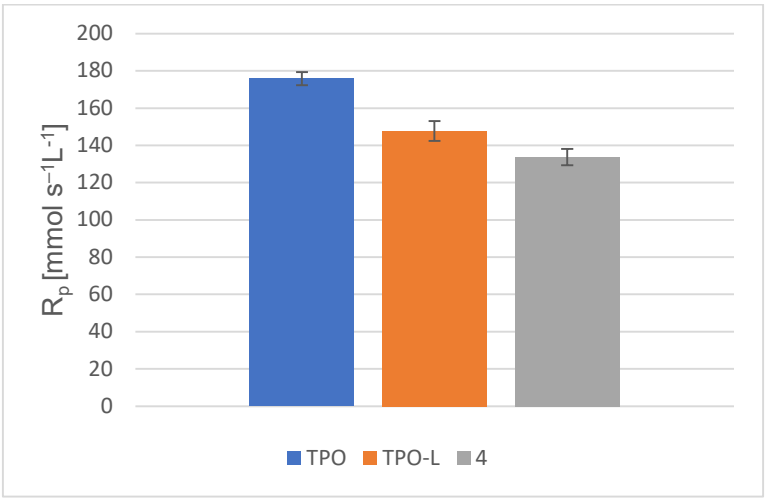

*Figure 27: Comparison of Rp values for **TPO, TPO-L,** and **4** obtained from broadband photo-DSC measurements.*

According to the represented data, it can be concluded that **TPO** has not only the highest efficiency in monomer conversion, but also the highest rate of polymerization. Sadly, the new photoinitiator **4** falls with its performance behind **TPO-L**.

The collected results of the measurements are represented once again in the following Table 1.

*Table 1: Photo-DSC analysis of formulations consisting of 1 mol% **TPO**, **TPO-L**and **4** in UDMA at room temperature using broadband irradiation.*

Sample	t_{max} [s]	Height [mW/mg]	$t_{95\%}$ [s]	Area [J/g]	DBC [%]	R_p [mmol $s^{-1}L^{-1}$]
TPO	9.26 ± 0.2	17.8 ± 0.4	39.0 ± 1.6	154 ± 0.2	64.2 ± 0.1	176 ± 4
TPO-L	10.1 ± 0.3	14.9 ± 0.5	37.4 ± 1.5	141 ± 1	58.9 ± 0.5	148 ± 5
4	10.9 ± 0.1	13.5 ± 0.6	36.1 ± 0.9	134 ± 0.6	56.2 ± 0.4	134 ± 4

From the represented date it can be finally concluded that **TPO** and **TPO-L** perform better than **4**. Nonetheless, some similarities in the performance of **TPO-L** and **4** can be observed. This can be attributed to the electronic effects of the two phosphorus substituents in these compounds. Both the ethoxy group (**TPO-L**) and the diethyl amino group (**4**) are electron-donating groups. Additionally, oxygen and nitrogen possess higher electronegativity than carbon, which is present in the phenyl ring of **TPO**. This connection between performance and the electronegativity of phosphorus substituents should be taken into consideration.

In addition to electronegativity, it is crucial to account for the steric factors of the substituents. Steric hindrance significantly influences reactivity, and both **TPO-L** and **4** have considerably less sterically demanding substituents compared to **TPO**.

Photo-DSC studies using LED irradiation

Further studies into the performance capability of the new photoinitiator **4** were conducted by photo-DSC using selective sources of irradiation. To simulate the narrow wavelength distribution in photo-DSC, commercial LED spotlight sources of 385 nm and 405 nm were used.

Photo-DSC study using 385 nm LED irradiation.

This photo-DSC study was performed with a 385 nm LED spotlight source. The formulations for the measurements consisted of UDMA with 1 mol% of the corresponding photoinitiator. Besides the photoinitiator **4**, **TPO** and **TPO-L** were once again used as references. The conditions of the measurements were kept according to the broadband measurements so that a comparison between these can be drawn. The measurements were therefore performed at room temperature, under a nitrogen atmosphere (20 $mLmin^{-1}$), for 300 s and with an intensity of 60 mW/cm^2.

The recorded polymerization heat plotted against the measurement time is represented in Figure 28.

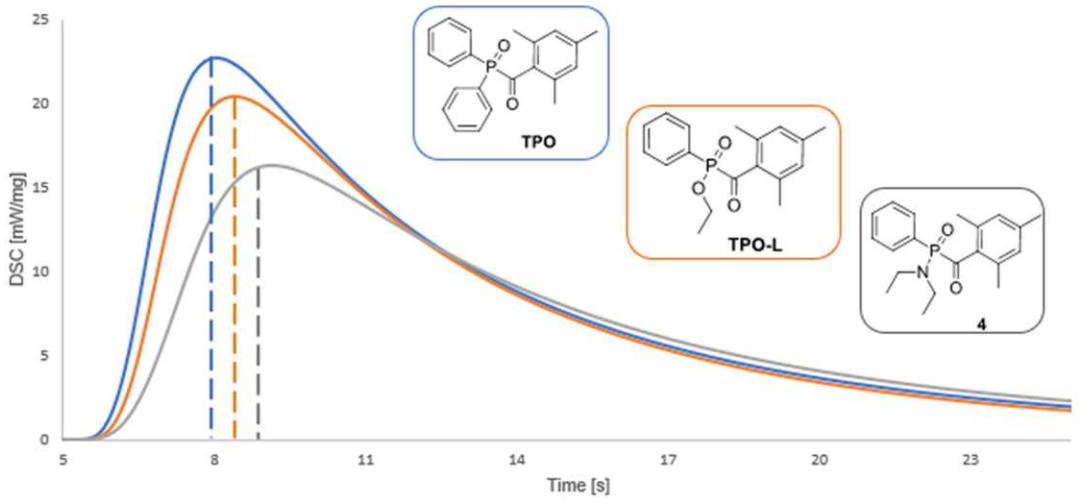

*Figure 28: Photo-DSC analysis of formulations consisting of 1 mol% **TPO** (blue), **TPO-L** (orange), and **4** (grey) in UDMA at room temperature using 385 nm LED irradiation.*

The measurements at 385 nm show compared to the ones conducted with broadband irradiation a higher reactivity of all three photoinitiators. According to the represented data, when comparing the time needed to reach the maximal heat flow, **TPO** shows once again the highest reactivity, and **4** the lowest.

Further data collected from these measurements are represented in Table 2.

*Table 2: Photo-DSC analysis of formulations consisting of 1 mol% **TPO**, **TPO-L**, and **4** in UDMA at room temperature using 385 nm LED irradiation.*

Sample	t_{max} [s]	Height [mW/mg]	$t_{95\%}$ [s]	Area [J/g]	DBC [%]	R_p [mmol $s^{-1}L^{-1}$]
TPO	8.13 ± 0.09	21.8 ± 0.6	34.4 ± 0.4	185 ± 3	77.7 ± 1.5	216 ± 6
TPO-L	8.77 ± 0.39	19.5 ± 1.0	32.7 ± 0.0	180 ± 7	75.3 ± 3.1	194 ± 9
4	9.00 ± 0.10	18.0 ± 1.2	48.7 ± 0.8	181 ± 7	75.6 ± 2.9	178 ± 12

As evident from the data presented in Table 2 and Figure 28, the time required to reach the peak maximum is the shortest for **TPO**, followed by **TPO-L** and **4**. When comparing the peak heights, which indicate the rate of polymerization, **TPO** once again demonstrates better performance, followed by **TPO-L** and **4**. This is represented graphically in Figure 29.

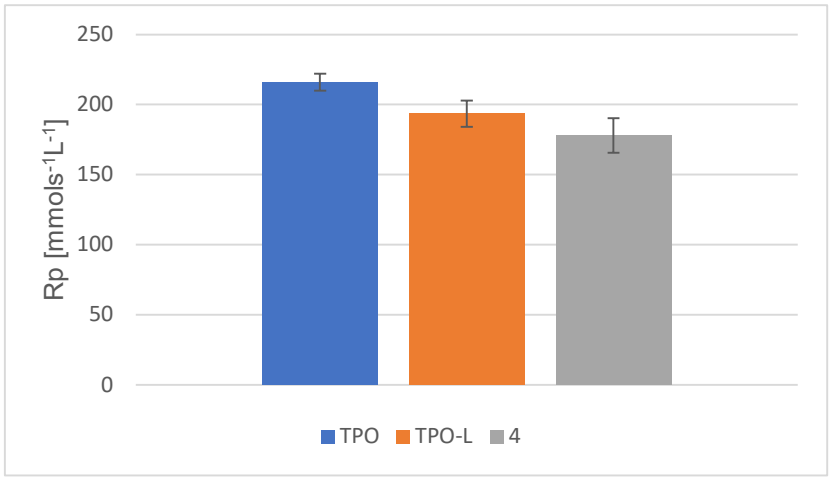

*Figure 29: Comparison of Rp values for **TPO**, **TPO-L,** and **4** obtained from photo-DSC measurements conducted with 385 nm LED irradiation.*

Regarding the results for the peak area and consequently the double bond conversion (DBC), **TPO** continues to exhibit the best performance. However, when comparing **TPO-L** and **4**, a notable similarity in performance can be observed. Photoinitiator **4** outperformed **TPO-L** slightly when comparing the achieved DBC. These results are represented in Figure 30.

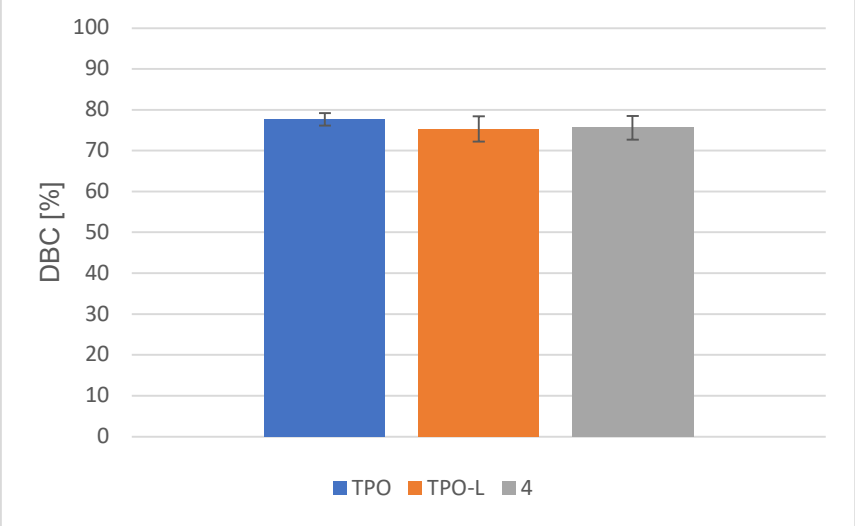

*Figure 30: Comparison of DBC values for **TPO**, **TPO-L** and **4** obtained from photo-DSC measurements conducted with 385 nm LED irradiation.*

These results can be explained through the analysis of conducted UV-Vis measurements (Figure 24). It was expected for **TPO** to outperform the other two photoinitiators, given its absorption maximum at 380 nm. This characteristic makes **TPO** highly sensitive to the employed light source with a wavelength of 385 nm. A similar rationale can be applied to interpret the results of **TPO-L** and **4**. **TPO-L** has an absorption maximum of 370 nm, while **4** shows its peak at 390 nm.

Finally, these results suggest that the photoinitiator **4** compared to **TPO-L** shows a slightly better efficiency in monomer conversion, however despite achieving the higher DBC, the lower rate of polymerization would suggest that the initiation process is proceeding slower with **4** than **TPO-L**.

Photo-DSC study using 405 nm LED irradiation.

The next study that was performed was with a 405 nm irradiation source. The measurement conditions were the same: the polymerizations were performed at room temperature, under a nitrogen atmosphere (20mLmin^{-1}), and for 300 s. However, while using the 405 nm LED spotlight source intensity of 60 mW/cm^2 could not be achieved. Therefore, this measurement was performed with an intensity of 36.6 mW/cm^2. In Figure 31 represented are the results of this measurement.

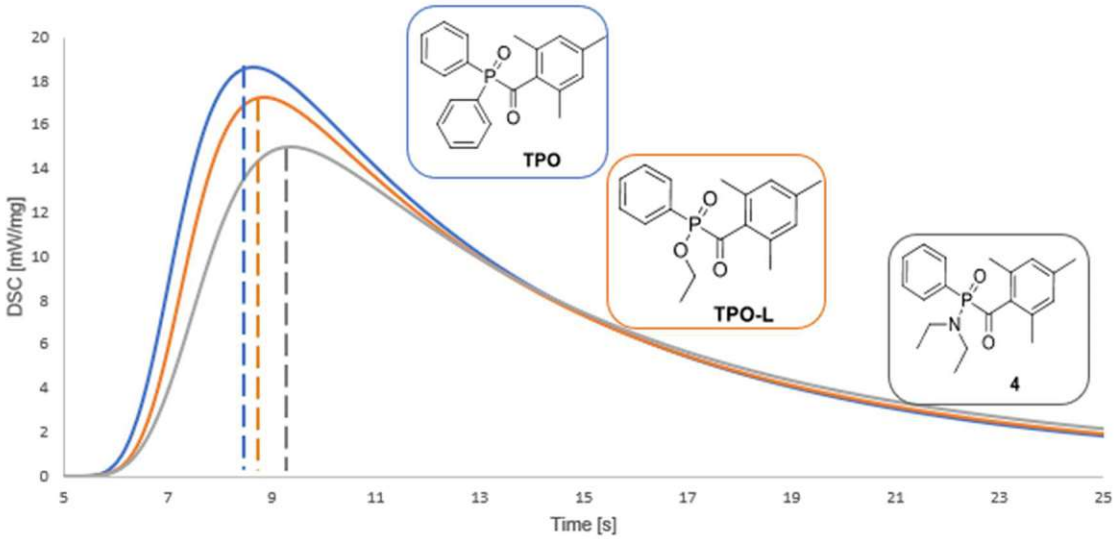

*Figure 31: Photo-DSC analysis of formulations consisting of 1 mol% **TPO** (blue), **TPO-L** (orange), and **4** (grey) in UDMA at room temperature using 405 nm LED irradiation.*

As Figure 31 represents, the best-performing photoinitiator under these measuring conditions was **TPO**, followed by **TPO-L,** and lastly **4**. Further collected data is represented in the following Table 3.

*Table 3 Photo-DSC analysis of formulations consisting of 1 mol% **TPO**, **TPO-L,** and **4** in UDMA at room temperature using 400 nm LED irradiation.*

Sample	t_{max} [s]	Height [mW/mg]	$t_{95\%}$ [s]	Area [J/g]	DBC [%]	R_p [mmol s^{-1}L^{-1}]
TPO	8.73 ± 0.09	18.7 ± 0.4	38.1 ± 0.5	172 ± 3	72.0 ± 1.3	185 ± 4
TPO-L	8.90 ± 0.14	18.2 ± 0.8	36.2 ± 0.8	161 ± 3	67.5 ± 1.1	180 ± 7
4	9.33 ± 0.05	16.1 ± 1.0	41.8 ± 1.1	158 ± 5	66.3 ± 2.1	160 ± 10

When comparing the peak heights of the photoinitiators, which directly correspond to the rate of the polymerization, it is evident that **4** exhibits significantly lower performance compared to both **TPO** and **TPO-L**. The calculated rate of polymerization for the three photoinitiators is represented in the following Figure 32.

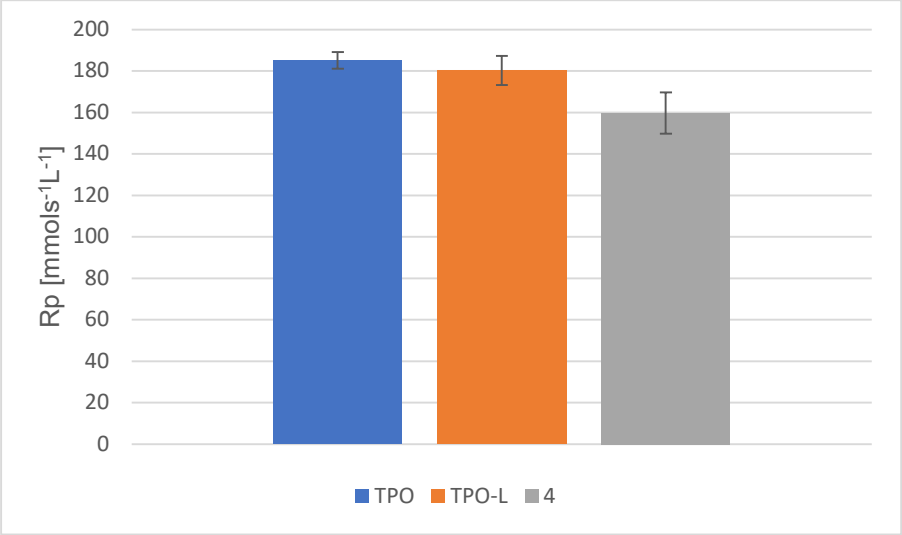

*Figure 32: Comparison of Rp values for **TPO**, **TPO-L,** and **4** obtained from photo-DSC measurements conducted with 400 nm LED irradiation.*

This trend is consistent when evaluating the peak areas and DBC. However, a similarity of **TPO-L** and **4** can be observed once again. The results for the calculated DBCs are represented in Figure 33.

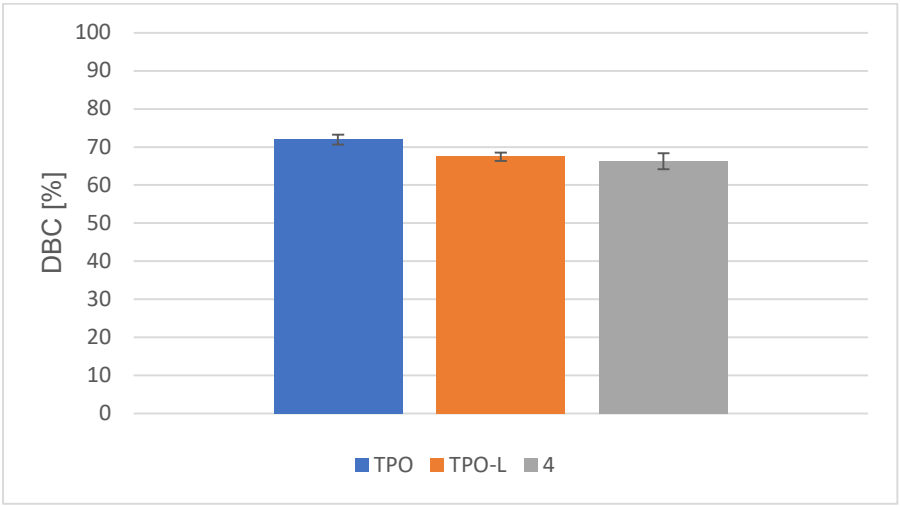

*Figure 33: Comparison of DBC values for **TPO**, **TPO-L,** and **4** obtained from photo-DSC measurements conducted with 400 nm LED irradiation.*

Given that photoinitiator **4** has an absorption maximum of 390 nm, while the irradiation source has a wavelength of 405 nm, the observed results were unexpected, particularly the outperformance by **TPO-L**. The analyzed data indicate that photoinitiator **4** shows

lower efficiency in converting monomers to polymers, as demonstrated by a lower double bond conversion. Moreover, the rate of polymerization for photoinitiator **4** is considerably slower compared to **TPO-L**.

To understand this behavior of photoinitiator **4**, further investigation into its quantum yield should be performed, and this can be achieved through steady-state photolysis. This additional analysis can provide insight into the efficiency of the photoinitiator in initiating the polymerization and may explain the observed behavior.

1.2.1.4 Steady state photolysis

When irradiated with light of suitable wavelength, the Type I photoinitiators undergo α-cleavage and form radical species that can start polymerization. To investigate the efficiency of the photoinitiator, α-cleavage and quantum yield of decomposition play an important role.[18] The quantum yield represents the number of events (reactions) that occur per absorbed photon.[18] Therefore, through determining quantum yield, information about the efficiency of photoinitiator to initiate the desired photochemical reaction can be obtained.

Since the current methods for determining the quantum yields are very complicated, expensive and suffer from some shortcomings, Stadler et al.[18] report a new setup that should help to overcome these disadvantages.[18] They introduced a novel setup for assessing quantum yields via online UV-Vis spectroscopy.

The α-cleavage of **MAPO** photoinitiators **TPO**, **TPO-L** and **4** was followed by online UV-Vis spectroscopy in order to determine their quantum yields.

For the calculation of quantum yield the Equation 3 was used.

$$\Phi = \frac{k_{fit} c_0}{I_0 (1 - 10^{-A_i})}$$

Equation 3: Quantum yield calculation[18]

Φ: *quantum yield of the photoinduced conversion*
k_{fit}: *decay constant obtained by exponential fitting of the absorbance trace [s^{-1}]*
c_0: *starting concentration of the solutions [M]*
I_0: *initial light intensity [$molL^{-1}s^{-1}$]*
A_i: *absorbance at the irradiation wavelength*

Initial light intensity at specific wavelength (I_0, LED light source) that starts the photoreaction, can be determined by using a suitable chemical actinometer. Ferrioxalate actinometer is a standard tool for photochemical investigations.[18] This actinometer is widely researched and has some great advantages like high sensitivity and precision as well as long wavelength absorption (used usually between 200 and 450 nm)[42,43].

To determine photon flow of the used LED source, the actinometric measurements with potassium ferrioxalate actinometer were performed following research of Lehóczki et al.[42] Firstly, the potassium ferrioxalate was recrystallized two times from water, and the

crystals dried under vacuum. For the measurements, 1 mg of solid potassium ferrioxalate $K_3[Fe(C_2O_4)_3]\cdot 3H_2O$ was dissolved in 2.5 mL of 0.05 M H_2SO_4 solution. After measuring the background (0.05 M H_2SO_4 solution), the actinometer solution was placed directly into the cuvette and irradiated with the light source (385 or 405 nm). For each measurement, fresh actinometric solution was prepared. When the solution is irradiated the intensity of the original spectrum decreases based on the decomposition reaction and the photon flow of the used LED can be obtained with Equation 4.[42]

$$I_0 = \frac{slope}{\varepsilon_{obs}\Phi}$$

Equation 4: Initial light intensity calculation[18]

I_0: *initial light intensity at a specific wavelength [molL^{-1}s^{-1}]*
$slope$: *represents absorbance/time dependence that is proportional to the initial rate of absorbance change for the process. [s^{-1}]*
ε_{obs}: *extinction coefficient at the observation wavelength [Lcm^{-1}mol^{-1}]*
Φ: *quantum yield of actinometer conversion []*

To characterize the rate of photochemical reaction, the change in absorbance at one selected wavelength with irradiation time can be used. The choice of this wavelength should be based on the best signal-to-noise ratio. The linear fit of these data can provide us with the *slope* of the curve that is identical to the initial rate of absorbance change for the process.[42] The extinction coefficient at the observation wavelength (ε_{obs}) was determined by Lambert-Beer Equation (optical path length: 1 cm).

The quantum yield of ferrioxalate actinometer conversion (Φ) at 385 and 405 nm was addressed both in Stadler et al. and Lehóczki et al. In order to determine the photon flow of the LED light source, Lehóczki et al.[42] uses the quantum yield Φ=1.2. Stadler et al.[18] tested the use of Φ=1.2 and showed a very good agreement between actinometric measurement and spectrophotometric determinations and therefore justified the use of this value.[18] For the 405 nm LED, Φ=1.14 was used.[18,42]

The quantum yield determination of **TPO**, **TPO-L** and **4** with 385 and 405 nm LED was performed using the above-described formulas.

Steady State photolysis with 385 nm LED

In order to determine the photon flow of the used 385 nm LED irradiation source, Equation 4 was used. The measurement results of the actinometric solution with 385 nm LED are represented in Figure 34.

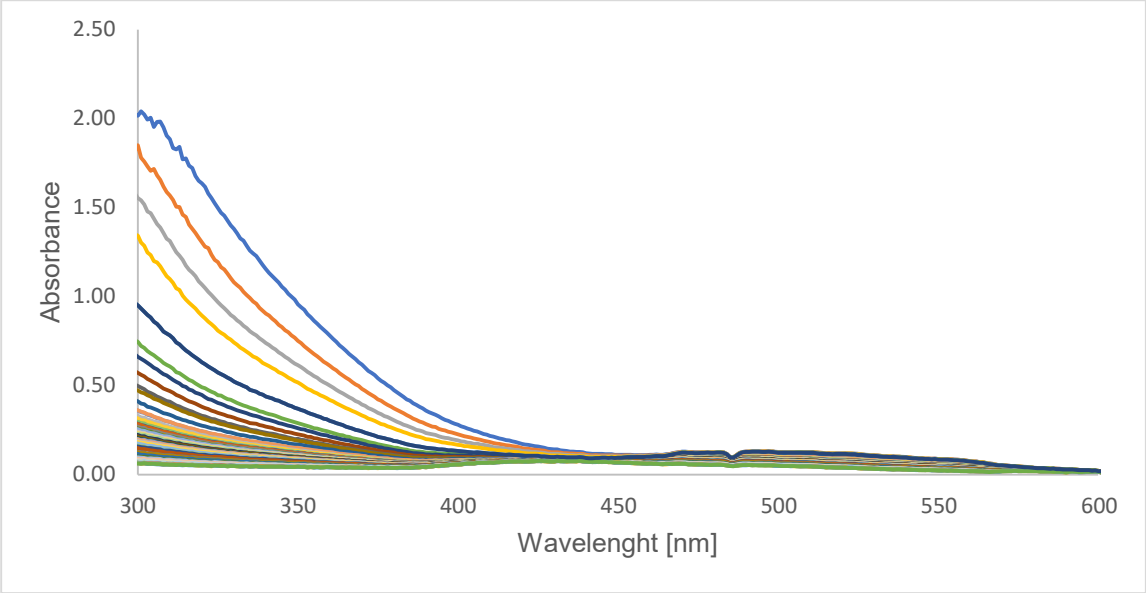

Figure 34: Spectral changes of the actinometer during a 5 min irradiation with 385 nm LED. The irradiated volume was 2 mL consisting of 0.8 mM solution of $K_3[Fe(C_2O_4)_3]\cdot 3H_2O$ in 0.05 M H_2SO_4.

The observational wavelength was 380 nm, since it showed the best signal-to-noise ratio. The change in absorbance of ferrioxalate actinometer during the 5 min irradiation at 380 nm is represented in Figure 35. The insert shows the data that were used for the calculation of the photon flow.

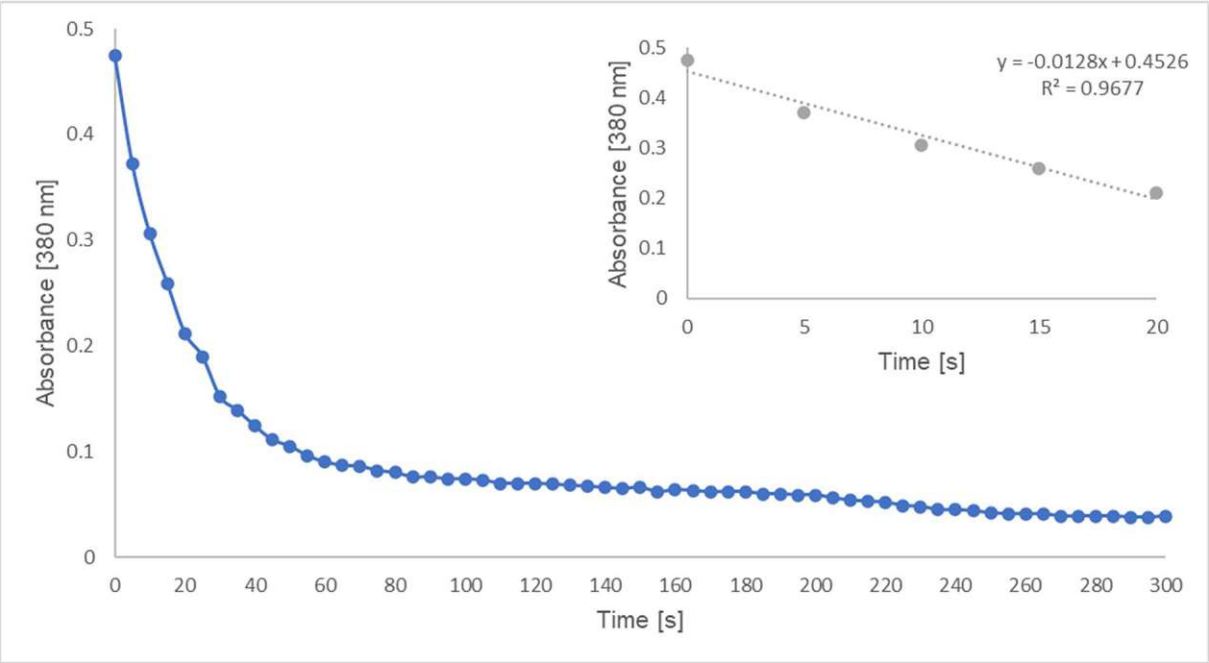

Figure 35: Absorbance changes at 380 nm during 5 min irradiation time used for ferrioxalate actinometry. The insert shows the region between 0 and 20 s in more detail and the linear fit used to calculate the light intensity.

The results of the measurement are summarized in Table 4.

Table 4: Results of actinometric measurements with 385 nm LED

c [M]	λ_{obs} [nm]	A_{obs} (at 380 nm)	ε_{obs} [$Lcm^{-1}mol^{-1}$]	$\phi^{18,42}$ []	slope [s^{-1}]	I_0 [$molL^{-1}s^{-1}$]
0.001	380	0.47	583	1.2	0.0128	**$1.83\ 10^{-5}$**

Using the value of calculated photon flux for 385 nm LED I_0 (Table 4) the quantum yields of **TPO**, **TPO-L** and **4** were determined according to Equation 3. Since upon the irradiation of **MAPO**s the characteristic nπ* band decays, the change in absorbance over time was followed at absorption maxima of **TPO** (380 nm), **TPO-L** (370 nm) and **4** (390 nm). The spectral changes were recorded every 5 s. The parameter k_{fit} was determined by the exponential fitting of the absorbance/time traces at these wavelengths.

The spectral changes of **TPO** observed when irradiated with 385 nm are represented in Figure 36. In insert, the change in absorbance over time at the chosen wavelength (380 nm) is shown.

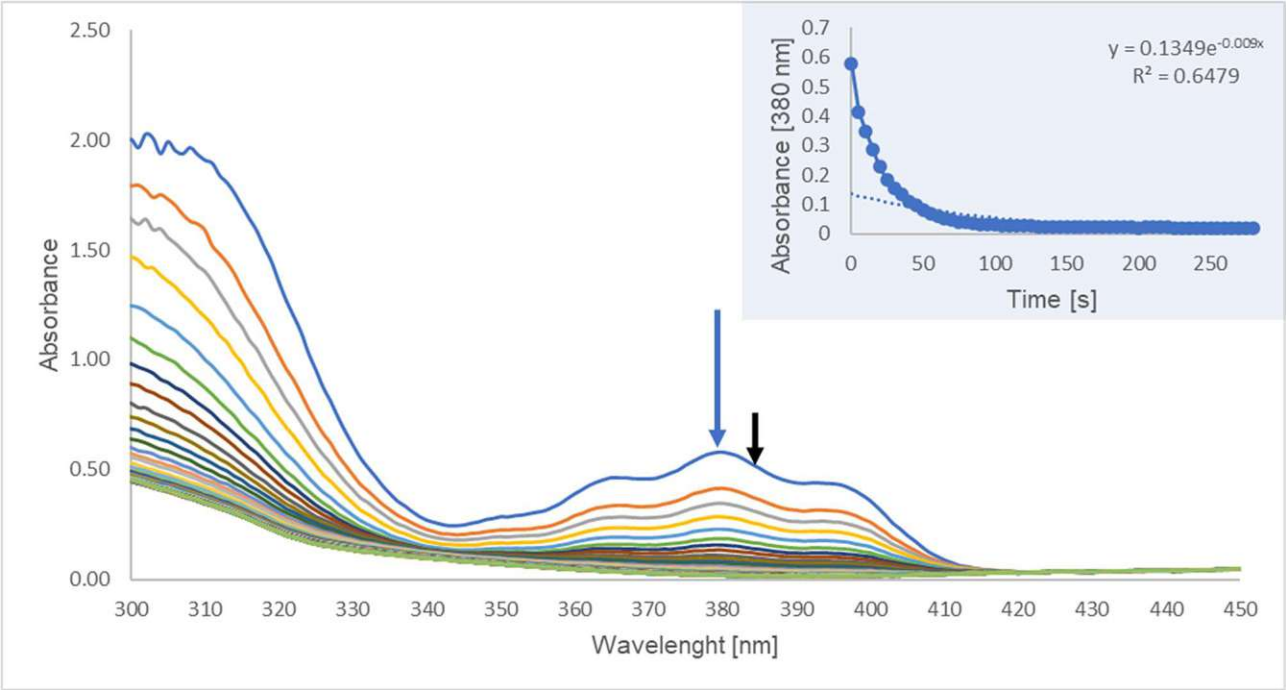

*Figure 36: Spectral changes of **TPO** when irradiated with 385 nm (black arrow) LED. Time steps between each spectrum 5 s. The insert shows the decay of absorbance with irradiation time at 380 nm (blue arrow). Sample: 2 mL of 0.001 M **TPO** in acetonitrile.*

As visible in Figure 36, the decrease of the nπ* band of **TPO** at 380 nm (blue arrow) occurs very fast. When looking at the insert, in the first 5 seconds of measurement a noticeable decay in absorbance occurs.

The spectral changes of **TPO-L** when irradiated with 385 nm are represented in Figure 37. The observational wavelength for following the nπ* band was 370 nm.

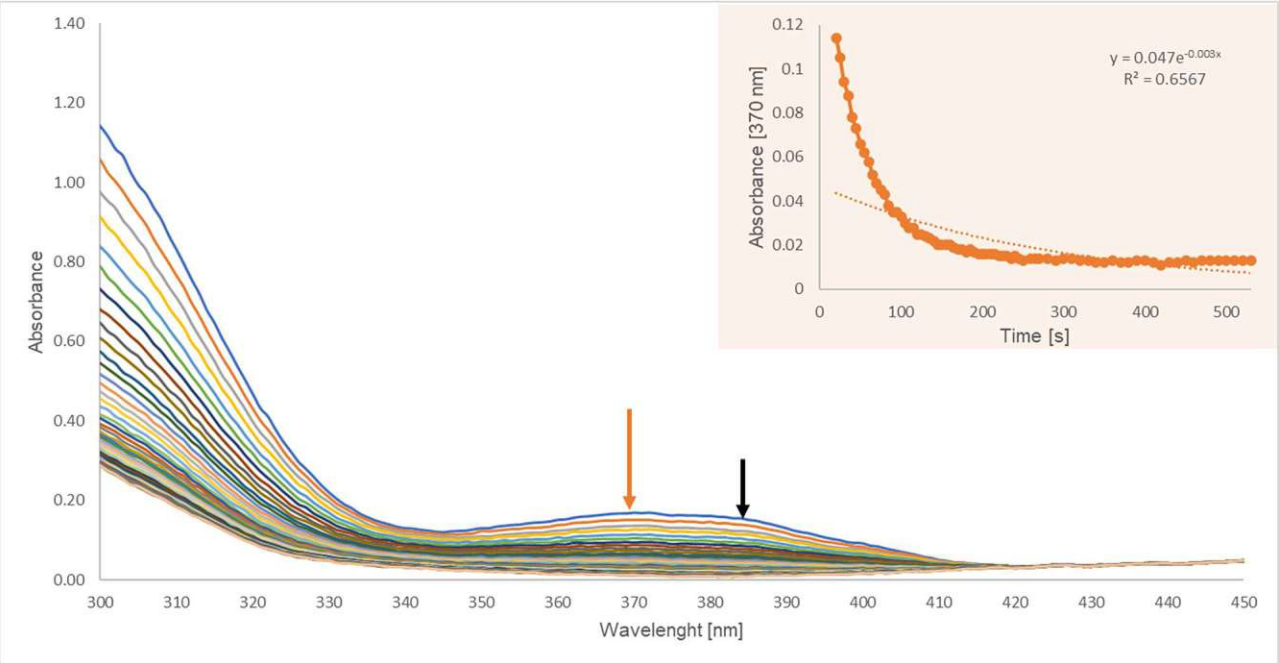

*Figure 37: Spectral changes of **TPO-L** when irradiated with 385 nm (black arrow) LED. Time steps between each spectrum 5 s. The insert shows the decay of absorbance with irradiation time at 370 nm (orange arrow). Sample: 2 mL of 0.001 M **TPO-L** in acetonitrile.*

The same measurements were performed with **4.** The spectral changes during the irradiation with 385 nm are represented in Figure 38. The decay of nπ* band for **4** was followed at 390 nm.

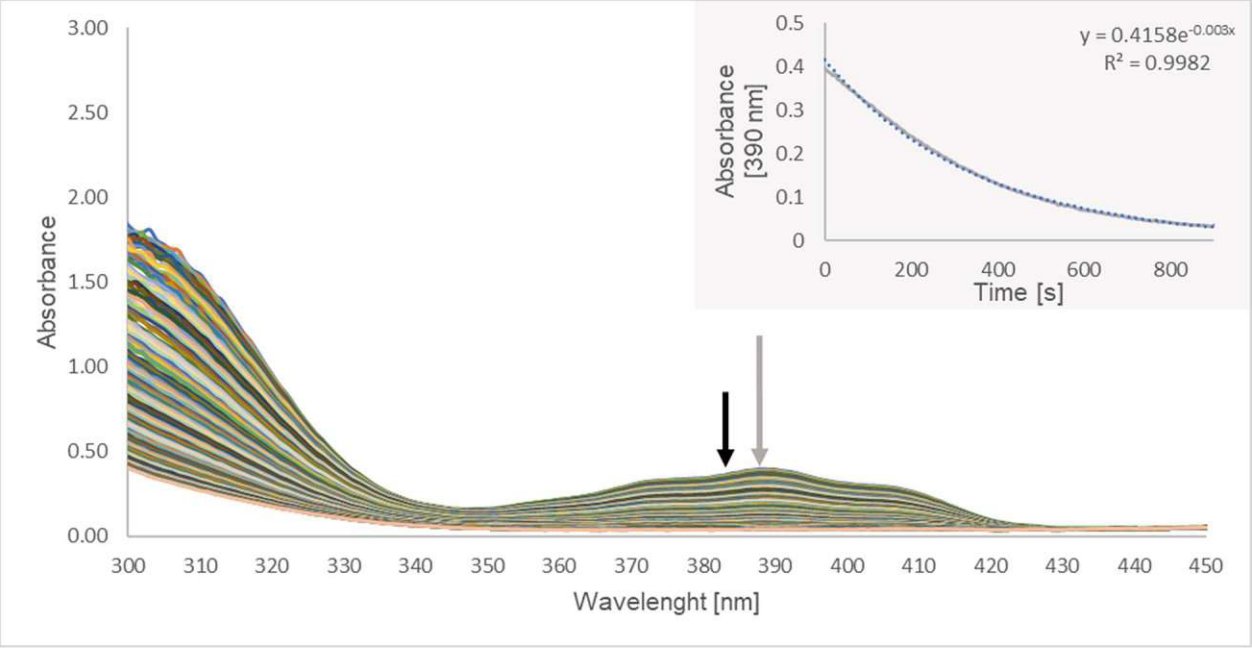

*Figure 38: Spectral changes of **4** when irradiated with 385 nm (black arrow) LED. Time steps between each spectrum 5 s. The insert shows the decay of absorbance with irradiation time at 390 nm (grey arrow). Sample: 2 mL of 0.001 M **4** in acetonitrile.*

The results of the measurements for **TPO** (Figure 36), **TPO-L** (Figure 37) and **4** (Figure 38) are summarized in Table 5.

*Table 5: Results for quantum yield determination of **TPO**, **TPO-L** and **4**, irradiated with 385 nm LED.*

	λ_{obs} [nm]	$A_{i'}$ (at 385 nm)	c_0 [M]	I_0 [molL^{-1}s^{-1}]	k_{fit} [s^{-1}]	Φ []
TPO	380	0.507	0.001	1.83 10^{-5}	0.009	0.715
TPO-L	370	0.151	0.001		0.003	0.559
4	390	0.378	0.001		0.003	0.282

The calculated values for the quantum yields are in a very good agreement with photo-DSC results performed with 385 nm LED (Figure 28). **TPO** shows the highest reactivity, followed by the **TPO-L** and **4**. To compare the photoinitiators, the exponential fit of the recorded data was considered for 900 s for all photoinitiators. However, according to the reached signal-to-noise ratios, it can be concluded that the measurements of **TPO** and **TPO-L** need to be measured in intervals shorter than 5 s. In case of **4**, the exponential fit was with 0.999 ideal.

This can also be observed when the absorbance decay at the corresponding absorption wavelengths within the first 50 s of irradiation are compared. As visible in Figure 39, **TPO** has almost completely decomposed within the first 50 s of irradiation. In comparison, **4** shows a very slow decomposition and almost no change in absorbance at 390 nm in this time frame.

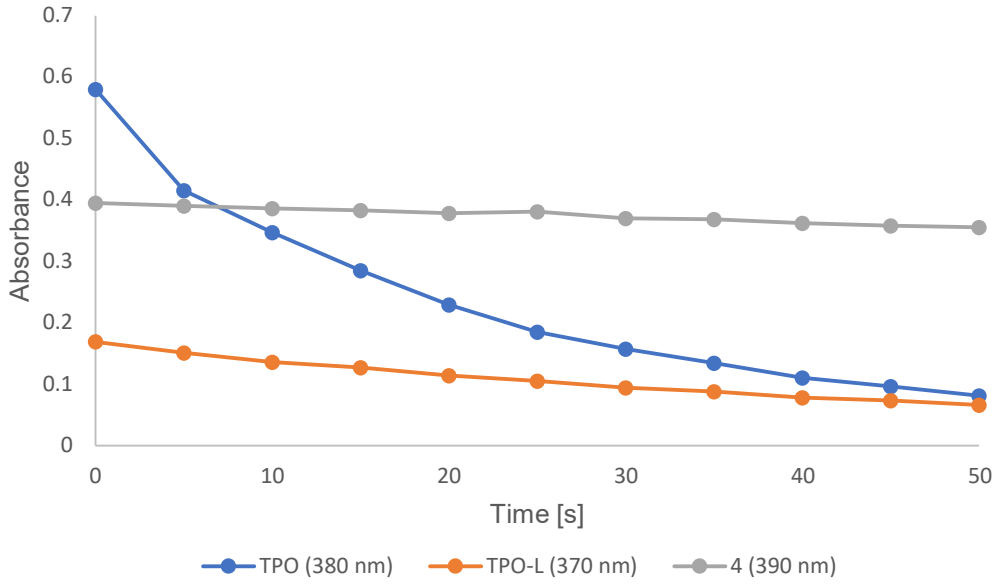

*Figure 39: Spectral changes within the first 50 s irradiation of **TPO** (380 nm), **TPO-L** (370 nm) and **4** (390 nm) when irradiated with 385 nm LED. Time steps between each spectrum 5 s.*

Steady State photolysis with 405 nm LED

The next steady state photolysis experiment was performed with a 405 nm LED. The actinometric measurements were analyzed using Equation 4. The spectral change of actinometer while measuring with 405 nm LED is represented in Figure 40.

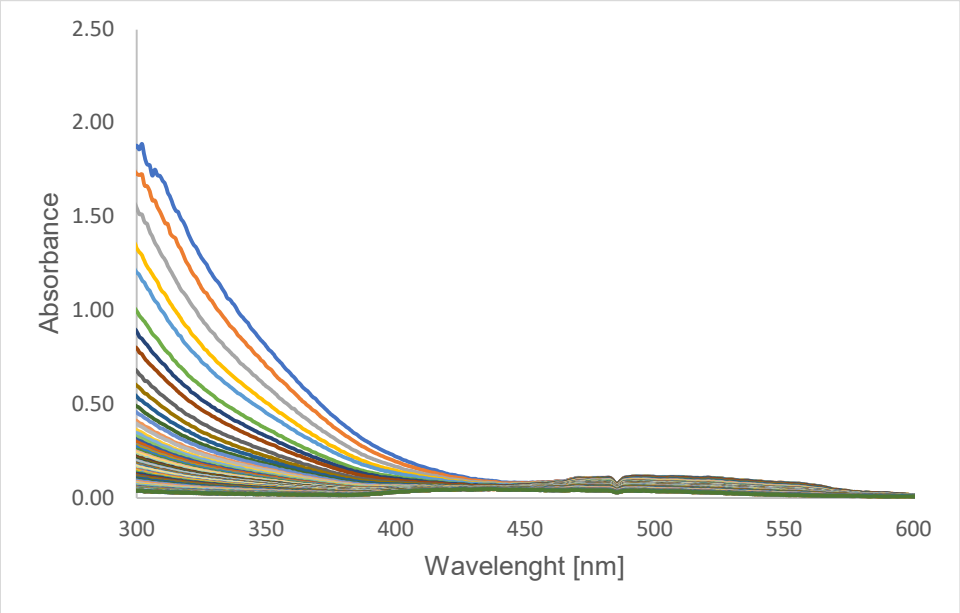

Figure 40: Spectral changes of the actinometer during a 5 min irradiation with 405 nm LED. The irradiated volume was 2 mL consisting of 0.8 mM solution of $K_3[Fe(C_2O_4)_3]\cdot 3H_2O$ in 0.05 M H_2SO_4.

The parameters needed for calculation of LED photon flow were determined at 390 nm. The spectral change at observed wavelength is represented in Figure 41 and summarized in Table 6.

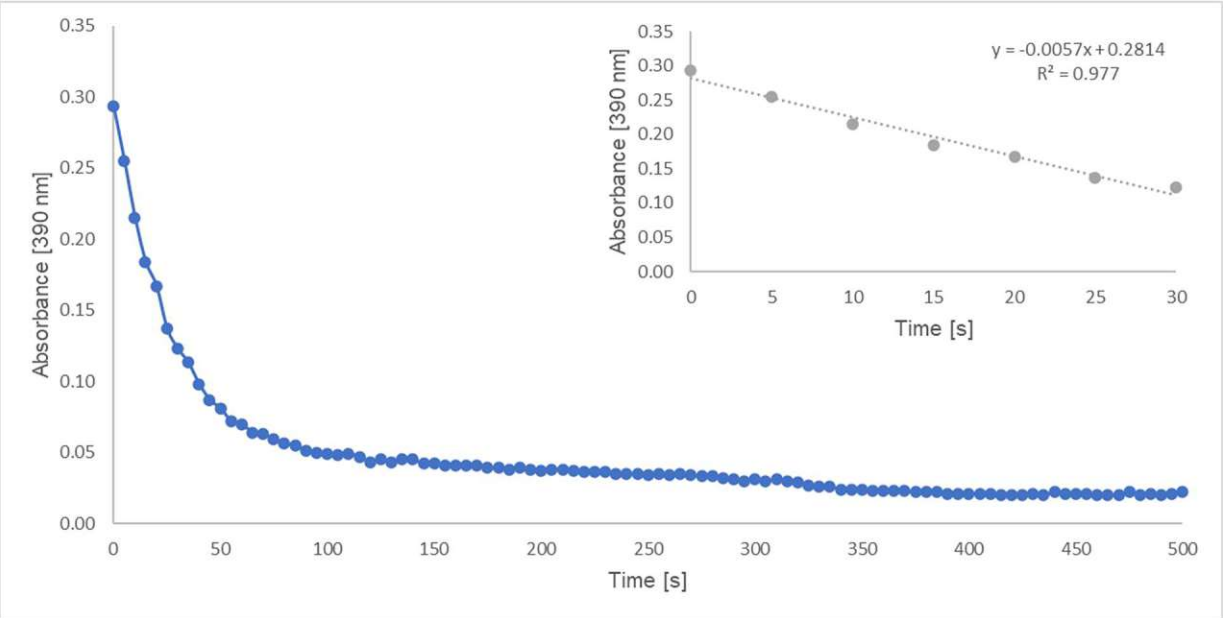

Figure 41: Absorbance changes at 390 nm during 8 min irradiation time used for ferrioxalate actinometry. The insert shows the region between 0 and 20 s in more detail and the linear fit used to calculate the light intensity.

The results of the actinometric measurements are represented in Table 6.

Table 6: Results of actinometric measurements with 405 nm LED

c [M]	λ_{obs} [nm]	A_{obs} (at 390 nm)	ε_{obs} [$Lcm^{-1}mol^{-1}$]	$\Phi^{18,42}$ []	Slope [s^{-1}]	I_0 [$molL^{-1}s^{-1}$]
0.001	390	0.293	360	1.14	0.0057	**$1.39\ 10^{-5}$**

The quantum yields of **TPO**, **TPO-L** and **4** were calculated based on the measured photon flux at 405 nm (Table 6), by using Equation 3. The decay in nπ* band was once again followed at the absorption maxima of **TPO** (380 nm), **TPO-L** (370 nm) and **4** (390 nm). Spectral changes were recorded at intervals of 5 seconds. The parameter k_{fit} was determined by fitting the absorbance/time traces at these wavelengths using an exponential function.

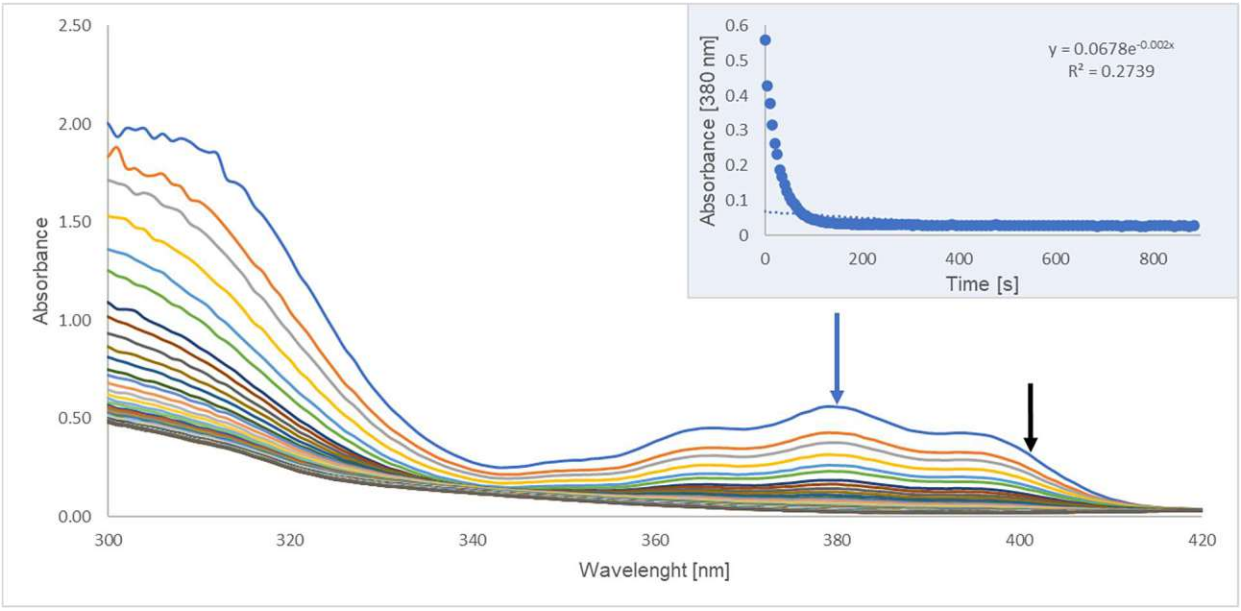

*Figure 42 Spectral changes of **TPO** when irradiated with 405 nm (black arrow) LED. Time steps between each spectrum 5 s. The insert shows the decay of absorbance with irradiation time at 380 nm (blue arrow). Sample: 2 mL of 0.001 M **TPO** in acetonitrile.*

As visible in Figure 42 the nπ* band decay does not occur as fast as with 385 nm LED light source (Figure 36). Furthermore, a slower decay in absorbance with time compared to the one occurring with 385 nm LED is visible as well. The spectral changes of **TPO-L** are represented in Figure 43.

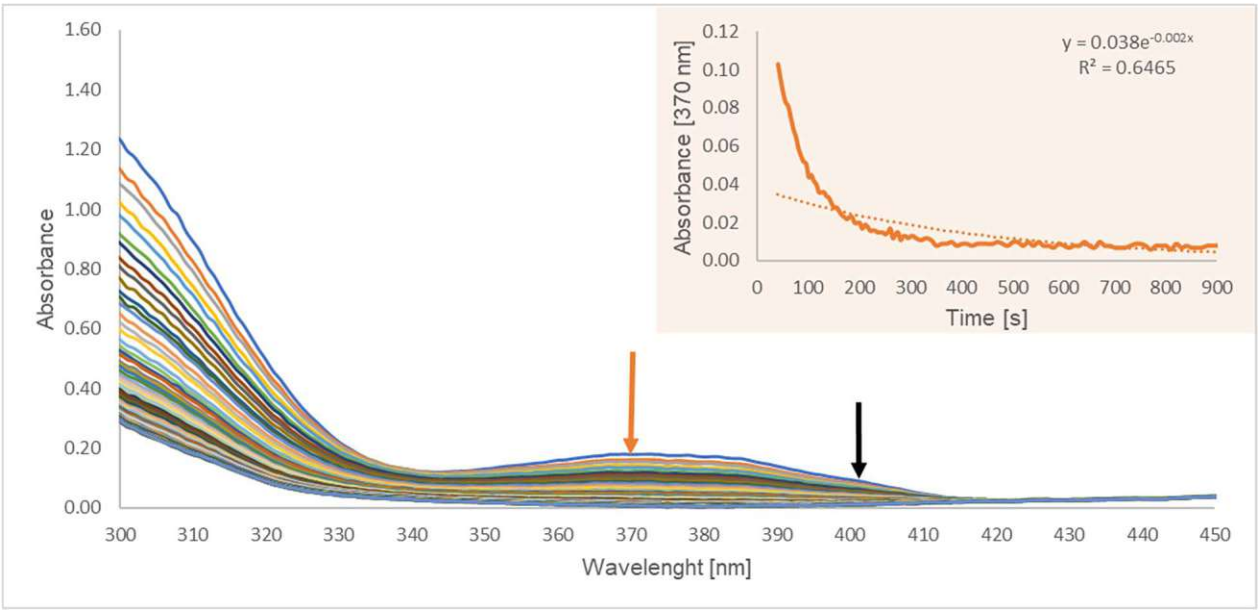

*Figure 43: Spectral changes of **TPO-L** when irradiated with 405 nm (black arrow) LED. Time steps between each spectrum 5 s. The insert shows the decay of absorbance with irradiation time at 370 nm (orange arrow). Sample: 2 mL of 0.001 M **TPO-L** in acetonitrile.*

In the following Figure 44 the recorded changes in absorbance of **4** are represented.

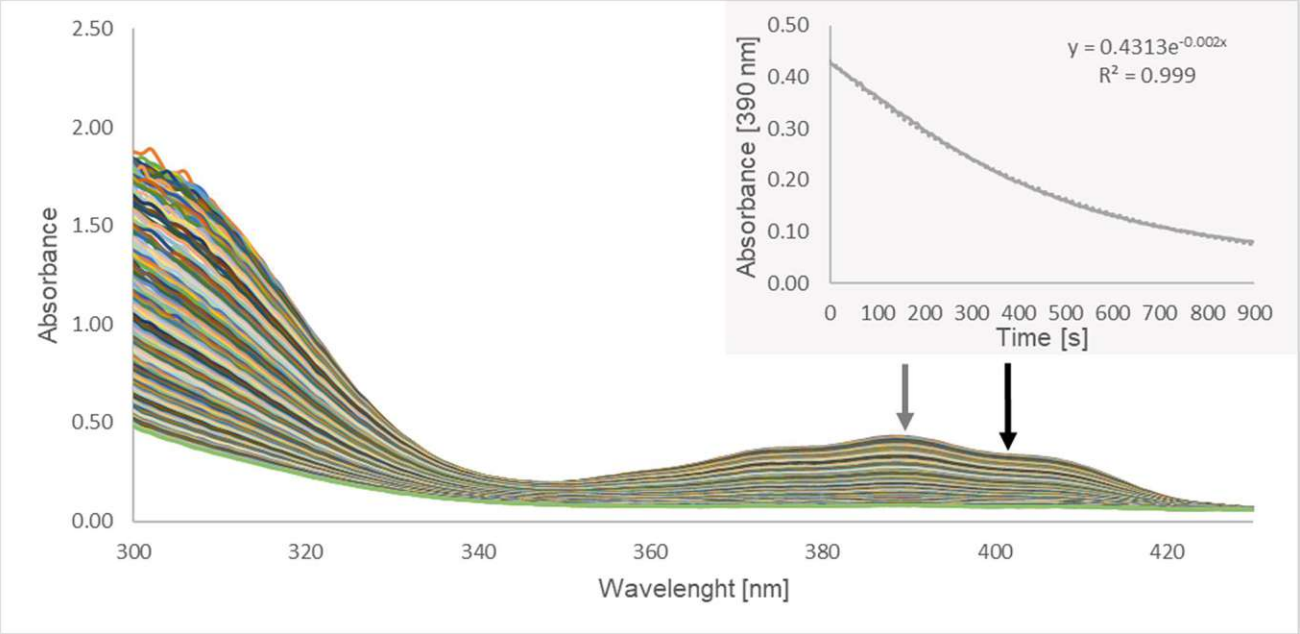

*Figure 44: Spectral changes of **4** when irradiated with 405 nm (black arrow) LED. Time steps between each spectrum 5 s. The insert shows the decay of absorbance with irradiation time at 390 nm (grey arrow). Sample: 2 mL of 0.001 M **4** in acetonitrile.*

The data collected from the performed measurements are summarized in Table 7.

*Table 7: Results for quantum yield determination of **TPO**, **TPO-L** and **4**, irradiated with 405 nm LED.*

	λ_{obs} [nm]	$A_{i'}$ (at 405 nm)	c_0 [M]	I_0 [molL^{-1}s^{-1}]	k_{fit} [s^{-1}]	ϕ []
TPO	380	0.197	0.001	1.39 10^{-5}	0.002	0.395
TPO-L	370	0.071	0.001		0.002	0.954
4	390	0.326	0.001		0.002	0.273

According to the collected data represented in Table 7 the highest reactivity under the measuring conditions is achieved with **TPO-L**. These results however are not in good agreement with the performed photo-DSC measurements, which have shown that **TPO** outperforms **TPO-L** in measurements with 405 nm LED. Furthermore, when comparing the curve trajectory in Figure 45 it is once again obvious that the decline in absorbance for **TPO** occurs much faster than for **TPO-L** or **4**. The higher results for **TPO-L** can be explained by a very low absorbance that this photoinitiator has at the irradiation wavelength of 405 nm which has directly influenced the results of quantum yield (Equation 3).

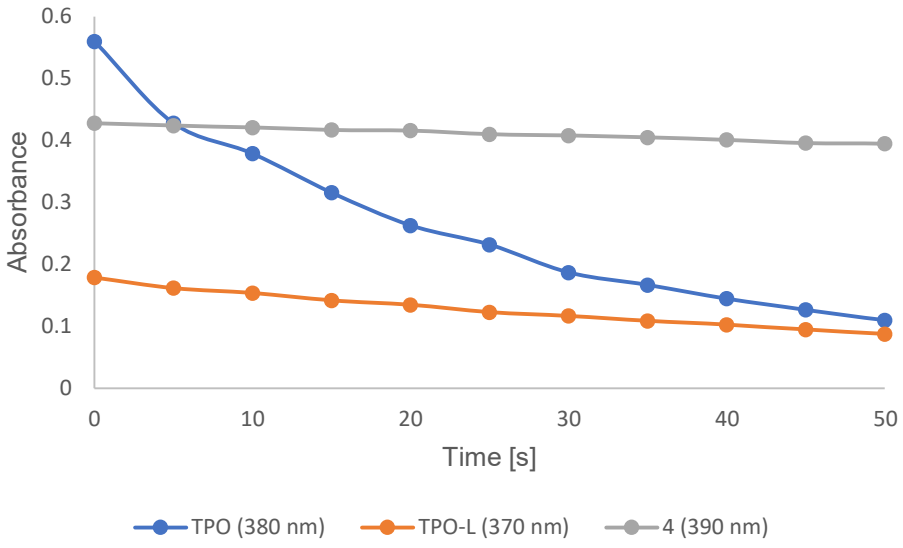

Figure 45: Spectral changes within the first 50 s irradiation of TPO (380 nm), TPO-L (370 nm) and 4 (390 nm) when irradiated with 405 nm LED. Time steps between each spectrum 5 s.

The photoinitiator **4** shows once again the lowest efficiency when compared to **TPO** and **TPO-L**. Furthermore, compatible with photo-DSC, **4** shows a slightly higher reactivity when irradiated with 385 nm LED.

When comparing the results of performed analysis methods: UV-Vis spectroscopy, photo-DSC and steady state analysis, it can be concluded that compared to well-established **MAPO**s, **TPO** and **TPO-L**, **4** shows a much lower performance and efficiency in initiating a polymerization.

However, photoinitiator **4** displayed a noticeable 10 nm redshift when compared to **TPO**. This observation inspired further investigation of potential nitrogen substituents on phosphorus.

Moreover, considering that **TPO,** with its sterically demanding phenyl ring, outperformed **TPO-L** and **4**, both of which have less sterically demanding moieties, the investigation into nitrogen substituents with greater steric hindrance was pursued.

1.2.2 Phosphinic acid amide **5**

Since **4** showed a bathochromic shift but did not perform as well as **TPO**, the next **MAPO**-based molecules that were researched were the ones containing more sterically demanding nitrogen substituents than diethyl amine. Since the sterical hindernice on phosphorus directly influences the stability of the formed radical species and therefore its efficiency in initiating the polymerization process, investigation of these molecules should provide us with new insights. For this purpose, diisopropyl amine was chosen. The synthesis of **5** was performed following the previously described procedure by Roszkowski et al. for synthesis of **4**.

1st attempt

The reaction was performed under the same conditions as the synthesis of **4**: at room temperature, under an inert atmosphere, and for 1 h. To the solution of the corresponding amine in toluene, a solution of **3** in toluene was added dropwise. Reaction control was performed with ^{31}P-NMR and UPLC-MS.

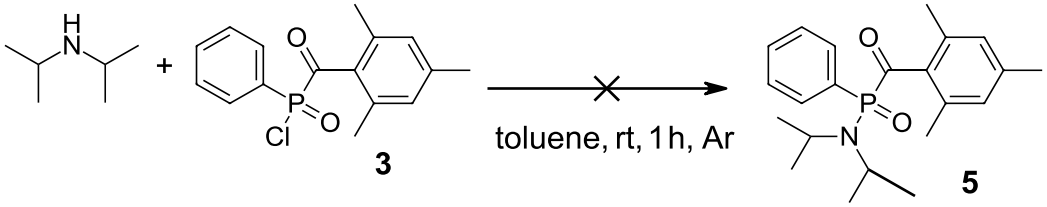

In the initial attempt, an equimolar amount of amine and **3** was used. The reaction progress was monitored using ^{31}P-NMR (Figure S 14), which allowed the identification of several compounds, including the starting acid chloride **3**, the hydrolysis product **2**, and a byproduct formed during the reaction. The analysis of the reaction mixture was also carried out using UPLC-MS (Figure 46).

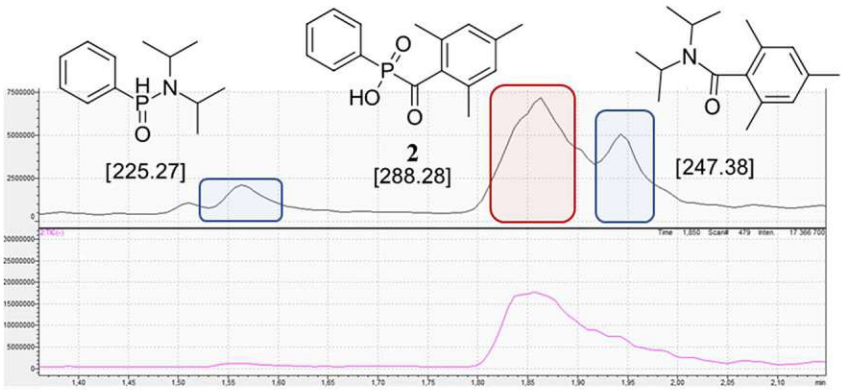

*Figure 46: UPLC-MS of the reaction mixture **6**. (Equimolar amounts of **6** and **3**)*

The UPLC-MS measurement confirmed the presence of the two byproducts resulting from the nucleophilic cleavage, illustrated in Figure 47.

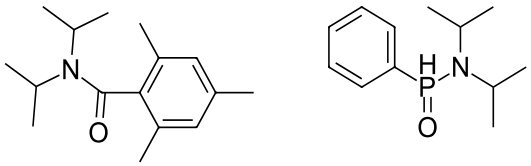

*Figure 47: Byproducts of nucleophilic cleavage found in UPLC-MS during the synthesis of **6**.*

The same synthesis was performed with 3 eq. of diisopropyl amine, and the measurements of ^{31}P-NMR were conducted at two points: after 1 h and 20 h of the reaction. In both instances, ^{31}P-NMR (Figure S 15) showed that the initial compound **3** remained unconsumed throughout the reaction. Additionally, UPLC-MS (Figure S 16) analysis confirmed the formation of the cleavage byproducts, consistent with the byproducts represented in Figure 47.

Since the synthesis of **5** following the same procedure used in the synthesis of **4** either yielded the hydrolysis product **2** or cleavage products, a different approach to desired structures was used. The reactions were performed under the same conditions but in this new attempt, the corresponding amine was first reacted with TEA.

2nd attempt

For the second synthesis attempt of **5**, to solution of diisopropyl amine (1 eq.) in toluene, TEA (2 eq.) was added following the addition of precursor **3** (1 eq.). The monitoring of the reaction was performed once again with ^{31}P-NMR.

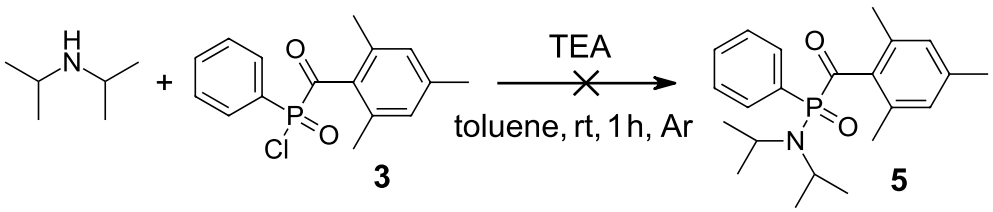

The reaction control showed that after 3 h (Figure S 17) of reaction time, the starting material **3** was not consumed. The reaction continued and the second reaction control was performed after 18 h. The ^{31}P-NMR (Figure S 18) showed a complete consumption of **3**. Therefore, the UPLC-MS measurement was performed, however besides **2**, two byproducts of the nucleophilic cleavage represented in Figure 47 were identified as the main products.

The synthesis of MAPO derivative containing a diisopropyl amine substituent on phosphonyl side of the molecule was unsuccessful. Given the important role of steric properties in nucleophilic substitution, it is evident that the high steric demand of this amine hindered the desired reaction. During both synthesis attempts, the precursor **3** has undergone cleavage in the presence of the nucleophile. To further investigate the influence of more sterically demanding amines than diethylamine, however less demanding than diisopropyl amine, ethyl isopropyl amine was chosen.

1.2.3 Phosphinic acid amide **6**

For the synthesis of ethyl isopropyl amine substituted **MAPO**, two synthesis attempts following the research of Roszkowski et al. were performed.

1st attempt

For the synthesis of **6** 2 eq. of ethyl isopropyl amine were reacted with 1 eq. of **3**. After 1 h of reaction time according to ^{31}P-NMR (Figure S 12) start product **3** was still present in the reaction mixture and the hydrolysis of the starting material **3** to acid **2** occurred.

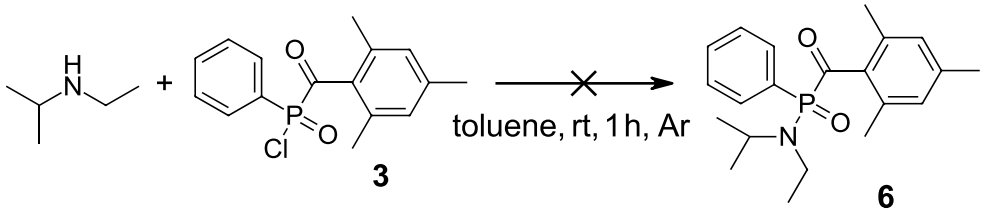

3 **6**

Since this synthesis attempt was unsuccessful, the second attempt to synthesize the desired molecule **6** was performed.

2nd attempt

In the second attempt to synthesize **6**, before the precursor **3** (1 eq.) was added to the reaction mixture, ethyl isopropyl amine (1 eq.) was placed in toluene and reacted with TEA (2 eq.). The monitoring of the reaction progress was performed with ^{31}P-NMR (Figure S 13).

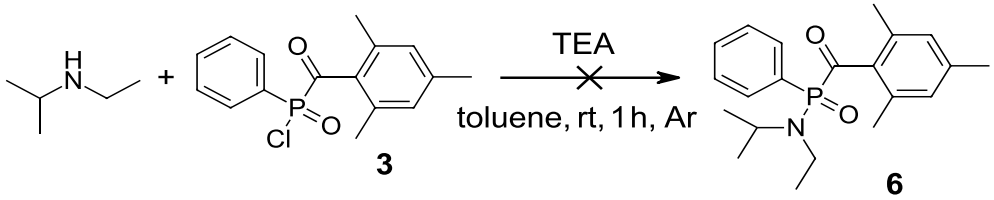

3 **6**

After 1 h of reaction time, the reaction control was performed and **2** was identified as the main product of the reaction. The precursor **3** hydrolyzed during the reaction.

The synthesis of **MAPO** photoinitiators with nitrogen substituents on phosphorus that are more sterically demanding than diethylamine proved unsuccessful. During the synthesis, precursor **3** showed a pattern to either hydrolyze to **2** during the attempted synthesis of **6** or undergo cleavage in the presence of nucleophiles as during the attempted synthesis of **5**.

Since the investigation into new **MAPO** photoinitiators with nitrogen substituents on phosphorus revealed that **4** exhibited performance similar to that of **TPO-L** and efforts to perform nucleophilic substitutions with bulkier amines were unsuccessful, the research shifted its focus toward investigation of alternative phosphorus substituents. Specifically, the potential **MAPO** structures with phosphorus substituents featuring atoms of comparable electronegativity to carbon, as found in **TPO**.

1.3 Sulfur-substituted MAPO (**7**)

The synthesis of new **MAPO** photoinitiators containing sulfur substituents on phosphorus was performed according to Roszkowski et al.[34] The literature reports a successful reaction performed in two steps. In the first step of the reaction deprotonation of thiol with base was performed. This reaction step was followed by the reaction of thiolate and precursor **3**. The research reported no decomposition of the product, but an intermediate yield.

The reaction was performed as nucleophilic substitution on **3** with thiophenol. In the first step of the reaction thiophenol (1.5 eq.) was deprotonated by TEA (2 eq.) and then **3** (1 eq.) was added to the reaction mixture. The monitoring of the reaction was performed with ^{31}P-NMR.

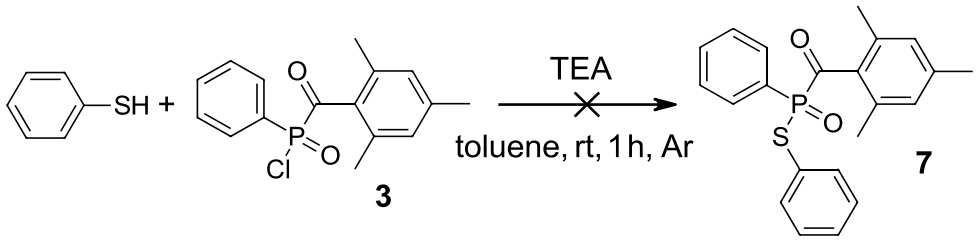

According to ^{31}P-NMR immediately after the addition of **3** to synthesized thiolate the product was formed. This was also confirmed by UPLC-MS (Figure S 25). However, within 15 min of reaction time, the two decomposition products were formed and within an hour of reaction time, the product was fully decomposed. The decomposition of the desired product over time measured by ^{31}P-NMR is represented in Figure 48.

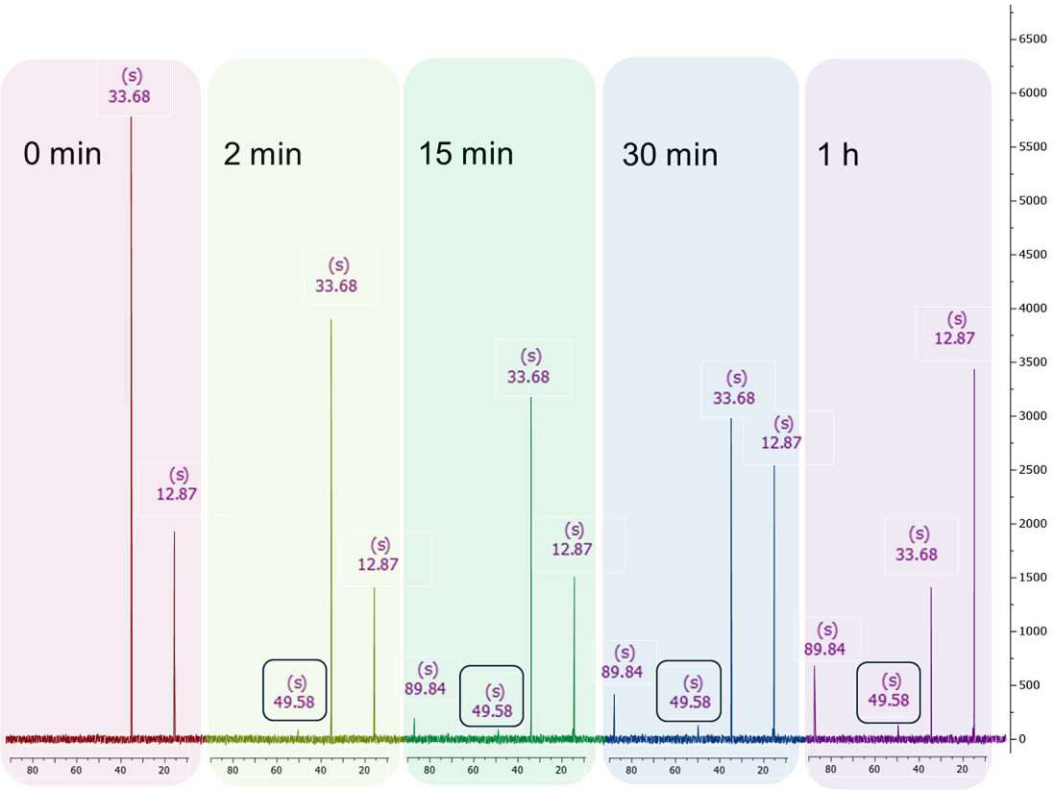

*Figure 48: Monitoring of the reaction over time. The product **7** (33.68 ppm) and by-products (12.87 ppm, 49.58 ppm (Figure 49) and 89.84 ppm).(Figure S 19; Figure S 20; Figure S 21; Figure S 22; Figure S 23)*

One of the side products was identified and confirmed[44] in ^{31}P-NMR and UPLC-MS (Figure S 25). This byproduct is represented in Figure 49.

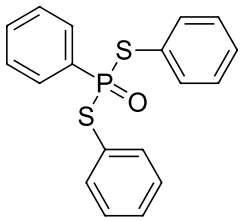

Figure 49: Identified byproduct confirmed by literature. [44]

To purify and quench the reaction, various methods were applied. The goal was to remove the base to stop the further cleavage of the product. However, both aqueous (acidic and neutral conditions) as well as non-aqueous purification methods have led to the decomposition of the product (Figure S 24). Therefore, it was established that the desired product **7** was formed during the reaction, however it is unstable and decomposes over time.

1.4 Selenium-substituted MAPO (**8**)

For additional research into potential phosphorus substituents in **MAPO** molecules, elements with electronegativity similar to carbon, such as selenium, were selected. The reaction was performed according to the same research used for the attempted synthesis of **7**.[40]

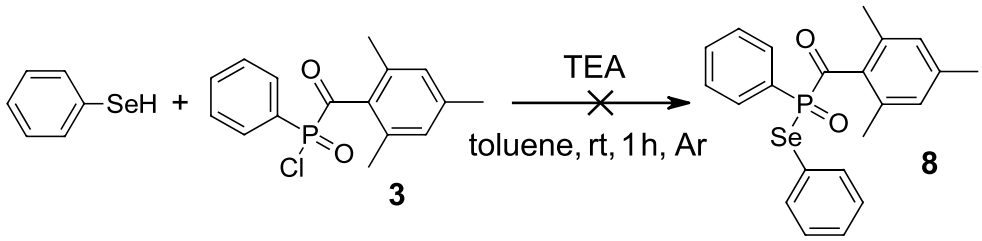

In the first step of the reaction, benzeneselenol (1 eq.) was deprotonated by TEA (2 eq.), and the nucleophilic substitution was performed on **3** (1 eq.). The reaction control was performed with ^{31}P-NMR (Figure S 26) and UPLC-MS (Figure 50). After 1 h of reaction time both analysis methods showed the completion of the reaction. However, both methods showed several byproducts as well. According to UPLC-MS, the desired product was formed.

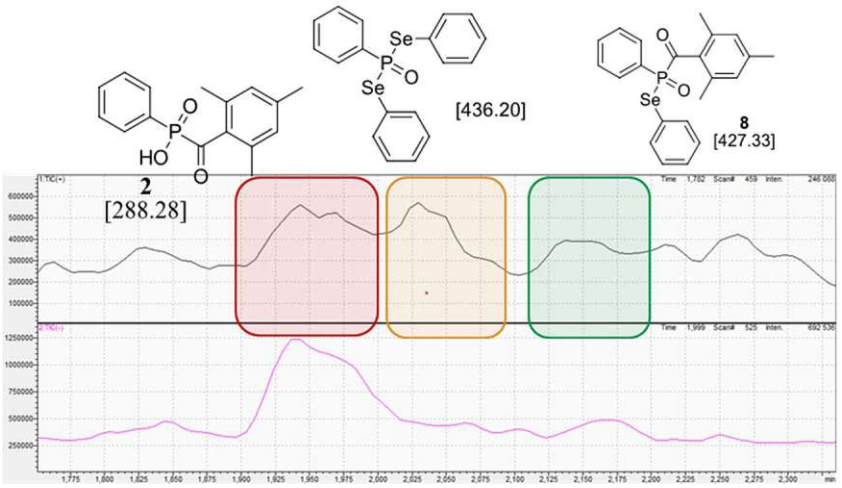

*Figure 50: UPLC-MS of the crude reaction mixture **8**.*

One of the byproducts was identified and confirmed[45] and is represented in Figure 51.

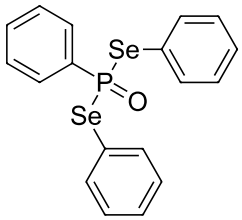

Figure 51: By-product of the reaction.

For the purification of **8** diluted aqueous acid solution was used to remove the base. The byproduct represented in Figure 51 was removed by this purification step, however the decomposition of **8** had started. In the next seven days, the product decomposed completely (Figure S 27). Since the product was placed under an inert atmosphere it can be concluded that this molecule analogous to **7** is unstable.

For the next synthesis, the focus of the research shifted to developing a new **MAPO** photoinitiator featuring a phosphorus-oxygen bond, like **TPO-L**. The goal was to enhance the steric hindrance by substituting the ethoxy group with the highly sterically demanding perfluoro-tert-butyl group.

1.5 Oxygen-substituted MAPO (**9**)

The first attempt to synthesize **9** was performed in analog to synthesis of **4**. The starting material precursor **3** was used and the synthesis was performed following the research described in Roszkowski et al.[34] According to ^{31}P-NMR (Figure S 28) and UPLC-MS (Figure S 29), the substitution did not take place and **3** was hydrolyzed to **2**. Therefore, it was concluded that this synthesis pathway cannot be applied in this case and new synthesis methods had to be researched.

Xiong et al. present a novel and effective method for the direct esterification of phosphinic and phosphoric acids. They report the crucial role of dicyclohexylcarbodiimide DCC as a coupling agent for successful esterification. Furthermore, they have reported excellent yields of 90 % and above. Particularly, their research indicates that the optimal conditions for achieving the highest yields involve using dioxane as a solvent and 1.1 eq. DCC. In this research, the reaction was performed according to these findings with few modifications.

The starting material for reaction **2** was synthesized following the general procedure of precursor synthesis. The reaction was performed under an inert atmosphere and at room temperature. In the first step of the reaction, a solution of **2** (1 eq.) was added to the suspension of DCC (1.1 eq.) in dioxane. This was followed by the dropwise addition of perfluoro-tert-butanol (1 eq.). The reaction was performed for 18 h.

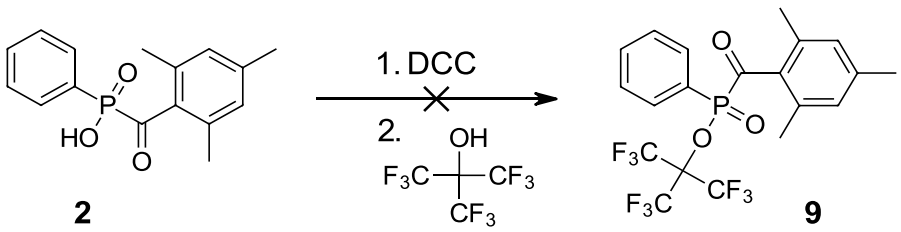

2 **9**

dioxane, rt, 18 h, Ar

The consumption of **2** was followed by ^{31}P-NMR. After 18 h of reaction ^{31}P-NMR (Figure S 30) and UPLC-MS (Figure S 31) were performed and showed that the consumption of starting material **2** did not occur.

The results of the conducted reaction once again highlighted the crucial role played by the steric hindrance of the reaction partners in the synthesis of the desired modifications.

1.6 Phosphorus-substituted MAPO (**10**)

The next modification attempt of the **MAPO** phosphonyl group involved the synthesis of a phosphorus-phosphorus bond. The motivation for this molecule was to investigate how phosphorus substituents impact performance and absorption, given that phosphorus possesses a lower electronegativity compared to oxygen or carbon, which are present in **TPO** and **TPO-L**. Two different attempts were conducted to synthesize the desired molecule.

1st attempt

A new study described by Suzuki et al.[47] reports the synthesis of organic magnesium phosphides useful for the synthesis of new organic phosphorus compounds. The literature[47] reports a successful synthesis of a complex presented in Figure 52 synthesized from di-tert-butyl-chlorophosphin with magnesium and lithium chloride.

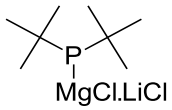

Figure 52: The proposed complex of di-tert-butyl chlorophosphin, magnesium, and lithium chloride

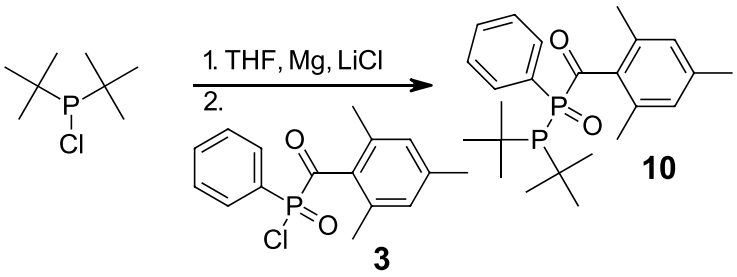

The first step of the reaction was to synthesize the complex presented in Figure 52. Magnesium shavings (1.7 eq.) and lithium chloride (1 eq.) were suspended in dry THF under an inert atmosphere and the suspension was activated with 1 drop of di-tert-butyl chlorophosphin. After the successful activation, the rest of the di-tert-butyl chlorophosphin (1 eq.) was added dropwise to an ice bath-cooled suspension. As reaction control, ^{31}P-NMR was performed. After 48 h of the reaction, ^{31}P-NMR (Figure S 32) analysis revealed the complexation of di-tert-butyl chlorophosphin, as the signal corresponding to this starting material was no longer detectable.

For the second step of the reaction, a solution of **3** (1 eq.) that was separately cooled down with an ice bath was added dropwise to the synthesized complex. The stirring of

the combined solutions continued for the next 2 h at 0 °C before the temperature was allowed to reach room temperature and the reaction control was performed. It was determined by ^{31}P-NMR (Figure S 33) that the mixture contained not only unreacted **3** but that the synthesized complex had decomposed since the signal corresponding to di-tert-butyl chlorophosphin was also detected.

2nd attempt

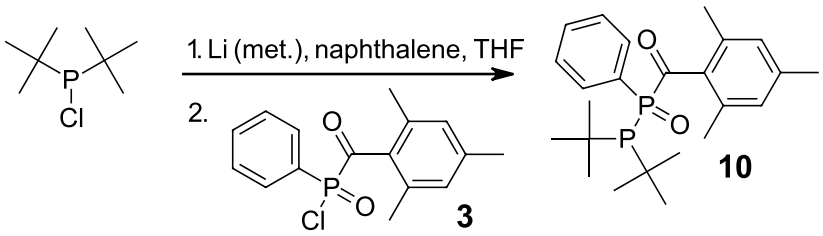

The second synthesis attempt of the desired molecule was performed with elementary lithium (4 eq.) and naphthalene (0.03 eq.) as catalysts.[48] After the successful activation, di-tert-butyl chlorophosphin (1 eq.) was added to the dark-colored suspension. For the next step of the reaction, lithium excess was separated and a solution of **3** (2.2 eq.) was added. The monitoring of the reaction was performed by ^{31}P-NMR (Figure S 34). However, after 18 h of reaction time, it was clear that both starting materials as well as several byproducts were present in the reaction mixture.

Both attempts to synthesize the intended modification did not lead to the desired outcome. The presence of di-tert-butyl groups, known for their high steric hindrance, appears once more as a potential explanation for the unsatisfactory outcomes.

Therefore, the next aim for modifications involved molecules with lower steric demands. Furthermore, investigation into the effects of electron-withdrawing groups on **MAPO** molecules should provide some interesting novel insights. For this purpose, pseudohalide were chosen and investigated as the new possible substituents.

1.7 Pseudohalide-substituted MAPO

1.7.1 Nitrile-substituted MAPO (**11**)

Multiple synthesis attempts were performed to synthesize **11**.

1st attempt

The research of Shi et al.[49] reports a new synthesis approach to perform pseudohalogenation of phosphorochloridates under milder conditions compared to conventional methods. Their goal thereby was to optimize the pseudohalogenation using sodium pseudohalides. They report improved reaction rates, higher yield, suppression of side reactions, and reactions that do not require anhydrous solvents.[49] To achieve these goals, they propose a phase transfer reaction. It was established that when quaternary ammonium salts were used as phase-transfer catalysts, a small amount of water was crucial to reach higher reaction rates.[49] On the other hand, the performed research with 18-crown-6 as a phase-transfer catalyst, showed with or without water successful reaction with higher rates.[49] In this research both methods were tested.

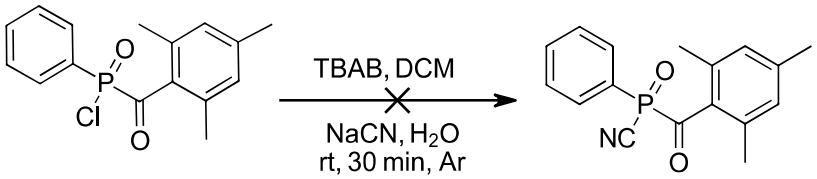

3 **11**

Following the literature[49] the first reaction was performed with tetrabutylammonium bromide (TBAB) as a phase-transfer catalyst. To a solution of **3** (1 eq.) and TBAB (0.1 eq.) in DCM, an aqueous solution of sodium cyanide (1.5 eq.) was added. The reaction was performed at room temperature and for 30 min. The monitoring of the reaction was performed with UPLC-MS (Figure S 35). Since **3** is known to hydrolyze back to **2** in the presence of water, it was not surprising that **2** was found after the reaction was completed.

As already mentioned, the research[49] has reported a successful phase-transfer reaction as well without the presence of water traces.

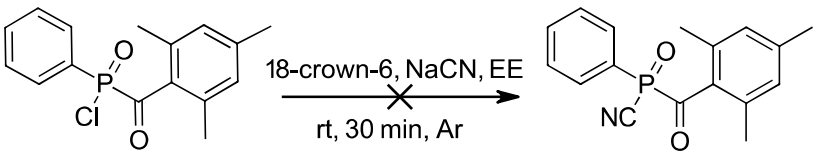

3 **11**

The reaction was performed under the same conditions as the first phase-transfer reaction: at room temperature and for 30 min. Instead of DCM/water, ethyl acetate was used as a solvent, and 18-crowns-6 (0.1 eq.) as a phase-transfer catalyst. The monitoring of the reaction was performed with ^{31}P-NMR (Figure S 37) and UPLC-MS (Figure S 36). After 30 min of reaction, it was determined by ^{31}P-NMR that besides **3** in the reaction mixture, **2** were present as well. The UPLC-MS measurement has confirmed the presence of **2**.

The pseudohalide derivatives are known to be less stable than the corresponding halide. To remove any water traces from the reaction mixture a couple of precautions were taken, including using dry solvents and drying the salt/catalyst *in vacuo.* Consequently, one plausible explanation for the presence of compound **2** in the reaction mixture is that the intended pseudohalide derivative was successfully synthesized, but it is inherently unstable, leading to rapid hydrolysis and the formation of **2**. Nonetheless, it is essential to note that this hypothesis could not be proven.

Since both methods of phase-transfer reactions were unsuccessful and resulted in either the hydrolysis product or no reaction, new approaches for synthesizing **MAPO** molecules containing phosphorus-nitrile bonds were investigated.

2nd attempt

Li et al. n.d. report a new synthetic approach to organophosphorus compounds containing acylthiourea derivatives. In this multi-step synthesis, the synthesis of isocyanate from phosphorochloridate was reported as successful and was then further used in the synthesis of the desired product. In the reported research potassium isocyanate was used.[50]

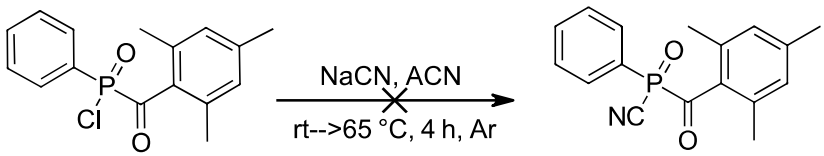

3 **11**

The procedure described in the literature[50] was modified. Instead of potassium isocyanate, sodium cyanide was used. The salt (1.1 eq.) was dissolved in acetonitrile and an acetonitrile solution of **3** (1 eq.) was added. The reaction was performed for 1 h at room temperature before the temperature was raised to 65 °C. During the reaction, a white precipitate was formed. The reaction control was performed with ^{1}H-NMR (Figure S 38). These measurements have shown that the precipitated product formed during the reaction was sodium 2,4,6-trimethylbenzoylphenylphosphinate (see Figure 53) and that the reaction was sadly unsuccessful.

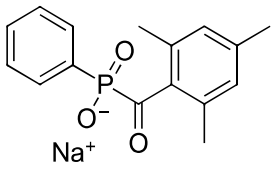

Figure 53: Sodium 2,4,6-trimethylbenzoylphenylphosphinate

The water content of used acetonitrile was measured by the Karl Fischer method and was determined to be 9.97 ppm. Furthermore, sodium cyanide was dried under a high vacuum for a couple of hours to get rid of any water traces. Nonetheless, it is clear that during the reaction hydrolysis took place and sodium 2,4,6-trimethylbenzoylphenyl phosphinate was formed. Once more, as a potential explanation, the reduced stability of the desired pseudohalide presents itself as a possible solution.

1.7.2 Thiocyanate-substituted MAPO (**12**)

The synthesis attempts used for **11** were also applied in the synthesis of **12**.

1st attempt

The first attempt to synthesize the thiocyanate substituted **MAPO** was performed as a phase-transfer reaction following the already-described research by Shi et al. The first attempted synthesis was performed with TBAB, and the results were the same as in the nitrile synthesis. The UPLC-MS (Figure S 35) has shown that **3** hydrolyzed in the presence of water to **2**.

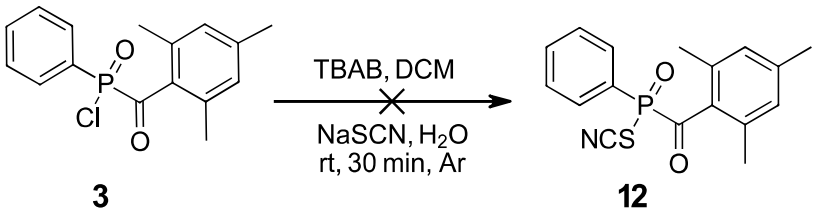

3 **12**

2nd attempt

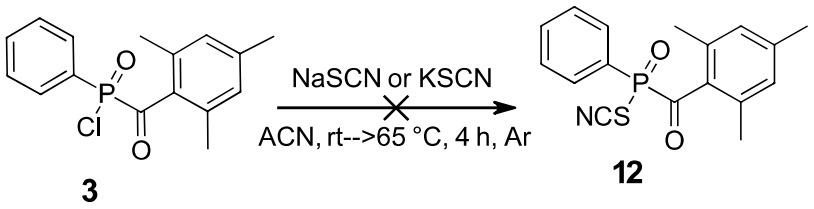

3 **12**

The second synthesis attempt was performed analogous to the 2nd attempted synthesis of **11**, following the synthesis described in Li et al. n.d. The white precipitate was formed during the reaction and after measuring ^{1}H-NMR it was determined that sodium 2,4,6-trimethylbenzoylphenylphosphinate (see Figure 53) was built.

The reaction was performed once again, but this time with potassium isocyanate. After the drying of the salt (2 eq.) under high vacuum, the salt was dissolved in acetonitrile and the acetonitrile solution of **3** (1 eq.) was added. The reaction mixture was stirred for 1 h before the temperature was raised to 65 °C. The reaction was monitored by ^{31}P-NMR. After 4 h (Figure S 39) of the reaction, **3** was still present in the reaction mixture. The reaction continued and the next measurement was performed after 8 h, and it was determined that the reaction did not occur. After 14 days the reaction mixture that was stored under an inert atmosphere was measured once again with ^{31}P-NMR (Figure S 40) and **2** was detected.

Several attempts were made to synthesize the desired pseudohalide derivatives of **MAPO**. However, considering the unsatisfactory results, it can be concluded that the synthetic approach using pseudohalide salts and **3** may not be effective. Alternatively, it is possible that the desired products were indeed synthesized at some point but are too unstable and rapidly undergo hydrolysis to yield **2** in the presence of even trace amounts of water.

2 Electrophilic Reactions

The major focus of this research were the nucleophilic reactions to synthesize new **MAPO** photoinitiators by a simple and efficient synthesis route. Therefore, the syntheses were performed by nucleophilic substitution on **3** that was produced by efficient general procedure. However, we have encountered a couple of difficulties using the general synthesis path. Firstly, the reaction of **3** with nucleophiles has usually resulted in an attack on the carbonyl group and therefore cleavage of the product. The removal of these byproducts was possible, but it has influenced the overall reaction yield and, in some synthesis, has led to the decomposition of the desired product. Furthermore, as previously proven, the nucleophilic attack on **3**, which already has a **MAPO** backbone, with sterically demanding nucleophiles was unsuccessful and yielded usually the hydrolyzation product **2**. Therefore, this method can be applied efficiently with less sterically demanding nucleophiles such as diethylamine.

Consequently, new synthesis routes for the synthesis of **MAPO** photoinitiators should be researched. At this stage of our research, we wanted to investigate electrophilic reactions. One of the established methods for the synthesis of new **BAPO** molecules involves the use of bisacyl phosphoenolate in reactions with various electrophiles. This method should be tested as a potential new approach for the synthesis of new **MAPO** molecules.

The reaction was performed as a multi-step reaction. The first step of the reaction is a selective monoacylation that should be possible since the first acylation step results in the lowering of the nucleophilicity of phosphorus. The synthesized monoacyl phosphoenolat is afterward reacted with an electrophile to the corresponding monoacyl phosphine. The last step of the reaction is the oxidation of phosphine to monoacyl phosphine oxide. In this research, cyclohexyl isocyanate was selected as the electrophile due to its potential to introduce steric effects into the molecule. The addition of this molecule allows for the incorporation of a second carbonyl group which can induce the bathochromic shift, like the observed redshift in **BAPO** molecules. The proposed synthetic pathway is represented in Figure 54.

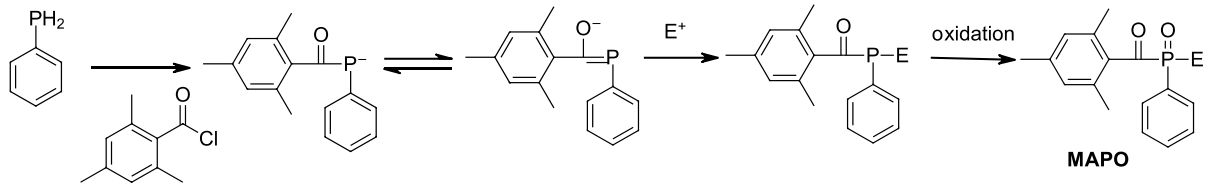

*Figure 54: Synthetic pathway for the synthesis of new **MAPO** structures.*

The synthesis followed the research conducted by Müller[51] which was primarily focused on the synthesis and application of novel phosphorus-based photoinitiators. As already mentioned, the first step of the synthesis was the selective monoacylation of phenyl phosphine.

2.1 Synthesis of **13**

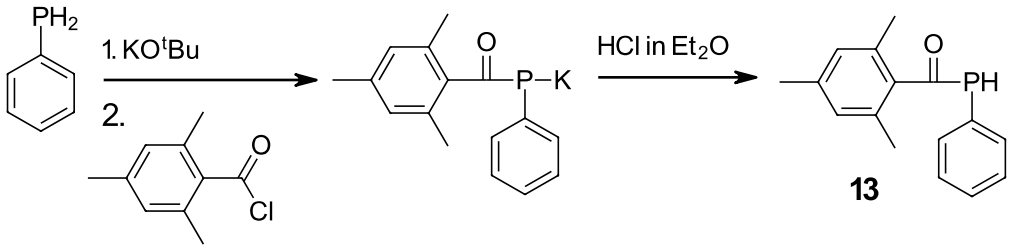

For this purpose, potassium tert-butoxide was used to deprotonate phenyl phosphine. After deprotonation, an equimolar amount of mesityl chloride was added and the reaction was stirred at room temperature for the next 2 h. The monitoring of the reaction was performed by ^{31}P-NMR (Figure S 41) and after 2 h of reaction time, it was confirmed that the reaction was complete. For the purification of the product, the reaction mixture was warmed to 60 °C and filtered over celite. The potassium salt of the desired product was cooled to room temperature and treated with a solution of HCl in diethyl ether. The precipitated salt was filtered off and the solvent was removed under a vacuum. Product **13** was obtained as a pale-yellow solid, characterized by ^{31}P-NMR (Figure S 42) and the reaction yield was 74 % of the theory.

Following the procedure described in the same research[51] to synthesize N-cyclohexyl formamide functionalized bis-acylphosphine, the synthesis of **14** was performed.

2.2 Synthesis of **14**

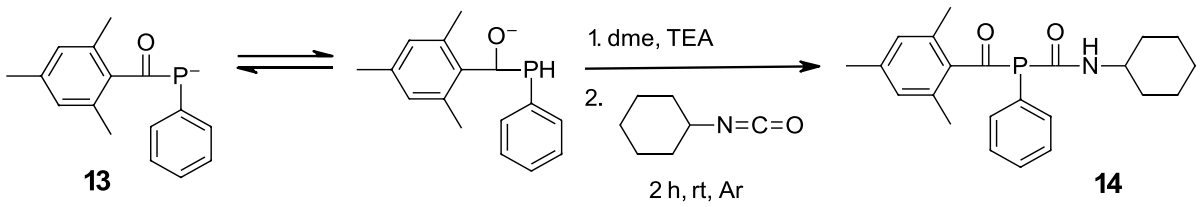

The reaction was once again performed under total air and moisture exclusion. In the first step of the reaction, phosphoenolate **13** was reacted with cyclohexyl isocyanate. The reaction solvent was dme, the reaction was performed at room temperature and with a catalytic amount of triethylamine (0.05 eq.). The reaction progress was monitored with ^{31}P-NMR. Before the final reaction step, intermediate **14** was treated with 0.05 eq. of HCl in diethyl ether (2 M) to precipitate triethyl amine. According to performed ^{31}P-NMR (Figure S 43) several phosphorus-containing byproducts were formed during the reaction. However, according to performed ^{1}H-NMR (Figure S 44) measurement, it was not possible to fully conclude the presence of the desired product. Nonetheless, the next synthesis step was performed directly afterward since the phosphines are known to be unstable. To obtain the desired **MAPO** structure **15**, the oxidation of the intermediate **14** had to be performed.

2.3 Synthesis of **15**

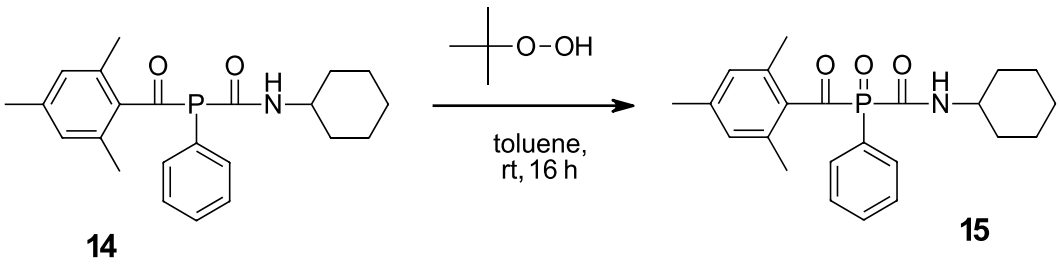

The oxidation was carried out under light exclusion with 5.5 M tert-butyl hydroperoxide in decane. The reaction ended after 12 h of stirring at room temperature. The monitoring of the reaction was performed by ^{31}P-NMR. Sadly, during the oxidation new byproducts of the reaction were formed. The comparison of the ^{31}P-NMR measurements for the intermediate **14** and final product **15** is represented in Figure 55.

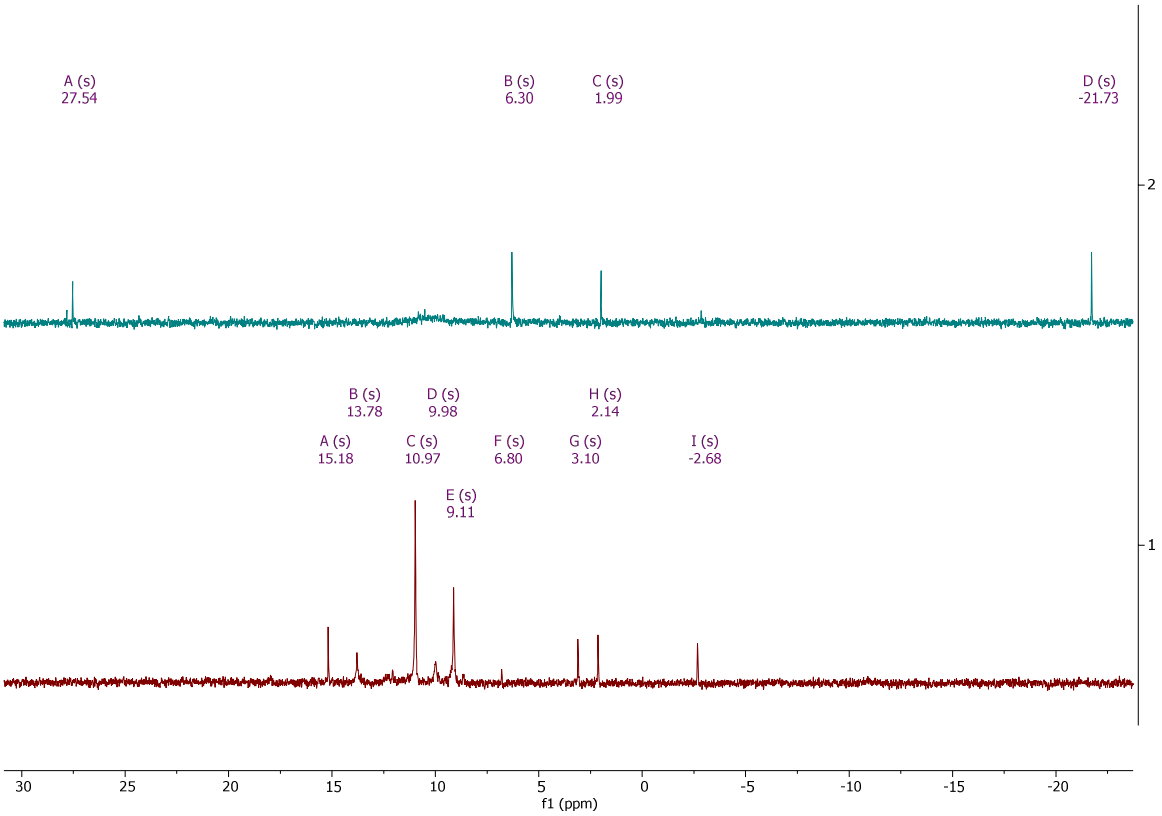

*Figure 55: Comparison of ^{31}P-NMR before the oxidation (**14**, green spectra) and after (**15**, red spectra)*

In the ^{31}P-NMR spectra of the intermediate **14** a signal with a low chemical shift, characteristic of phosphine, can be observed along with several byproducts exhibiting higher chemical shifts. Following the oxidation, the signal with the lower chemical shift is no longer observed, but several new products were formed.

Besides ^{31}P-NMR (Figure S 45), ^{1}H (Figure S 47) and ^{13}C-NMR (Figure S 48) were measured as well. Since the number of byproducts was too high to significantly validate the existence of the desired product **15** in the reaction mixture using these analysis methods, the purification and separation of the byproducts had to be performed. But firstly, UPLC-MS (Figure S 46) measurement was performed and the m/z value corresponding to product **15** was identified. Furthermore, the UPLC-MS showed the existence of a couple of byproducts, one of which was identified as product **2**.

Further investigation of the reaction mixture was performed by TLC. The most efficient separation on TLC was achieved in chloroform with gradient elution of methanol from 5 % to 50 %. Since the UPLC-MS showed that **2** was present in the reaction mixture, a TLC analysis of **2** was also performed. The product **2** showed no mobility in chloroform and could be eluted only with higher amounts of methanol in chloroform.

After performing a 2D TLC analysis in chloroform it was confirmed that all the products in the reaction mixture are stable on silica and therefore an MPLC column chromatography was performed. For the purification, 500 mg of crude product was used and the MPLC was performed with pure chloroform. The collected fractions had a volume of 30 mL and from each collected fraction TLC was performed and examined under UV light. After the fractions eluted with pure chloroform were collected, the amount of methanol was increased to 5 % and finally to 50 %.

The collected fractions were analyzed by ^{31}P-NMR and TLC. To determine the fraction possibly containing the desired product, from each collected fraction TLC was performed and examined under UV light. All the fractions that showed positive results in TLC measurements were analyzed further using ^{31}P-NMR. Using these analysis methods, the fraction that had fulfilled the mentioned requirements for the product **15**-showed signals in both TLC and ^{31}P-NMR was identified (from now on referred to as "collected fraction") and evaporated to dryness. In Figure 56 represented is the comparison of the ^{31}P-NMR measurements of the crude product **15** and collected fraction.

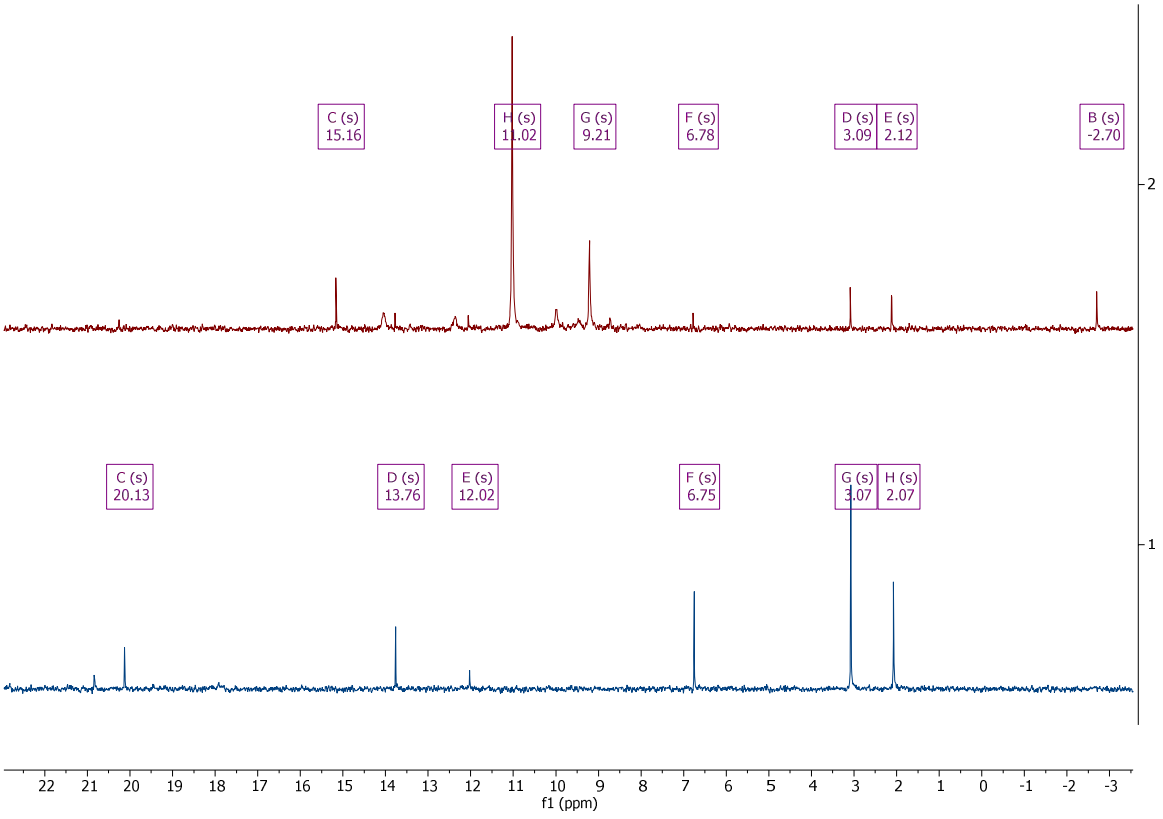

*Figure 56: Comparison of ^{31}P-NMR for the crude product (**15**, red spectra) and a collected fraction (blue spectra)*

As in Figure 56 apparent, with the performed MPLC column chromatography some degree of purification was achieved. Nonetheless, the collected fraction still contains several phosphorus-containing byproducts.

As there is no existing literature data available for the desired molecule, it is not possible to positively identify the desired product **15** solely based on ^{31}P-NMR. Moreover, given that the collected fraction contains multiple phosphorus-containing products, no additional purification could be performed.

To further analyze the collected fraction, ^{1}H-NMR (Figure S 50) was performed. Based on these measurements, the presence of the desired product **15** cannot be excluded. Therefore, the study of the absorption capabilities and performance of the crude product and collected fraction were investigated.

2.3.1 UV-Spectroscopy

Firstly, UV-Vis measurements of the crude product and collected fraction were performed. As reference molecules, **TPO** and **TPO-L** were used. Since the UPLC-MS has identified acid **2** as one of the byproducts of the reaction, the UV-Vis measurement of this molecule was performed as well. For the measurements 0.001 M solutions of corresponding photoinitiators in acetonitrile were prepared. The results of the measurement are represented in Figure 57.

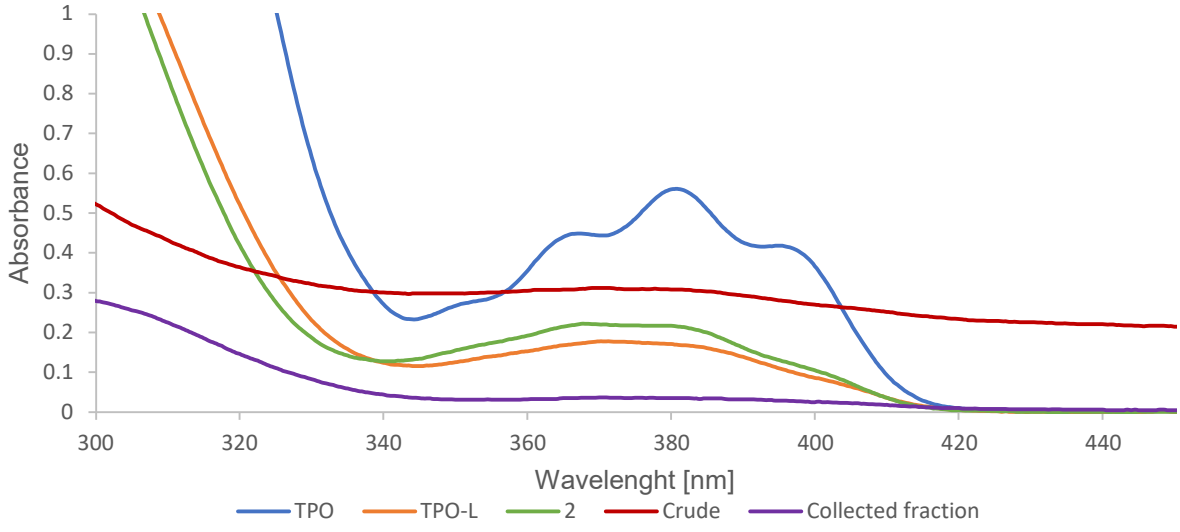

*Figure 57: UV-Vis spectra of 0.001 M solutions of **TPO** (blue), **TPO-L** (orange), **2** (green), crude product (red), and collected fraction (purple) in acetonitrile.*

The measurement results reveal a significantly higher absorption in the crude product compared to the collected fraction. Additionally, the collected fraction shows a very low overall absorption. The UV-Vis spectra presented also indicate that neither the crude product nor the collected fraction shows the typical absorption band of **MAPO** molecules.

2.3.2 Photo-DSC measurements

After evaluating the absorption compatibilities of the crude product and collected fraction, a photo-DSC study was conducted. The photo-DSC measurements were performed with broad-band irradiation (320-500 nm). The samples were prepared with UDMA and 1 mol% of the photoinitiator. As reference photoinitiators **TPO** and **TPO-L** were used. The samples were irradiated for 300 s, with the intensity of 60 $mWcm^{-2,}$ and under nitrogen atmosphere (20 $mLmin^{-1}$).

The results of the measurements are represented in Figure 58.

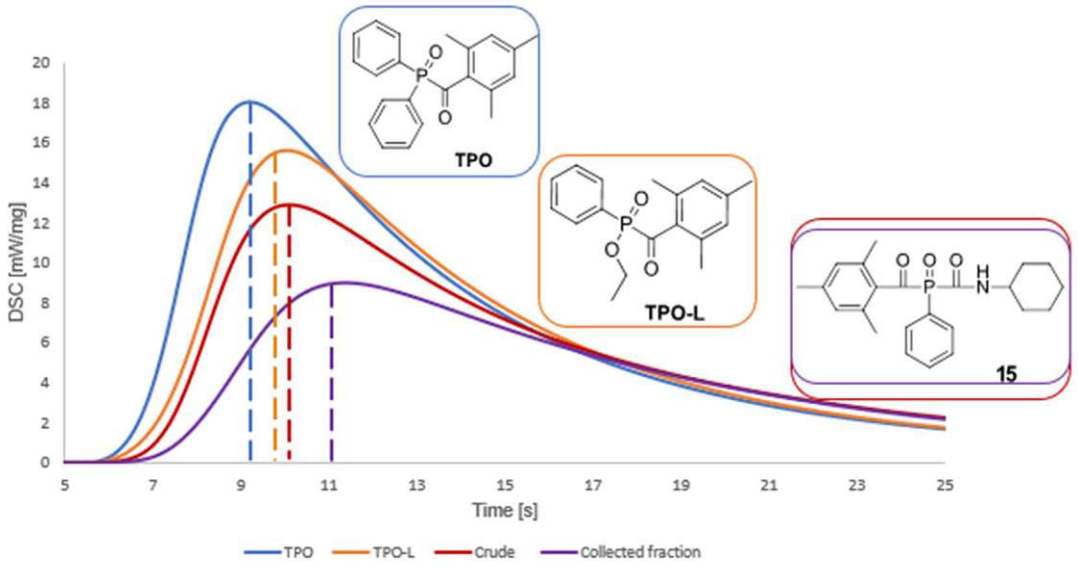

*Figure 58: Photo-DSC analysis of formulations consisting of 1 mol% **TPO** (blue), **TPO-L** (orange), crude product (red), and collected fraction (purple) in UDMA at room temperature using broadband irradiation.*

According to the results of the conducted photo-DSC study, **TPO** and **TPO-L** show the best performance. The crude fraction shows overall better performance than the collected fraction. Further collected data from the measurement is represented in Table 8.

*Table 8: Photo-DSC analysis of formulations consisting of 1 mol% **TPO**, **TPO-L**, the crude product, and collected fraction in UDMA at room temperature using broadband irradiation.*

Sample	t_{max} [s]	Height [mW/mg]	$t_{95\%}$ [s]	Area [J/g]	DBC [%]	R_p [mmol $s^{-1}L^{-1}$]
TPO	9.27 ± 0.2	17.8 ± 0.4	39.0 ± 1.6	154 ± 0	64.2 ± 0.1	176 ± 3
TPO-L	10.1 ± 0.3	14.9 ± 0.5	37.4 ± 1.5	141 ± 1	58.9 ± 0.5	148 ± 5
Crude	10.5 ± 0.5	12.9 ± 0.3	38.3 ± 3.3	138 ± 0	57.5 ± 0.2	128 ± 3
Collected Fraction	11.4 ± 0.2	9.23 ± 0.53	35.9 ± 1.5	108 ± 8	45.2 ± 3.2	91 ± 5

Based on the collected data it can be determined that the crude product exhibits an overall better performance than the collected fraction. However, this outcome was expected when comparing the UV-Vis measurement results of these two photoinitiators.

The collected fraction requires the most time to reach the peak maximum and exhibits the lowest peak area and height. The calculated results for the DBC and Rp are graphically represented in Figure 59 and Figure 60.

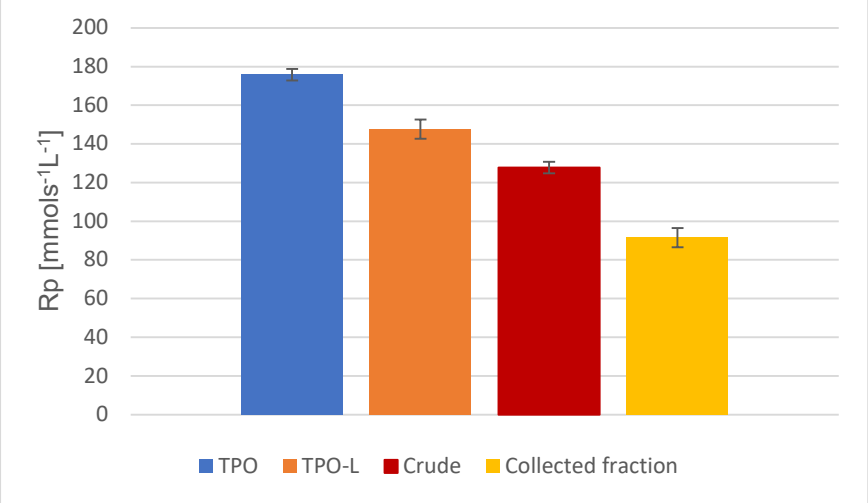

*Figure 59: Comparison of Rp values for **TPO**, **TPO-L**, crude, and collected fractions obtained from broadband photo-DSC measurements.*

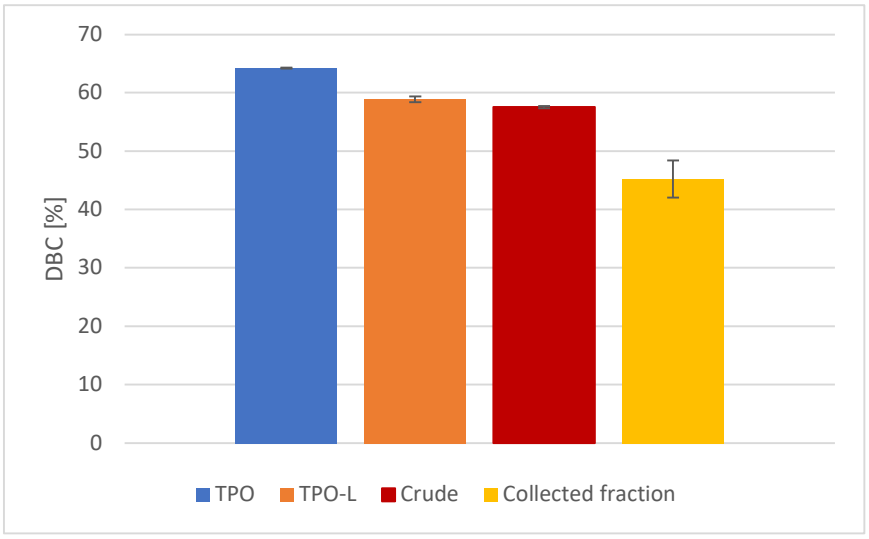

*Figure 60: Comparison of DBC values for **TPO**, **TPO-L**, crude, and collected fractions obtained from broad-band photo-DSC measurements.*

The crude product shows a higher efficiency based on the calculated DBC and a much higher rate of polymerization compared to the collected fraction.

However, when comparing the performance of the crude product and **TPO-L** some similarities can be observed. Besides the time needed to reach the peak maximum, according to the calculated DBC, both molecules show a very similar efficiency in monomer conversion. However, in terms of the polymerization rate, **TPO-L** significantly outperforms the crude product.

In summary, it remains challenging to definitively rule out the presence of the desired product in either the crude or collected fraction, given the analysis conducted. Nonetheless, the synthesized product, as indicated by performance and absorption measurements, exhibits overall lower performance when compared to state-of-the-art **MAPO** photoinitiators.

EXPERIMENTAL PART

1 Nucleophilic Reactions

1.1 General procedure for precursor synthesis (3)

1.1.1 Synthesis of lithium 2,4,6-trimethyl benzoyl phenyl-phosphinate (1)[52]

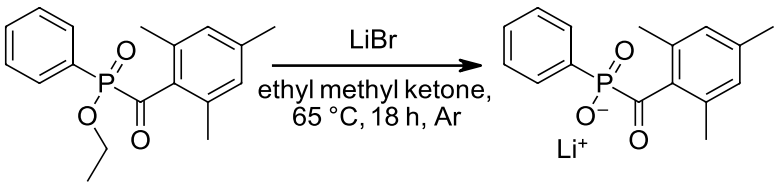

TPO-L
[316.33]

1
[294.24]

Materials:

60 g	(190 mmol)	**TPO-L**
66 g	(759 mmol)	lithium bromide
850 mL		ethyl methyl ketone

Preparation:

The synthesis of **1** was performed according to literature.[52]In a three-necked round bottom flask equipped with a reflux condenser and set under an argon atmosphere **TPO-L** (60 g, 190 mmol, 1 eq.) was dissolved in 850 mL ethyl methyl ketone and LiBr (66 g, 759 mmol, 4 eq.) was added. The clear solution was stirred at room temperature for 15 min before the temperature was raised to 65 °C. The mixture was stirred for 18 h at this temperature during which a yellow precipitate was built. The precipitate was filtered off and washed one time with 50 mL ethyl methyl ketone, two times with 50 mL petroleum ether, and dried under vacuum. The product was finally recrystallized from diethyl ether and yielded 46 g (82 % of the theory) of a white powder.

Yield: 46 g (82 % of the theory), white powder

$C_{16}H_{16}LiO_3P$

^{1}H NMR (200 MHz, DMSO) δ 7.75 – 7.56 (m, 2H), 7.37 – 7.25 (m, 3H), 6.73 (s, 2H), 2.18 (d, *J* = 9.6 Hz, 9H) ppm.

^{31}P NMR (101 MHz, DMSO) δ 9.31 ppm.

1.1.2 Synthesis of 2,4,6-trimethylbenzoylphenylphosphinic acid (2)[40]

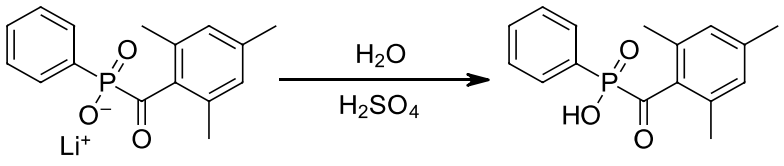

1 [294.24] **2** [288.28]

Materials: 1 g (3 mmol) **1**

Preparation:

The synthesis of **2** was performed in analogy to literature.[40] A solution of **1** (1 g, 3 mmol, 1 eq) in 60 mL deionized water was stirred at room temperature. To this solution, 0.5 M H_2SO_4 (12 mL) was added to reach pH 1. During the addition of acid, the precipitation of the product was observed. To the resulting suspension, 150 mL ethyl acetate was added, and after vigorous stirring of the two phases they were separated using a separatory funnel. The aqueous layer was washed two times with 50 mL ethyl acetate and the combined organic phases were washed twice with 50 mL deionized water. After drying the organic phase with anhydrous N_2SO_4 and removing the drying agent, the solvent was removed under reduced pressure and the product dried *in vacuo*. The desired product was obtained as a pale-yellow solid (967 mg, 99 % of the theory).

Yield: 967 mg (99 % of the theory), pale-yellow solid

$C_{16}H_{17}O_3P$

^{1}H NMR (200 MHz, $CDCl_3$) δ 12.06 (s, 1H), 7.78 – 7.59 (m, 2H), 7.49 (t, *J* = 7.4 Hz, 1H), 7.40 – 7.23 (m, 2H), 6.67 (s, 2H), 2.20 (s, 3H), 1.95 (d, *J* = 7.9 Hz, 6H) ppm.

^{31}P NMR (101 MHz, $CDCl_3$) δ 16.35 ppm.

UPLC-MS [2M] 577

1.1.3 Synthesis of 2,4,6-trimethylbenzoylphenylphosphinic acid chloride (3)

1st approach[40]

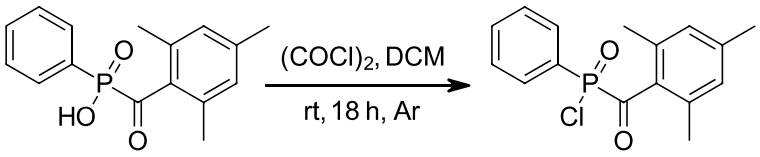

2 [288.28] **3** [306.72]

Materials:	970 mg	(3 mmol)	**2**
	881 mg	(7 mmol)	oxalyl chloride
	8 mL		dry dichloromethane

Preparation:

The synthesis of **3** was performed according to literature.[40] A three-necked round bottom flask set under argon atmosphere by Schlenk technique **2** (970 mg, 3 mmol, 1 eq.) was suspended in anhydrous dichloromethane (8 mL) and oxalyl chloride (881 mg, 7 mmol, 0.6 mL, 2 eq.) was added dropwise using a syringe. The evolution of gas bubbles was observed. The reaction mixture was stirred for 18 h at room temperature, during which it became a clear solution. The solvent was evaporated under reduced pressure and the residual oil was dissolved in anhydrous toluene (10 mL). The solvent was once again evaporated to dryness under reduced pressure to give a pale brown oil (960 mg, 93 % of the theory). Further purification of the product was not performed.

Yield: 960 mg (93 % of the theory) pale brown oil

$C_{16}H_{16}ClO_2P$

^{1}H NMR (200 MHz, CDCl3) δ 8.04 – 7.89 (m, 2H), 7.72 – 7.48 (m, 3H), 6.87 (s, 2H), 2.29 (s, 3H), 2.17 (s, 6H).

^{31}P NMR (101 MHz, $CDCl_3$) δ 28.05, 12.41* ppm.

*Correspond to the signal of the impurity

2nd approach[39]

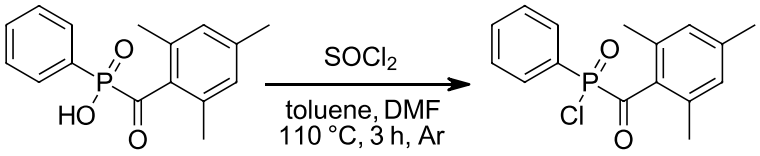

2 [288.28] **3** [306.72]

Materials:	5 g	(17 mmol)	**2**
	41 g	(347 mmol)	thionyl chloride
	50 mL		dry toluene
	5 µL		DMF

Preparation:

The second synthesis of acid chloride **3** was performed in analogy to modified literature.[39] In a three-necked round bottom flask set under an argon atmosphere, **2** (5 g, 17 mmol, 1 eq) was dissolved in 50 mL dry toluene. To the reaction solution, 5 µL DMF and thionyl chloride (41 g, 347 mmol, 20 eq) were added. The mixture was heated to 110 °C and the conversion of starting material was monitored by ^{31}P-NMR. The complete conversion of **2** was achieved after 3 h. The solvent and excess of thionyl chloride were removed under reduced pressure. The brown oil (3.77 g, 71 % of the theory) was used directly for the next synthesis step without further purification.

Yield: 3.77 g (71 % of the theory), brown oil

$C_{16}H_{16}ClO_2P$

^{1}H NMR (200 MHz, CDCl3) δ 8.05 – 7.89 (m, 2H), 7.79 – 7.46 (m, 3H), 6.87 (s, 2H), 2.33 (d, J = 15.4 Hz, 6H), 2.17 (s, 3H).

^{31}P NMR (162 MHz, $CDCl_3$) δ 75.54**, 35.96**, 28.17 ppm.

**Correspond to signals of the impurities

1.2 Synthesis of *N,N*-diethyl-P-phenyl-P-(2,4,6-trimethylbenzoyl) phosphonic acid (4)[40]

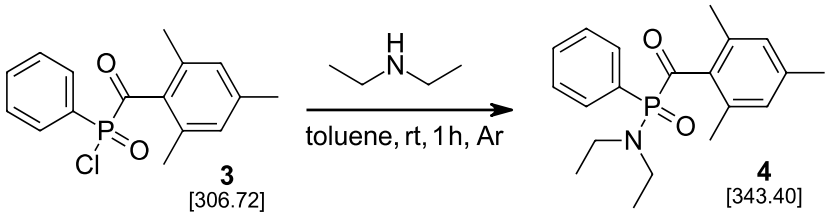

Materials:	944 mg	(13 mmol)	diethyl amine (DEA)
	1.7 g	(5 mmol)	**3**
	21 mL		dry toluene

Preparation:

The synthesis of **4** was performed according to modified literature.[40] In a three-necked round bottom flask set under an argon atmosphere using a Schlenk technique diethyl amine (DEA, 944 mg, 13 mmol, 2.4 eq.) was dissolved in 15 mL dry toluene. In a separate glass vial set under an argon atmosphere, **3** (1.7 g, 5 mmol, 1 eq.) was dissolved in 6 mL dry toluene. The DEA solution was added dropwise to the stirring solution of **3** at room temperature. The stirring of the reaction mixture continued for 1 h at room temperature. The reaction progress was followed by UPLC-MS and ^{31}P-NMR.

After the complete conversion of starting materials, the excess DEA and the reaction solvent were removed under reduced pressure. The crude product was once more dissolved in dry toluene (20 mL) and washed with deionized water (10 mL), 1 % (w/w) aqueous citric acid solution (3 x 10 mL), 2 % aqueous Na_2CO_3 solution (2 x 10 mL) and then once more with deionized water (15 mL). The product was dried over anhydrous Na_2SO_4, the drying agent was filtered off and the solvent was evaporated under reduced pressure. The product was recrystallized with petroleum ether to yield a yellow solid. (1.2 g, 65 % of the theory)

Yield: 1.2 g (65 % of the theory) yellow solid

$C_{20}H_{26}NO_2P$

Mp: 81.2-82.4 °C

^{1}H NMR (200 MHz, $CDCl_3$) δ 7.86 (ddd, *J* = 11.3, 8.1, 1.6 Hz, 2H), 7.63 – 7.35 (m, 3H), 6.77 (s, 2H), 3.14 (dq, *J* = 10.4, 7.1 Hz, 4H), 2.24 (s, 3H), 2.11 (s, 6H), 1.12 (t, *J* = 7.1 Hz, 6H) ppm.

^{31}P NMR (101 MHz, $CDCl_3$) δ 18.09 ppm.

^{13}C NMR (101 MHz, $CDCl_3$) δ 137.98, 134.95, 132.94, 132.85, 132.49, 128.98, 128.66, 128.54, 39.59, 21.25, 19.81, 14.30, 14.27 ppm.

UPLC-MS: [M+1] 344.10

1.3 Synthesis of Phenyl-(2,4,6-trimethylbenzoyl)-thiophosphinic-phenyl ester (7)[40]

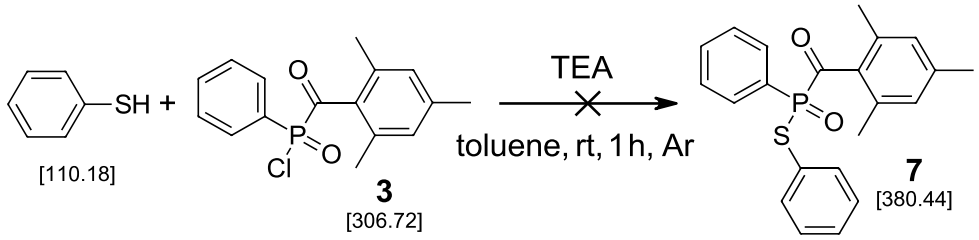

Materials:	180 mg	(1.63 mmol)	thiophenol
	330 mg	(3.26 mmol)	TEA
	500 mg	(1.63 mmol)	**3**
	5 mL		dry toluene

Preparation:

The synthesis of **7** was performed according to the modified literature.[40] In a glass reaction vial set under an argon atmosphere thiophenol (180 mg, 1.63 mmol,2 eq.) was dissolved in dry toluene (3 mL) and triethylamine (330 mg, 3.26 mmol, 2 eq.) was added dropwise. In a second glass vial set as well under argon atmosphere, a solution of **3** (500 mg, 1.63 mmol, 1 eq.) in dry toluene (2 mL) was stirred at room temperature. The thiophenol solution was added dropwise using a syringe to the second glass vial containing **3** and the reaction mixture was stirred for 1 h. The consumption of starting material was monitored by ^{31}P-NMR. After the complete consumption of starting material solvent was evaporated to dryness. The crude product was dissolved in 10 mL of deionized water and extracted with 3 x 5 mL dichloromethane. The product was once more evaporated to dryness and characterized by ^{31}P-NMR and UPLC-MS.

$C_{22}H_{21}O_2PS$

^{31}P NMR (**crude,** 101 MHz, $CDCl_3$) δ 89.74, 49.55, 33.58, 12.74* ppm.

UPLC-MS (**crude)**: [M+1] 342.95; [2M] 577 (TPO-OH); [M+1] 381;

^{31}P NMR (**worked-up,** 101 MHz, $CDCl_3$) δ 89.75, 12.43* ppm.

1.4 Synthesis of Phenyl-(2,4,6-trimethylbenzoyl)-seleno phosphinic-phenyl ester (8) [40]

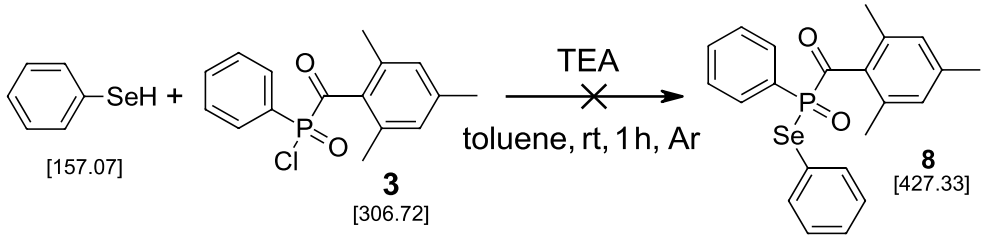

Materials:	500 mg	(1.63 mmol)	**3**
	256 mg	(1.63 mmol)	benzeneselenol
	330 mg	(3.26 mmol)	TEA
	5 mL		dry toluene

Preparation:

The synthesis of **8** was performed according to adapted literature.[40] In a glass vial set under an argon atmosphere, a solution of **3** (500 mg, 1.63 mmol, 1 eq.) in dry toluene (2 mL) was stirred at room temperature. In a three-necked round bottom flask set under an argon atmosphere using the Schlenk technique benzeneselenol (256 mg, 1.63 mmol, 1 eq.) was dissolved in dry toluene (3 mL) and TEA (330 mg, 3.26 mmol, 2 eq., 0.45 mL) was added dropwise. During the addition, a gas evolution was observed. After 15 min of stirring the reaction mixture at room temperature a solution of **3** in dry toluene was added dropwise using a syringe. The reaction progress was monitored by ^{31}P-NMR and UPLC-MS.

^{31}P NMR (**crude,** 101 MHz, $CDCl_3$) δ 34.69, 33.90, 23.35, 12.76*, 7.86 (d) ppm.

UPLC-MS (**crude**): [2M] 577 [M] 427.05

The work up of the reaction was performed according to the literature[40]. The solvent was evaporated to dryness and the crude product was dissolved in dry toluene (5 mL). The crude product was washed with deionized water (3 mL), 1 % (w/w) aqueous citric acid solution (3 x 2 mL), 2 % aqueous Na_2CO_3 solution (2 x 2 mL), and then once more with deionized water (3 mL). The product was dried over anhydrous Na_2SO_4, the drying agent was filtered off and the solvent was evaporated under reduced pressure. The ^{31}P-NMR was performed once more.

$C_{22}H_{21}O_2PSe$

^{31}P NMR (**worked-up,** 101 MHz, $CDCl_3$) δ 23.61, 15.52, 12.58** ppm.

After a week UPLC-MS and ^{31}P-NMR did not show any significant peaks.

2 Electrophilic Reactions

2.1 Synthesis of 13

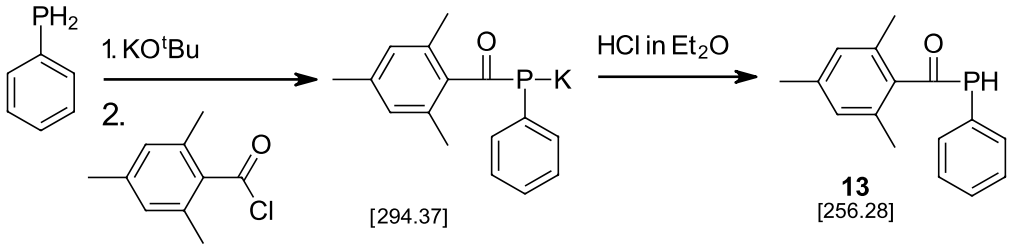

Materials:	500 mg	(4.54 mmol)	phenyl phosphine
	1 g	(9.08 mmol)	potassium-tert-butoxide
	830 mg	(4.54 mmol)	mesityl chloride
	35 mL		dry toluene

Preparation:

The synthesis was performed under total moisture and air exclusion. In a 50 mL Schlenk flask, a suspension of potassium-tert-butoxide (1 g, 9.08 mmol, 2 eq.) in dry toluene (15 mL) was prepared. To this suspension, phenyl phosphine (500 mg, 4.54 mmol, 1 eq.) was added at room temperature. During the addition, a color change was observed. To the stirring yellow solution, mesityl chloride (830 mg, 4.54 mmol, 1 eq.) diluted in toluene (20 mL) was added dropwise at room temperature. The stirring of the reaction mixture continued for the next 2 hours before the first reaction control with ^{31}P-NMR was performed. It was determined that the starting material-phenyl phosphine was fully consumed.

For the work-up, the yellow suspension was warmed to 60 °C and filtered over celite. The work-up of the reaction was performed as well under an inert atmosphere. The yellow filtrate consisting of sodium intermediate product was allowed to cool to room temperature and another ^{31}P-NMR measurement was performed. Finally, the solution was treated with a solution of HCl in diethyl ether (1 M) and the precipitated sodium chloride was removed by filtration. The solvent of the collected yellow filtrate was

removed *in vacuo* and product **13** was obtained as a pale-yellow solid with good yield (74 % of the theory) and was used directly for the next synthesis step.

Yield: 860 mg (74 % of the theory)

$C_{16}H_{17}OP$

^{31}P NMR (101 MHz, $CDCl_3$, potassium intermediate) δ 60.35, 27.97, 27.68 ppm.

^{31}P NMR (101 MHz, $CDCl_3$, **13**) δ -16.87 ppm.

2.2 Synthesis of 14

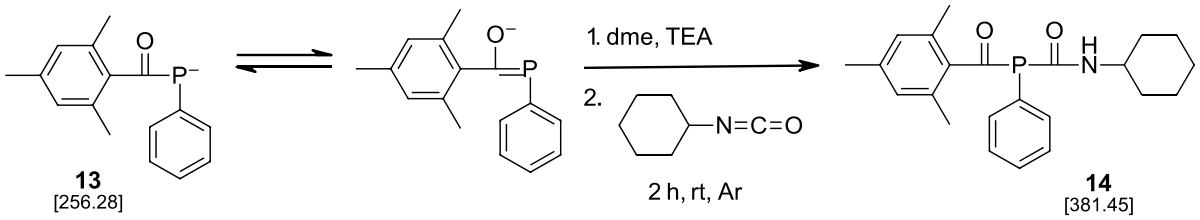

13 [256.28] **14** [381.45]

Materials:			
	860 mg	(3.36 mmol)	**13**
	17 mg	(0.17 mmol)	triethyl amine
	420 mg	(3.36 mmol)	cyclohexyl isocyanate
	15 mL		dme

Preparation:

In a 50 mL Schlenk flask set under an argon atmosphere, a solution of **13** (860 mg, 3.36 mmol, 1 eq.) in dme (15 mL) was placed. To the prepared solution, TEA (17 mg, 0.17 mmol, 0.05 eq.) was added followed by the dropwise addition of cyclohexyl isocyanate (420 mg, 3.36 mmol, 1 eq.). The reaction mixture was stirred at room temperature for 2 h and the reaction control was performed with ^{31}P-NMR. To the reaction mixture, a solution of HCl in diethyl ether (0.05 eq, 2 M) was added and the solvent was removed under reduced pressure. The obtained solid residue was dissolved in toluene and the precipitated amino hydrochloride was removed by filtration. The intermediate was obtained as a clear dark red liquid and was used directly for the next synthesis step.

$C_{23}H_{28}NO_2P$

^{31}P NMR (101 MHz, $CDCl_3$) δ 27.82, 27.54, 6.30, 1.99, -21.73 ppm.

2.3 Synthesis of 15

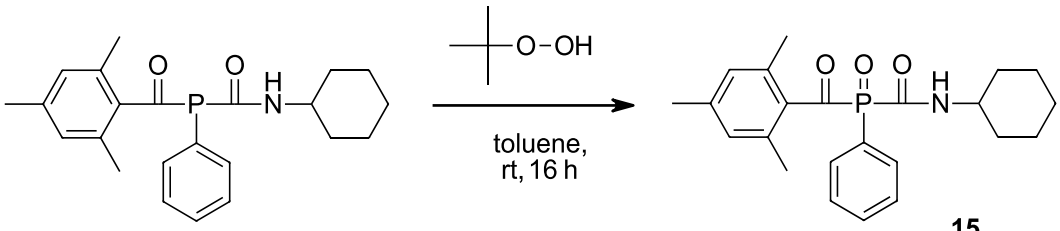

14
[381.45]

15
[397.45]

Materials: 1.2 g (3.15 mmol) **14**

424 mg (3.78 mmol) 5.5 M tert.-butyl hydroperoxide

Preparation:

The clear dark red solution of intermediate **14** (1.2 g, 3.15 mmol, 1 eq.) in toluene was placed in a 50 mL Schlenk flask. Under light exclusion, 5.5 M solution of tert.-butyl hydroperoxide in decane (1.2 eq.) was added dropwise and the reaction mixture was stirred at room temperature for 12 h. The reaction control of the now yellow solution was performed with ^{31}P-NMR and the solvent was removed *in vacuo* to yield a pale-yellow solid.

Yield: 104 %

$C_{23}H_{28}NO_3P$

^{31}P NMR (101 MHz, $CDCl_3$, **crude product**) δ 15.18, 13.78, 10.97, 9.98, 9.11, 6.80, 3.10, 2.14, -2.68 ppm

^{31}P NMR (162 MHz, $CDCl_3$, **collected fraction**) δ 15.16, 11.02, 9.21, 6.78, 3.09, 2.12, -2.70.

UPLC-MS: [M+1] 398.10

MATERIALS, EQUIPMENT, AND ANALYSIS

Chemicals and solvents:

All commercially available chemicals were used as received unless noted otherwise. Solvents and reagents were purchased at least in 96 % purity and purified according to common organic procedures if noted in the experimental section. Commercial grade methylene chloride (CH_2Cl_2), toluene and tetrahydrofuran (THF, Donau Chemie), were all obtained from Donau Chemie and dried with a PureSolvsystem (Inert, Amesbury, MA). The photoinitiators TPO and TPO-L were provided by Ivoclar Vivadent, Liechtenstein.

Melting points:

The melting points were measured with an OptiMelt – Automated Melting Point System. For that the samples had to be put in a one side open capillary (80 x 1.3 mm).

Orange light lab:

All weigh-ins, reactions and measurements of light sensitive substances were carried out in an orange light lab. The windows are laminated with Asmetec metolight SF-UV-foils (type ASR-SF-LY5) and all lamps are of the type Osram lumix with chip controlled light color 62.

^{1}H-, ^{13}C- and ^{31}P-NMR:

Spectra were measured with a BRUKER Avance DRX-400 FT-NMR spectrometer. The chemical shift was reported in ppm (s = singlet, d = doublet, t = triplet, q = quartet, m = multiplet). Deuterated chloroform ($CDCl_3$, 99.5% deuteration), deuterated benzene (C_6D_6, 99.9% deuteration) deuterated acetone ($(CD_3)_2CO$, 99.8% deuteration) and deuterated DMSO (DMSO-d_6, 99.8% deuteration) were used as solvents. Analysis of the spectra was performed with the software MestrReNova (version number: 14.1.0-24037).

Ultra-High-Pressure Liquid Chromatography-mass spectroscopy (UHPLC-MS):

HPLC analysis was performed on a Nexera X2® UHPLC system (Shimadzu®) comprised of LC- 30AD pumps, SIL-30AC autosampler, CTO-20AC column oven and DGU-20A5/3 degasser module. Detection was done using an SPD-M20A photo diode array, an RF-20Axs fluorescence detector, and ELS-2041 evaporative light scattering

detector (JASCO®) and an LC-MS-2020 mass spectrometer (ESI/APCI). If not stated otherwise, all separations were performed using a Waters® XSelect® CSHTM C18 2,5 µm (3.0 x 50 mm) column XP at 40 °C, and a flowrate of 1.7 mL/min with water/acetonitrile + 0.1% formic acid gradient elution.

Karl Fischer titrations (KFT)

KFTs were performed using an Envirotech CA-21 moisture meter with the anode solution "Aquamicron AX Karl Fischer Reagent for Coulometric Moisture Meter" containing methanol, propylene carbonate, 2,2'-iminodiethanol, sulfodioxide and iodine. As a cathode solution, the reagent "Aquamicron CXU Karl Fischer Reagent for Coulometric Moisture Meter" was used, which contains methanol, ethane-1,2-diol and choline chloride. In order to measure the water content, an appropriate amount of reagent (0.1 – 0.3 mL) was weighed in a syringe with mg accuracy and injected into the device. Liquid reagents could be measured without further preparation steps. The titration device displayed the amount of water in mg and simultaneously in ppm referring to the sample weight that was entered.

Silica column chromatography:

The analysis was performed with a Büchi MPLC-system equipped with the control unit C-620, fraction collector C-660, RI detector and UV-photometer C-635. As stationary phase Merck silica gel 60 (0.040-0.063 mm) was used.

Thin Layer Chromatography:

TLC was carried out by using TL-aluminum foils coated with silica gel (60 F245) from Merck.

Photo-DSC

Photo-DSC measurements were conducted on a Photo-DSC 204 F1 from Netzsch, using 15 µL aluminum pans. An Omnicure 2000 from Lumen Dynamics with glass fiber light wave guides was used as light source, which was calibrated *via* an Omnicure R2000 radiometer. All measurements were conducted under N2-atmosphere (flow rate: 20 mL min-1). The data analysis was performed with the program Netzsch Proteus Thermal Analysis in version 8.0.1.

For irradiating the samples, an OmniCure LX400 **UV-LED-spot curing system** was used with a 385 and 405 nm LED. In order to measure the light intensity an Ocean Optics 2000+ USB device was used with the SpectraSuit.

Additionally, an OmniCure 2000, equipped with a 320-500 nm filter and a single-tube liquid filled light guide with a diameter of 8 mm, was used. The **UV source** was calibrated at least once a day with an Omnicure R2000 radiometer.

UV-Vis Measurments:

UV-Vis measurements were performed on a *Thermo Scientific NanoDrop Onec Microvolume* UV-Vis spectrophotometer in ACN solutions. (1 mM)

Steady State Photolysis

All the instruments were purchased from ASEQ instruments, Canada.

Light sources: D2-S2 UV/VIS/NIS Deuterium/Tungsten light source and Optical fiber coupler for D2-S2 light source

Spectrometer: LR1 spectrometer, 300-1000nm, 1nm resolution/50um slit, 1m (400um core) optical fiber for 200-1200nm, software (ASEQ_16bitsV1_14), external trigger.

Light guides: 8 fiber bundle (solarization resistant) 1m with metal jacket and SMA905 Connectors (connecting the light source and cuvette) and 1 fiber bundle (solarization resistant) 1m with metal jacket and SMA905 Connectors (connecting the cuvette and detector).

All the measurements were performed in red light lab (dark room with LEDs λmax = 620 nm as the only light source).

SUMMARY

Modern dentistry requires the development of dental restoratives that have whiter hues and can be applied more efficiently. To achieve these advantages, new photo-initiating systems must be developed that can achieve sufficient curing depth and the desired color of the formulations. Currently, the state-of-the-art photoinitiator is the CQ/DMAB initiating system represented in Figure 61.

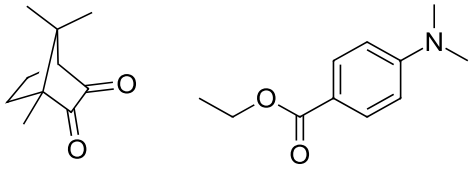

Figure 61: Camphorquinone (CQ) and dimethylamino benzoate (DMAB)

Even though, this photoinitiator shows great absorption at long wavelengths, it comes with some typical disadvantages of Norrish Type II photoinitiators. Firstly, they show a lower reactivity due to their bimolecular nature. Furthermore, they do not meet the requirement of white dental restoratives, because CQ, as well as the unreacted amine in formulations, can lead to the yellowing of the formulations. Additionally, they show insufficient photobleaching. For this reason, new highly reactive Norrish Type I photoinitiators that do not cause yellowing and show a photobleaching effect are to be investigated. The main drawback of Type I photoinitiators is however their absorption maximum does not overlap well with the emission band of currently used dental lamps. Therefore, the development of Type I photoinitiators that show a bathochromic redshift is to be developed.

Type I photoinitiators that fulfill the mentioned requirements such as non-yellowing, photobleaching effect and high efficiency are monoacylphosphine oxide (**MAPO**). The objective of this work is, therefore, the development of new **MAPO** derivatives that would preferably show a bathochromic redshift and higher (similar) efficiency compared to state-of-the-art **MAPO** photoinitiators such as **TPO** and **TPO-L**. (Figure 62)

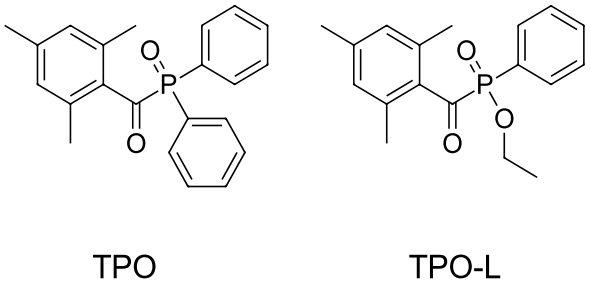

*Figure 62: Structures of commercially available **MAPO** photoinitiators **TPO** and **TPO-L***

The modification of **MAPO**-derivatives in this work was performed with amine. Since the bathochromic shift of **MAPO** molecules originates from n→π* transitions caused by interactions of an empty d-orbital of phosphorus and π*-orbital of the carbonyl carbon atom, electron-donating substituent like amine on phosphorus, should be able to induce further bathochromic shift. The amines that were investigated in this work are represented in Figure 63.

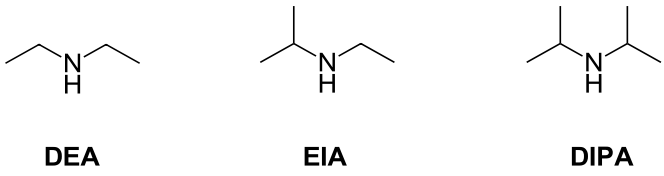

Figure 63: Structures of the used amines. Diethylamine (DEA), ethyl isopropyl amine (EIA) and diisopropyl amine (DIPA)

The synthesis of **4** (Figure 64) was carried out successfully. To explore the properties of the synthesized photoinitiator, its absorption characteristics were examined using UV-Vis spectroscopy. The analysis revealed that the product exhibits an absorption maximum of 390 nm, which represents a bathochromic shift of approximately 10 nm when compared to **TPO**.

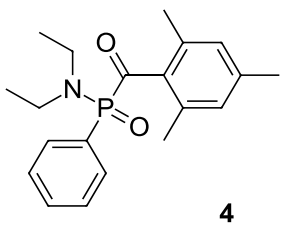

*Figure 64: Chemical structure of photoinitiator **4***

Furthermore, the photo-curing speed of the product was assessed through photo-DSC measurements. The results of the measurements indicated that the performance of the synthesized product was like that of **TPO-L** and notably lower than that of **TPO**. This outcome can be attributed to the higher electronegativity of oxygen in **TPO-L** and

nitrogen in **4** in comparison to the carbon electronegativity within the phenyl ring of **TPO**. Additionally, quantum yield of this photoinitiator was determined and compared to **TPO** and **TPO-L**. The results are in a very good agreement with the performed photo-DSC studies, where the reactivity of **4** is much lower than **TPO** or **TPO-L**.

Based on the results obtained from the synthesis conducted in this study, it is evident that molecules with greater steric hindrance were unable to effectively substitute phosphorus. This is evident when comparing the reaction outcomes of precursor compound **3** with diethyl amine (**4**) and diisopropyl amine (**5**). As diisopropyl amine possesses significantly higher steric hindrance compared to diethyl amine, the reactions involving diisopropyl amine did not yield the desired product, even in limited quantities. The same results were observed with ethyl isopropyl amine (**6**).

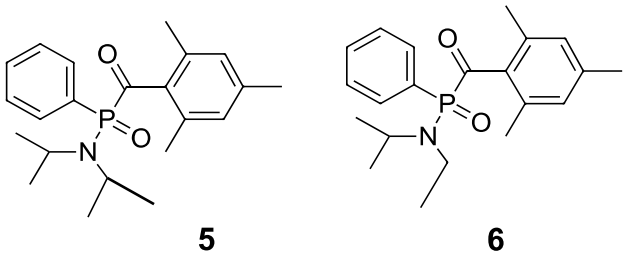

*Figure 65: Chemical structures of **5** (left) and **6** (right).*

The steric effects may also account for the lack of success in both synthetic approaches for the synthesis phosphorus substituted **MAPO 9** (Figure 66). Given that these reactions were conducted as Grignard reactions with considerably greater driving forces, the formation of the desired products was anticipated, even if in smaller quantities. However, both ^{31}P-NMR and UPLC-MS analyses failed to reveal any evidence of successful reactions. Moreover, the same reasoning can be extended to the synthesis of oxygen substituted **MAPO 10** (Figure 66).

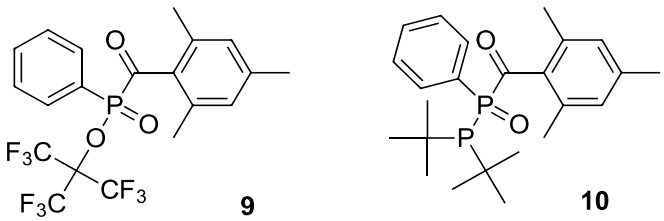

*Figure 66: Chemical structures of **9** (left) and **10** (right).*

The synthesis of sulfur **7** and selenium **8** substituted **MAPO**s (Figure 67) was performed as well. According to the results obtained through UPLC-MS analysis, it was established that the desired products were indeed synthesized. However, one of the significant

challenges we faced was identifying an appropriate purification method. In the case of **7**, the product was observed to decompose, rendering it unsuitable for further use. On the other hand, **8** displayed initial stability but exhibited signs of decomposition over time following purification, making it impossible to be isolated.

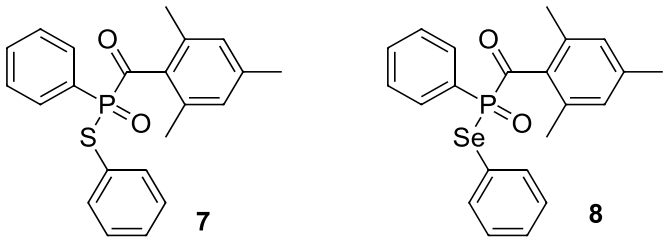

*Figure 67: Chemical structures of **7** (left) and **8** (right).*

The synthesis of compounds **11** and **12** (Figure 68), proved to be unsuccessful despite multiple attempts and varying methods. The precipitates that formed during the reactions were identified as sodium 2,4,6-trimethylbenzoylphenyl phosphinate (Figure 53) or compound **2**. Even though the reactions were conducted under air exclusion, and all reagents were thoroughly dried before the synthesis, it is plausible that the desired molecules were indeed synthesized but are highly unstable. They appear to hydrolyze into **2** almost immediately after the reaction. The trace amounts of water necessary for this hydrolysis might originate from the acetonitrile used in the synthesis. Karl Fischer titration revealed that the acetonitrile used contained 9.97 ppm of water.

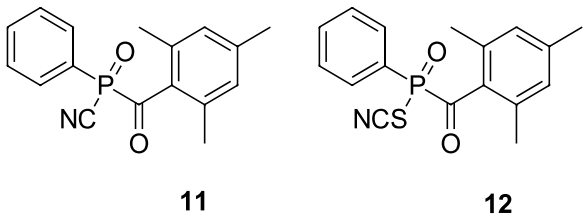

*Figure 68: Chemical structures of **11** (left) and **12** (right).*

Besides nucleophilic reactions, electrophilic reactions were investigated as a possible new synthetic route to **MAPO** photoinitiators (Figure 69). The reactions were performed as multi-step reactions, starting with the successful monoacylation of phenyl phosphine (**13**). However, in the second step, an electrophilic reaction with cyclohexyl isocyanate (**14**) the formation of various phosphorus-containing byproducts was observed. Sadly, the subsequent oxidation (**15**) step resulted in the formation of new byproducts. The purification of crude product was performed via MPLC column chromatography.

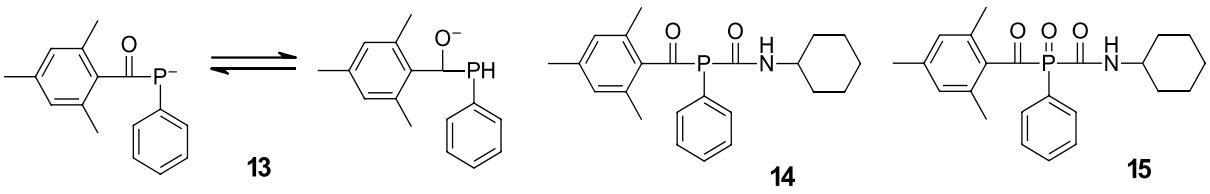

*Figure 69: Chemical structures of **13,14,15***

Since there was no prior literature data available for the target molecule, positively identifying product **15** was a challenge using only ^{31}P-NMR analysis. This was further complicated by the presence of multiple phosphorus-containing products in the collected fraction. To gain more clarity, ^{1}H and ^{13}C-NMR analyses were conducted, which did not eliminate the possibility of the presence of product **15**. Consequently, we proceeded to examine the absorption properties and performance of both the crude product and the collected fraction.

In the conducted UV-Vis measurements a significant difference in absorption levels between the crude product and the collected fraction can be observed. The collected fraction exhibited a very low overall absorption. The UV-Vis spectra analysis also indicates that neither the crude product nor the collected fraction displayed the typical absorption band associated with **MAPO** molecules.

The photo-DSC study results showed that **TPO** and **TPO-L** show a better performance than crude product or collected fractions. However, the crude product outperforms the collected fraction, which aligns with expectations based on the UV-Vis measurement results of these two photoinitiators.

In conclusion, it is difficult to conclusively eliminate the possibility of the desired product presence in either the crude or collected fraction, based on the analyses performed. Nevertheless, the synthesized product, as revealed by performance and absorption measurements, demonstrates a lower overall performance in comparison to state-of-the-art **MAPO** photoinitiators.

ABBREVIATIONS

Ar	Argon
BAPO	Bisacylphosphine oxide
bis-GMA	Bisphenol A diglycidylmethacrylate
$CDCl_3$	Deuterated chloroform
CQ	Camphorquinone
D_3MA	Decanediol dimethacrylate
DBC	Double bond conversion
DCC	Dicyclohexylcarbodiimide
DCM	Dichloromethane
DEA	Diethylamine
DEAPO	4-Dimethylaminobenzoyldiphenylphosphine oxide
DHAPO	4-Dihexylaminobenzoyldiphenylphosphine oxide
DIPA	Diisopropyl amine
DMAB	Dimethylaminobenzoic acid
DMAPO	4-Dimethylaminobenzoyldiphenylphosphine oxide
dme	Dimethoxyethane
EIA	Ethyl isopropyl amine
Ivocerin	Bis(4-methoxybenzoyl)diethylgermanium
LED	Light emitting diode.
MAPO	Monoacylphosphine oxide
MPLC	Medium pressure liquid chromatography
NMR	Nuclear magnetic resonance spectroscopy
Photo-DSC	Photo-differential scanning calorimetry
PI	Photoinitiator
rt	Room temperature
TBAB	Tetrabutylammonium bromide
TEA	Triethylamine
TLC	Thin layer chromatography
TPO	2,4,6-Trimethylbenzoyldiphenyl phosphine oxide

TPO-L	Ethyl (2,4,6-trimethylbenzoyl) phenylphosphinate
UDMA	Urethanedimethacrylate
UPLC-MS	Ultra-performance liquid chromatography–mass spectrometry
UV-Vis	Ultraviolet and visible light

REFERENCES

1. *Future Use of Materials for Dental Restoration*. (2010).
2. Bates, M. N. Mercury amalgam dental fillings: An epidemiologic assessment. *Int J Hyg Environ Health* **209**, 309–316 (2006).
3. Chun, K. J., Choi, H. H. & Lee, J. Y. Comparison of mechanical property and role between enamel and dentin in the human teeth. *J Dent Biomech* **5**, 1–7 (2014).
4. Albert, P., Dermann, K. & Rentsch, H. Amalgam und die alternativen. *Chemie in Unserer Zeit* **34**, 300–305 (2000).
5. Moszner, N. & Salz, U. *New Developments of Polymeric Dental Composites*. www.elsevier.com/locate/ppolysci.
6. Lai, H., Peng, X., Li, L., Zhu, D. & Xiao, P. Novel monomers for photopolymer networks. *Progress in Polymer Science* vol. 128 Preprint at https://doi.org/10.1016/j.progpolymsci.2022.101529 (2022).
7. Gruber, H. F. *PHOTOINITIATORS FOR FREE RADICAL POLYMERIZATION*. *Prog. Polym. Sci* vol. 17 (1992).
8. Andrzejewska, E. *Photopolymerization Kinetics of Multifunctional Monomers*. www.elsevier.com/locate/ppolysci.
9. Crivello, J. V., Dietliker, K. (1998). Photoinitiators for Free Radical Cationic & Anionic Photopolymerisation. Deutschland: Wiley.
10. Müller, S. M., Schlögl, S., Wiesner, T., Haas, M. & Griesser, T. Recent Advances in Type I Photoinitiators for Visible Light Induced Photopolymerization. *ChemPhotoChem* vol. 6 Preprint at https://doi.org/10.1002/cptc.202200091 (2022).
11. Randy, Jablonski Diagram. 2015: For Diagrams.
12. Hanson, K. *et al.* A paradigm for blue- or red-shifted absorption of small molecules depending on the site of π-extension. *J Am Chem Soc* **132**, 16247–16255 (2010).
13. George Drobny, J. *Radiation Technology for Polymers, Second Edition*.

14. Ganster, B., Fischer, U. K., Moszner, N. & Liska, R. New photocleavable structures. Diacylgermane-based photoinitiators for visible light curing. *Macromolecules* **41**, 2394–2400 (2008).

15. *2 RADTECH REPORT ISSUE 4 2014 New Generation of Highly Efficient, Long-Wavelength Photoinitiators for Dental Restoratives: From Research to Application*.

16. Mitterbauer, M., Haas, M., Stüger, H., Moszner, N. & Liska, R. Tetrakis(2,4,6-Trimethylbenzoyl)Silane—A Novel Photoinitiator for Visible Light Curing. *Macromol Mater Eng* **302**, (2017).

17. Dai, N., Cai, Z., Zhang, X. & Li, K. The effects and mechanism of the magnetic field on the hydrogen abstraction reaction of benzophenone and isopropanol. *Chem Phys* **555**, (2022).

18. Stadler, E. *et al.* A versatile method for the determination of photochemical quantum yields: Via online UV-Vis spectroscopy. *Photochemical and Photobiological Sciences* **17**, 660–669 (2018).

19. Asmussen, S., Arenas, G., Cook, W. D. & Vallo, C. Photoinitiation rate profiles during polymerization of a dimethacrylate-based resin photoinitiated with camphorquinone/amine. Influence of initiator photobleaching rate. *Eur Polym J* **45**, 515–522 (2009).

20. Asmusen, S., Arenas, G., Cook, W. D. & Vallo, C. Photobleaching of camphorquinone during polymerization of dimethacrylate-based resins. *Dental Materials* **25**, 1603–1611 (2009).

21. Kowalska, A., Sokolowski, J. & Bociong, K. polymers The Photoinitiators Used in Resin Based Dental Composite-A Review and Future Perspectives. (2021) doi:10.3390/polym130.

22. Ikemura, K., Ichizawa, K., Yoshida, M., Ito, S. & Endo, T. *UV-VIS Spectra and Photoinitiation Behaviors of Acylphosphine Oxide and Bisacylphosphine Oxide Derivatives in Unfilled, Light-Cured Dental Resins*. *Dental Materials Journal* vol. 27 (2008).

23. *Special Feature Ivocerin ®-a Milestone in Composite Technology*. www.ivoclarvivadent.com.

24. Jockusch, S. *et al. A Steady-State and Picosecond Pump-Probe Investigation of the Photophysics of an Acyl and a Bis(Acyl)Phosphine Oxide*. https://pubs.acs.org/sharingguidelines (1997).

25. Li, Q. *et al.* Bifunctional free radical photoinitiator based on syringaldehyde. *Polym Adv Technol* **33**, 1617–1627 (2022).

26. Kim, G. T. *et al.* Cytotoxicity, Colour Stability and Dimensional Accuracy of 3D Printing Resin with Three Different Photoinitiators. *Polymers (Basel)* **14**, (2022).

27. Wu, Y. P. *et al.* New acyl phosphine oxides as high-performance and low migration type I photoinitiators of radical polymerization. *Prog Org Coat* **168**, (2022).

28. Manojlovic, D. *et al.* Cytotoxicity and genotoxicity of a low-shrinkage monomer and monoacylphosphine oxide photoinitiator: Comparative analyses of individual toxicity and combination effects in mixtures. *Dental Materials* **33**, 454–466 (2017).

29. Zeng, B. *et al.* Cytotoxic and cytocompatible comparison among seven photoinitiators-triggered polymers in different tissue cells. *Toxicology in Vitro* **72**, (2021).

30. Sitzmann, E. V *et al. Low Color Liquid Acylphosphine Oxide Photoinitiators Blends for UV Coating Applications*.

31. Müller, S. M., Schlögl, S., Wiesner, T., Haas, M. & Griesser, T. Recent Advances in Type I Photoinitiators for Visible Light Induced Photopolymerization. *ChemPhotoChem* vol. 6 Preprint at https://doi.org/10.1002/cptc.202200091 (2022).

32. Duan, H. *et al.* Monoacylphosphine oxides with substituents in the phosphonyl moiety as Norrish I photoinitiators: Synthesis, photoinitiattion properties and mechanism. *J Photochem Photobiol A Chem* **421**, (2021).

33. Zhang, J. Q. & Han, L. B. Chlorosilane-Catalyzed Coupling of Hydrogen Phosphine Oxides with Acyl Chlorides Generating Acylphosphine Oxides. *Org Lett* **22**, 4633–4637 (2020).

34. Roszkowski, P. *et al.* Synthesis and evaluation of new radical photoinitiators bearing trialkoxysilyl groups for surface immobilization. *Polymer (Guildf)* **129**, 207–220 (2017).

35. Liu, Y. *et al.* Naphthyl-based acylphosphine oxide photoinitiators with high effiency and low migration. *Prog Org Coat* **142**, (2020).

36. Xie, C. *et al.* A novel acyl phosphine compound as difunctional photoinitiator for free radical polymerization. *Prog Org Coat* **135**, 34–40 (2019).

37. Nazir, R., Danilevicius, P., Gray, D., Farsari, M. & Gryko, D. T. Push-pull acylophosphine oxides for two-photon-induced polymerization. *Macromolecules* **46**, 7239–7244 (2013).

38. Dumur, F. The future of visible light photoinitiators of polymerization for photocrosslinking applications. *Eur Polym J* **187**, (2023).

39. Oesterreicher, A. *et al.* Low migration type I photoinitiators for biocompatible thiol-ene formulations. *Eur Polym J* **88**, 393–402 (2017).

40. Roszkowski, P. *et al.* Synthesis and evaluation of new radical photoinitiators bearing trialkoxysilyl groups for surface immobilization. *Polymer (Guildf)* **129**, 207–220 (2017).

41. Ribas-Massonis, A., Cicujano, M., Duran, J., Besalú, E. & Poater, A. Free-Radical Photopolymerization for Curing Products for Refinish Coatings Market. *Polymers* vol. 14 Preprint at https://doi.org/10.3390/polym14142856 (2022).

42. Lehóczki, T., Józsa, É. & Osz, K. Ferrioxalate actinometry with online spectrophotometric detection. *J Photochem Photobiol A Chem* **251**, 63–68 (2013).

43. Atchard, C. G. H. *A New Sensitive Chemical Actinometer II. Potassium Ferrioxalate as a Standard Chemical Actinometer*. vol. 8 https://royalsocietypublishing.org/.

44. Wang, C. *et al. Supporting Information for Direct 18 F-Labeling of Biomolecules via Spontaneous Site-Specific Nucleophilic Substitution by F-on Phosphonate Prostheses*.

45. Arisawa, M., Sawahata, K., Yamada, T., Sarkar, D. & Yamaguchi, M. Rhodium-Catalyzed Insertion Reaction of PhP Group of Pentaphenylcyclopentaphosphine with Acyclic and Cyclic Disulfides. *Org Lett* **20**, 938–941 (2018).

46. Xiong, B. *et al.* DCC-assisted direct esterification of phosphinic and phosphoric acids with O-nucleophiles. *Phosphorus Sulfur Silicon Relat Elem* **193**, 239–244 (2018).

47. Suzuki, K. ; K. N. ; I. N. ; H. S. ; S. H. Organic magnesium phosphide and method for producing same, organic magnesium phosphide complex and method for producing same, and method for producing organic phosphorus-containing compound using said phosphide. WO2018008510, 2018. (2018).

48. G. Ullrich; B. Ganster; U. Salz; N. Moszner; R. Liska. Water soluble bisacylphosphine oxides for the photopolymerisation of acidic aqueous dental formulations. *Journal of Polmyer Science: Part A: Polymer Chemistry 2006, 44, 1686*.

49. Shi, E. & Pei, C. Phase-transfer catalyzed pseudohalogenation of phosphorochloridates. *Synth Commun* **35**, 669–673 (2005).

50. Li, Z., Kuang, Y., Guo, F. & Hou, Y. *Synthesis and Properties of 5,5-Dimethyl-l,3?2-Dioxa Phosphoro Cyclohexane Phosphoryl Thioureas*.

51. Müller, G. S. Phosphorus Based Photoinitiators: Synthesis and Application. (Swiss Federal Institute of Technology (ETH Zurich), 2013).

52. Benedikt, S. *et al.* Highly efficient water-soluble visible light photoinitiators. *J Polym Sci A Polym Chem* **54**, 473–479 (2016).

Appendix

Synthesis of 1

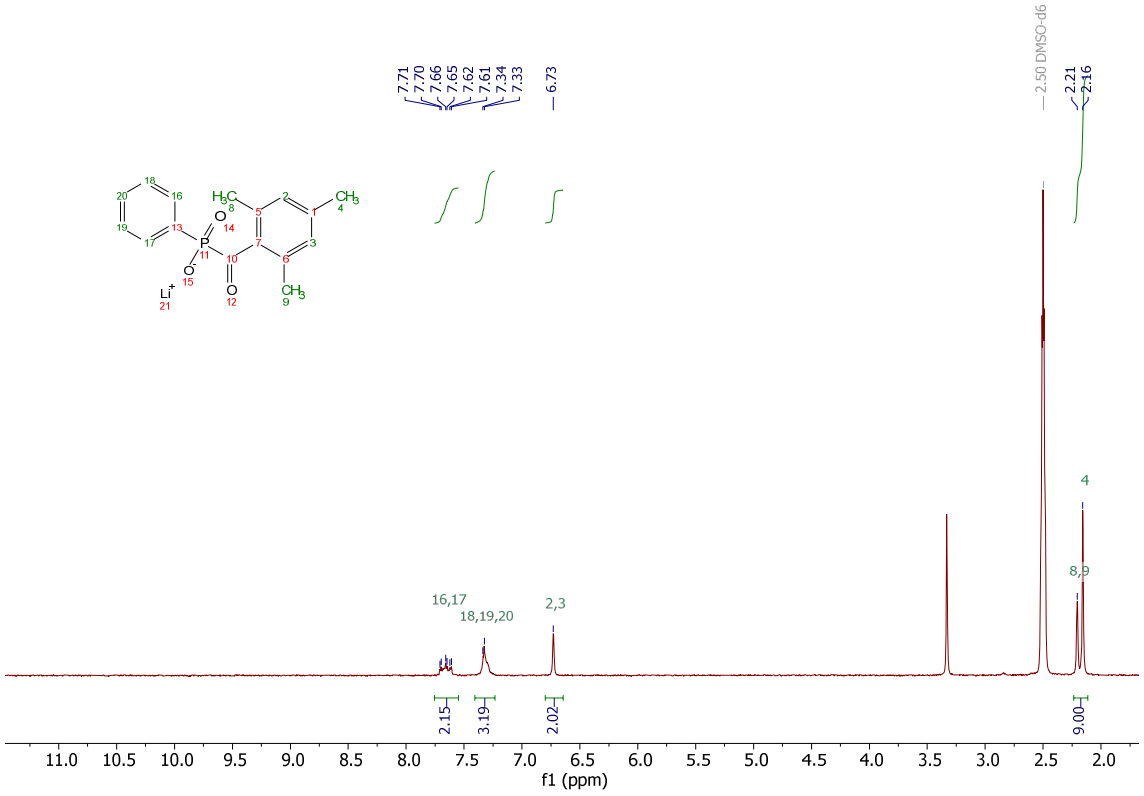

*Figure S 1: ^{1}H NMR (200 MHz, DMSO) of **1.***

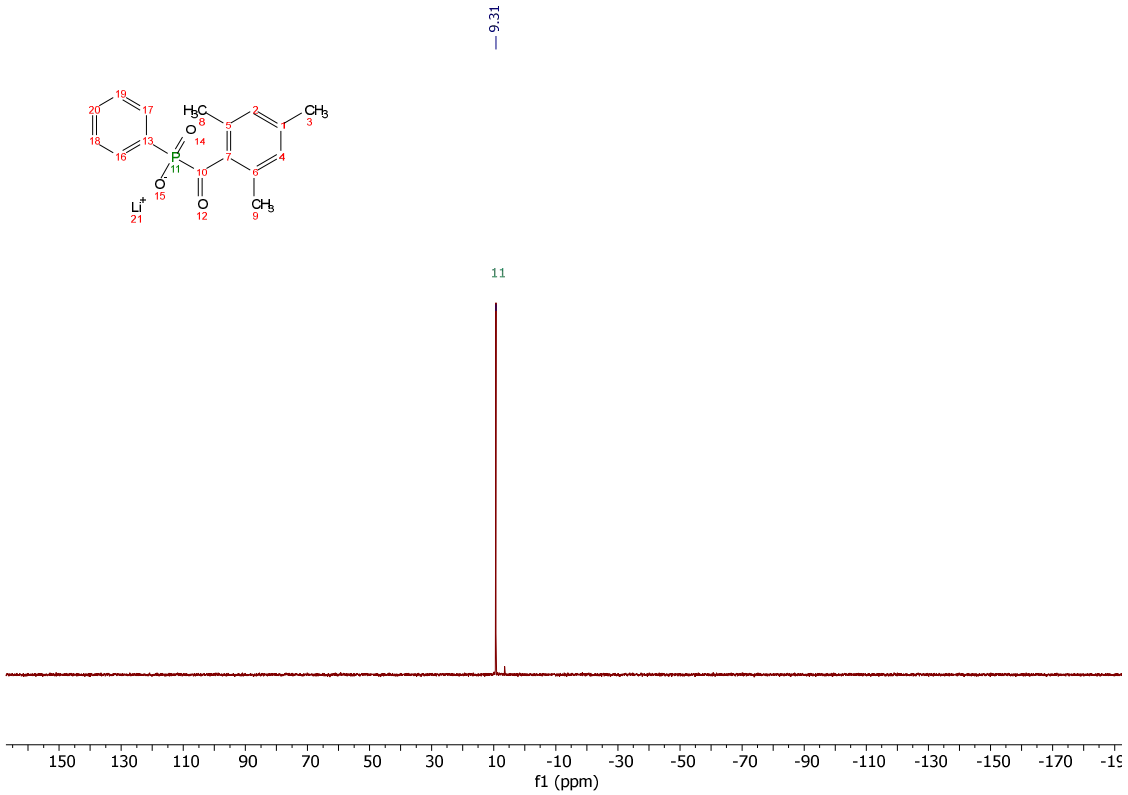

*Figure S 2: ^{31}P NMR (101 MHz, DMSO) of **1.***

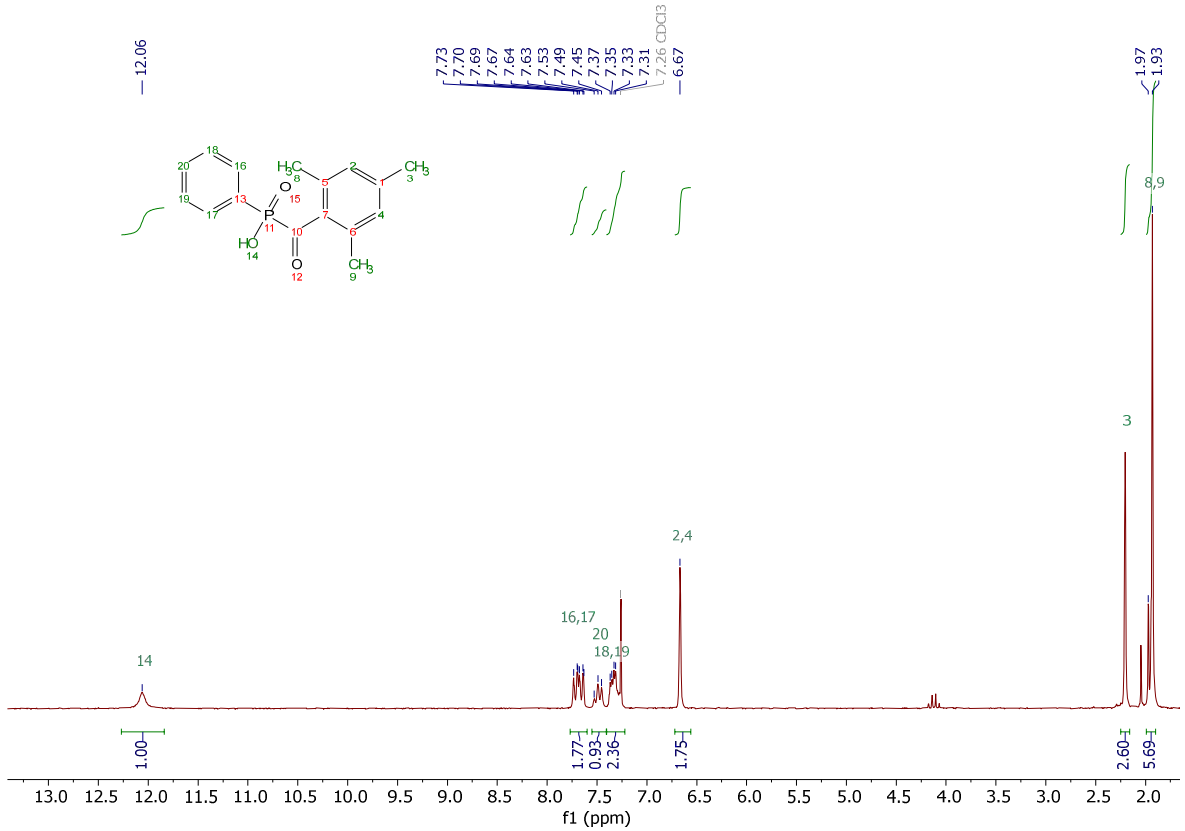

*Figure S 3: ^{1}H NMR (200 MHz, $CDCl_3$) of **2***

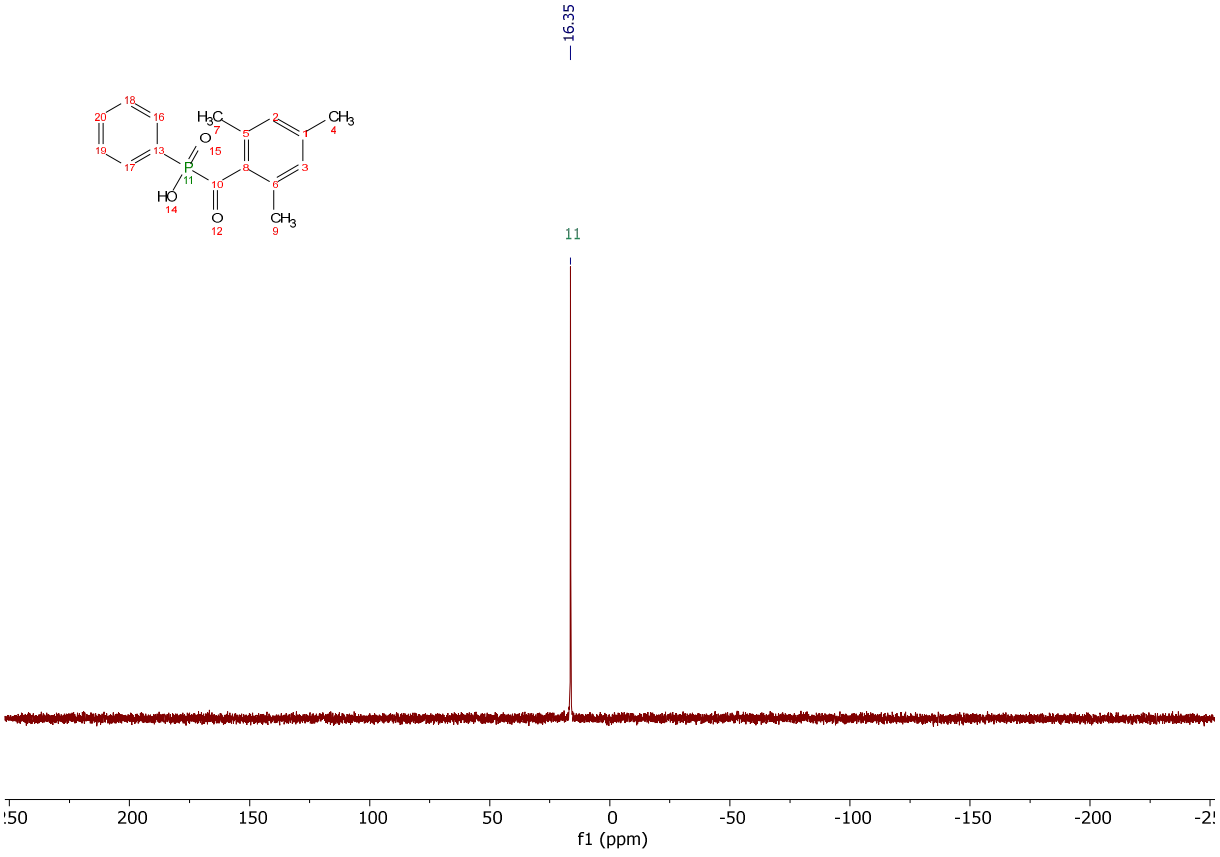

*Figure S 4: ^{31}P NMR (101 MHz, $CDCl_3$) of **2***

Synthesis of 3

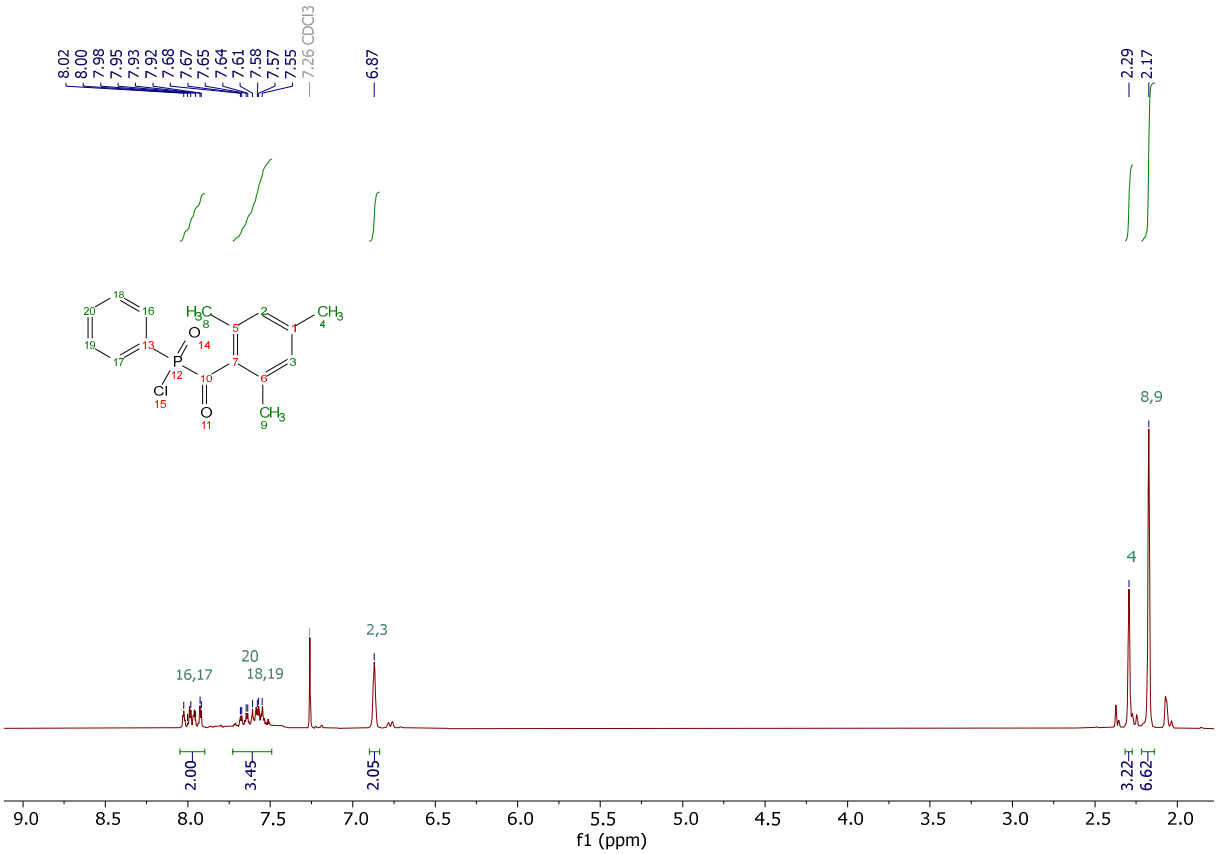

*Figure S 5: ^{1}H NMR (200 MHz, $CDCl_3$) of **3** synthesized with oxalyl chloride*

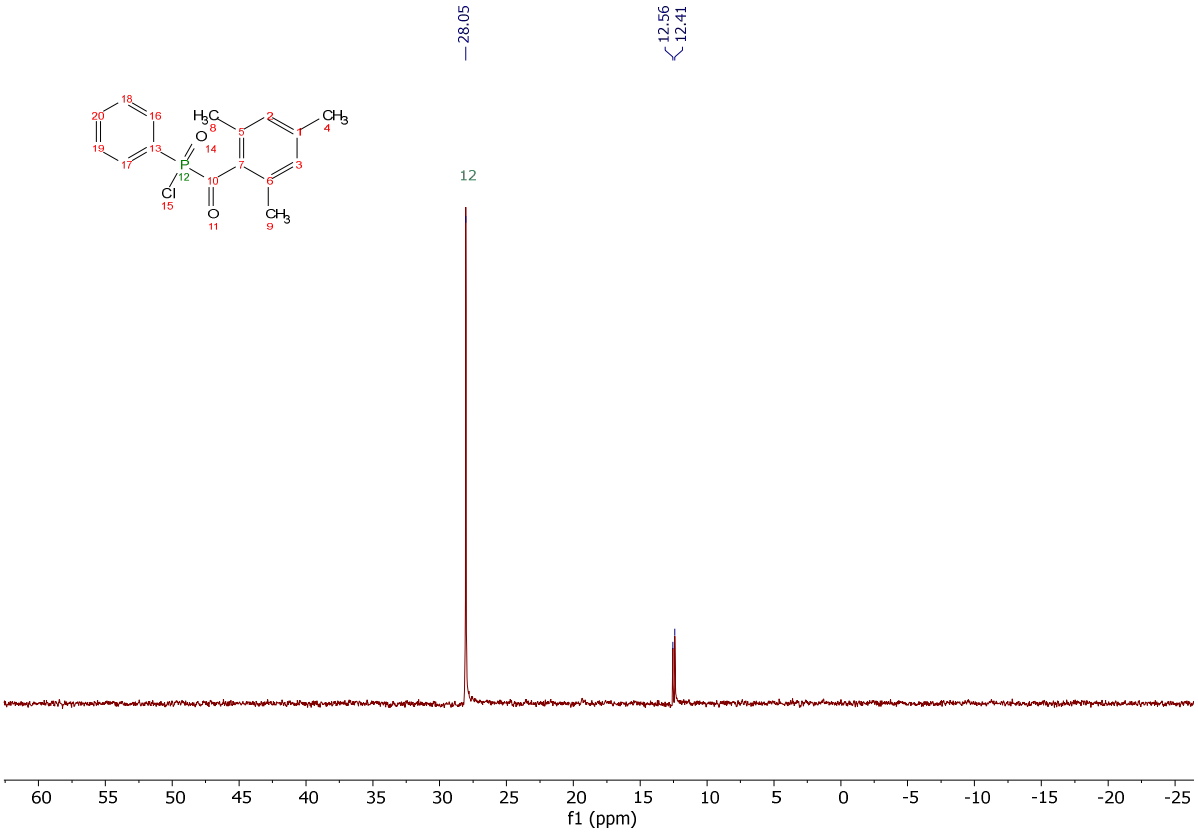

*Figure S 6: :^{31}P NMR (101 MHz, $CDCl_3$) of **3** synthesized with oxalyl chloride.*

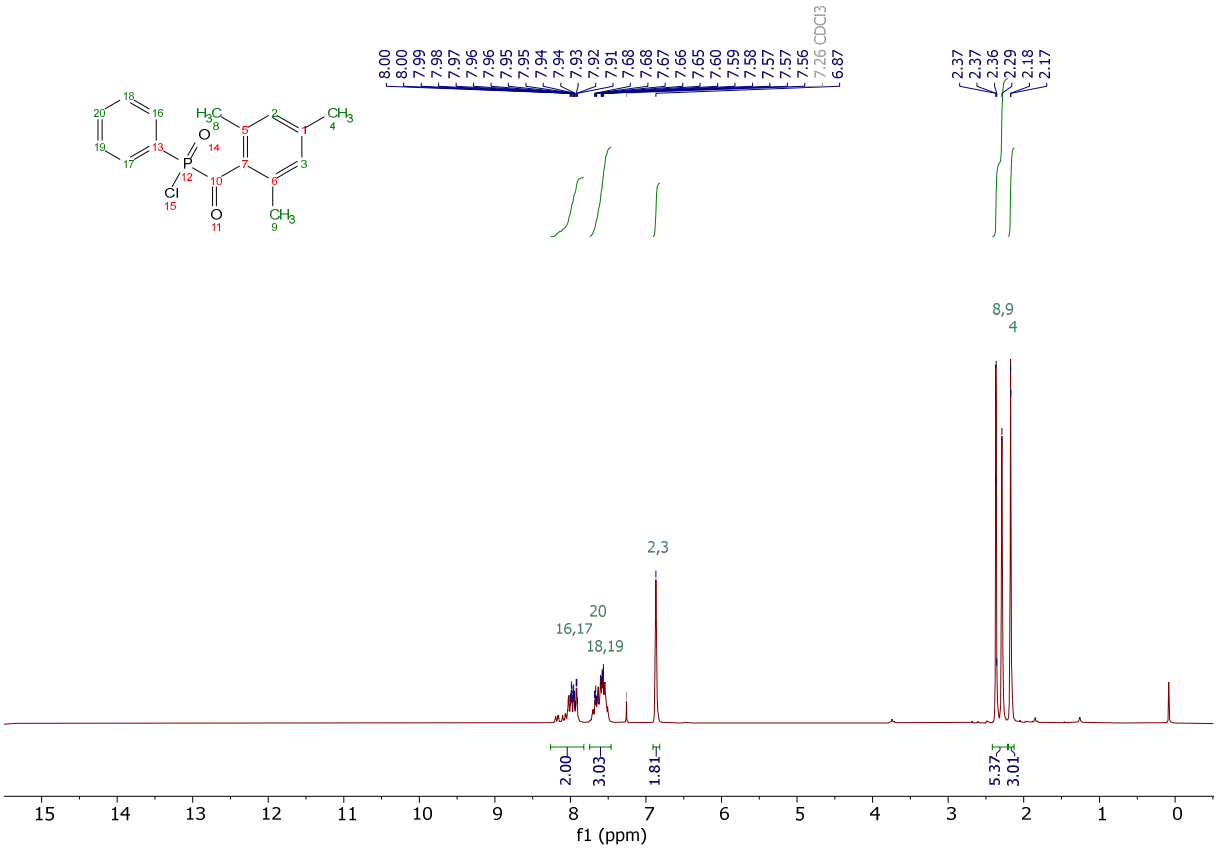

*Figure S 7: ^{1}H NMR (200 MHz, $CDCl_3$) of **3** synthesized with thionyl chloride.*

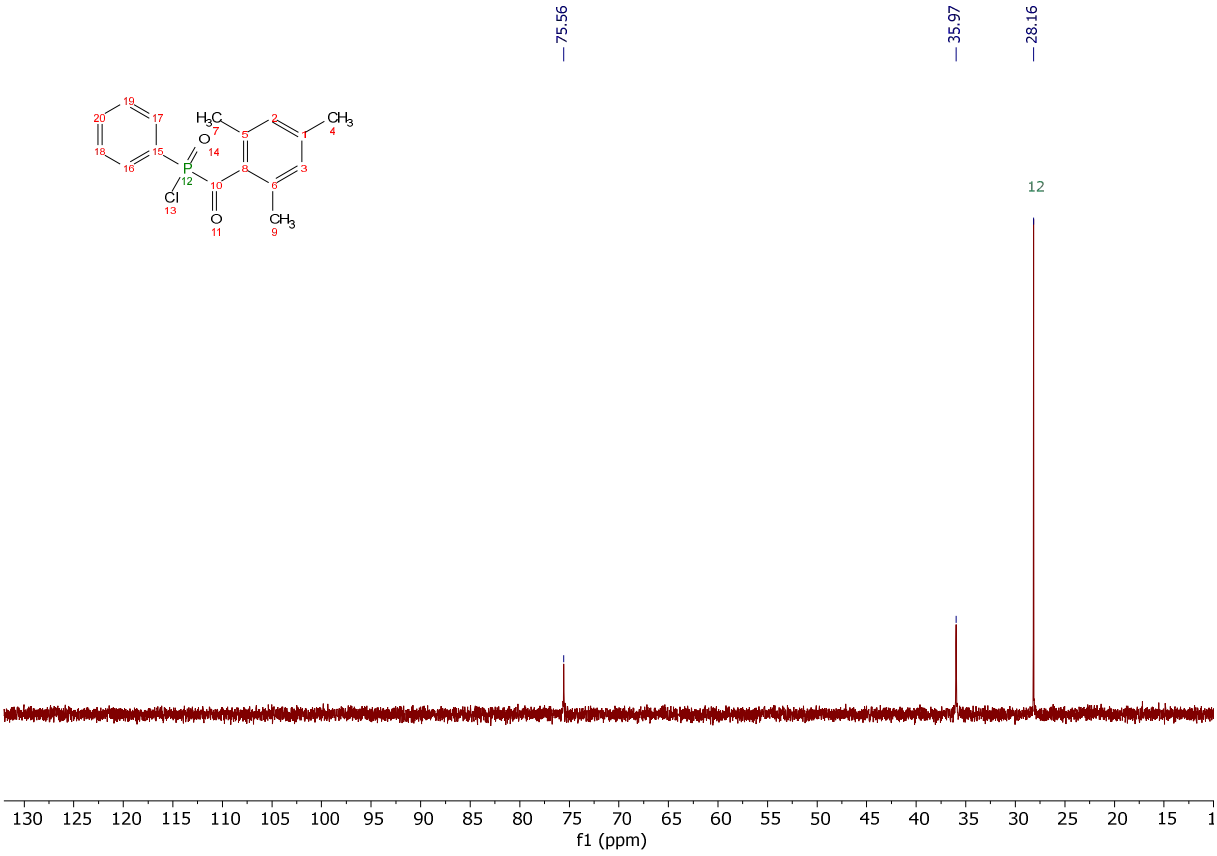

*Figure S 8: ^{31}P NMR (101 MHz, $CDCl_3$) of **3** synthesized with thionyl chloride.*

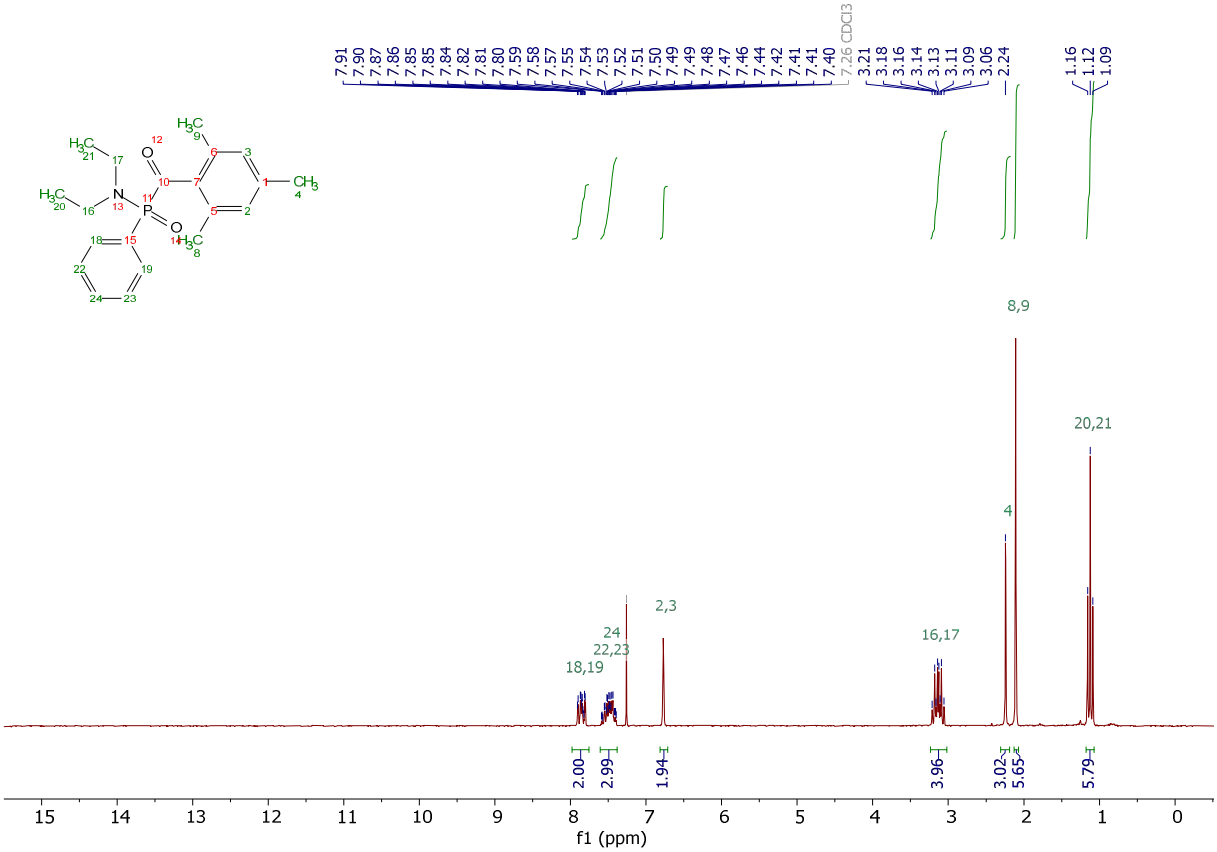

*Figure S 9: ^{1}H NMR (200 MHz, $CDCl_3$) of **4***

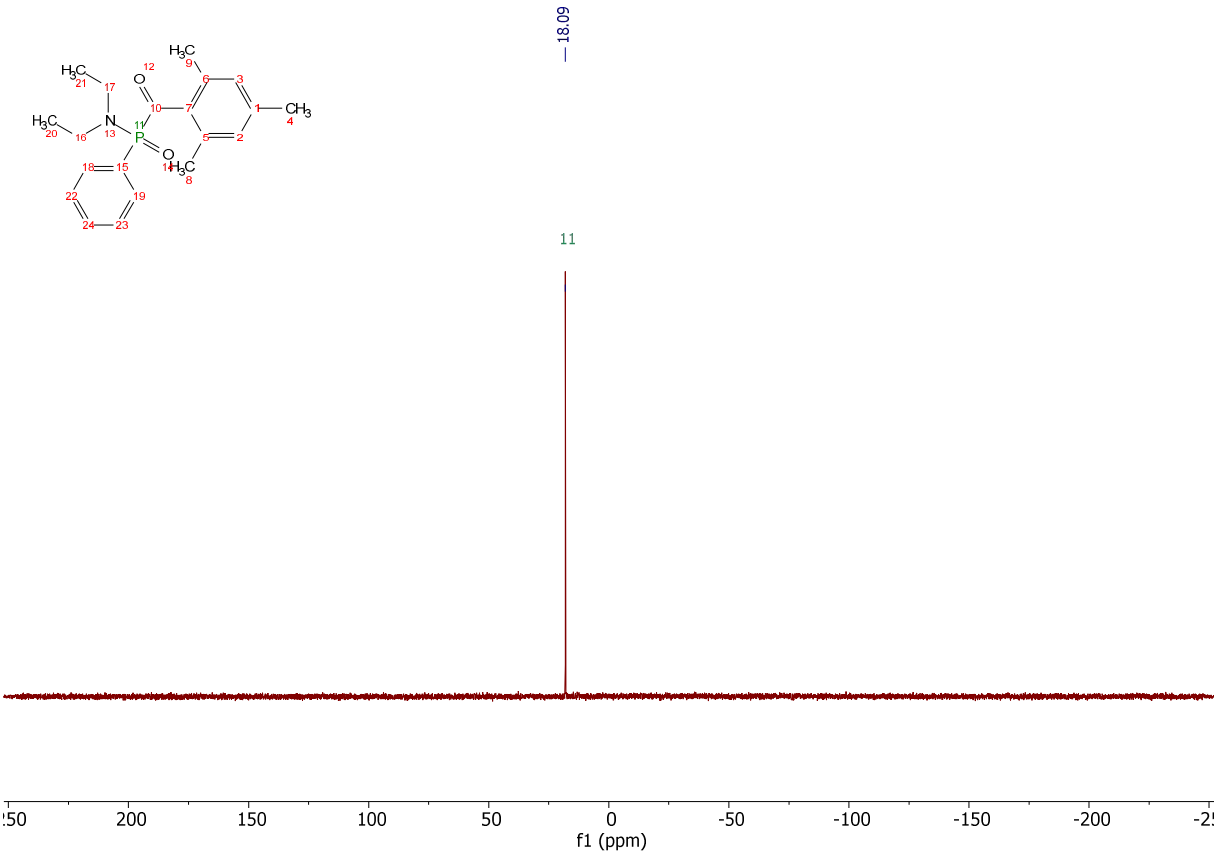

*Figure S 10: ^{31}P NMR (101 MHz, $CDCl_3$) of **4***

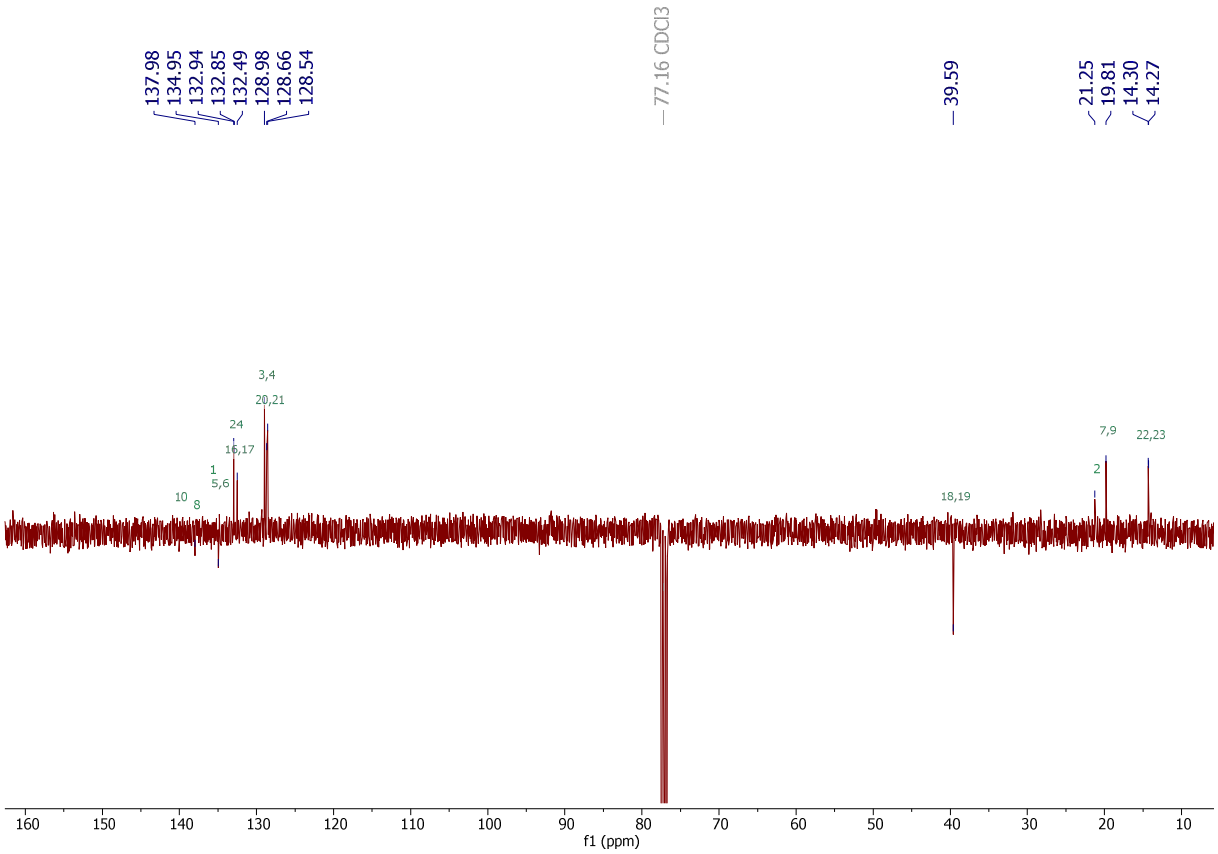

*Figure S 11: ^{13}C NMR (101 MHz, $CDCl_3$) of **4***

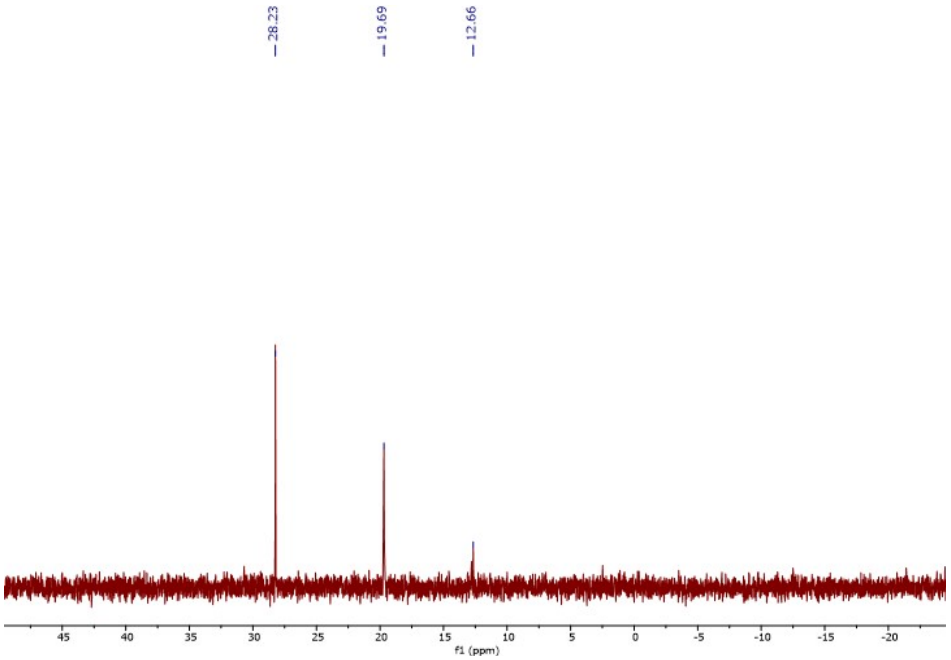

*Figure S 12: ^{31}P NMR (101 MHz, $CDCl_3$) of the reaction mixture of **5** after 1 h reaction time in toluene. (reaction mixture: 2 eq. ethyl isopropyl amine, 1 eq. **3**)*

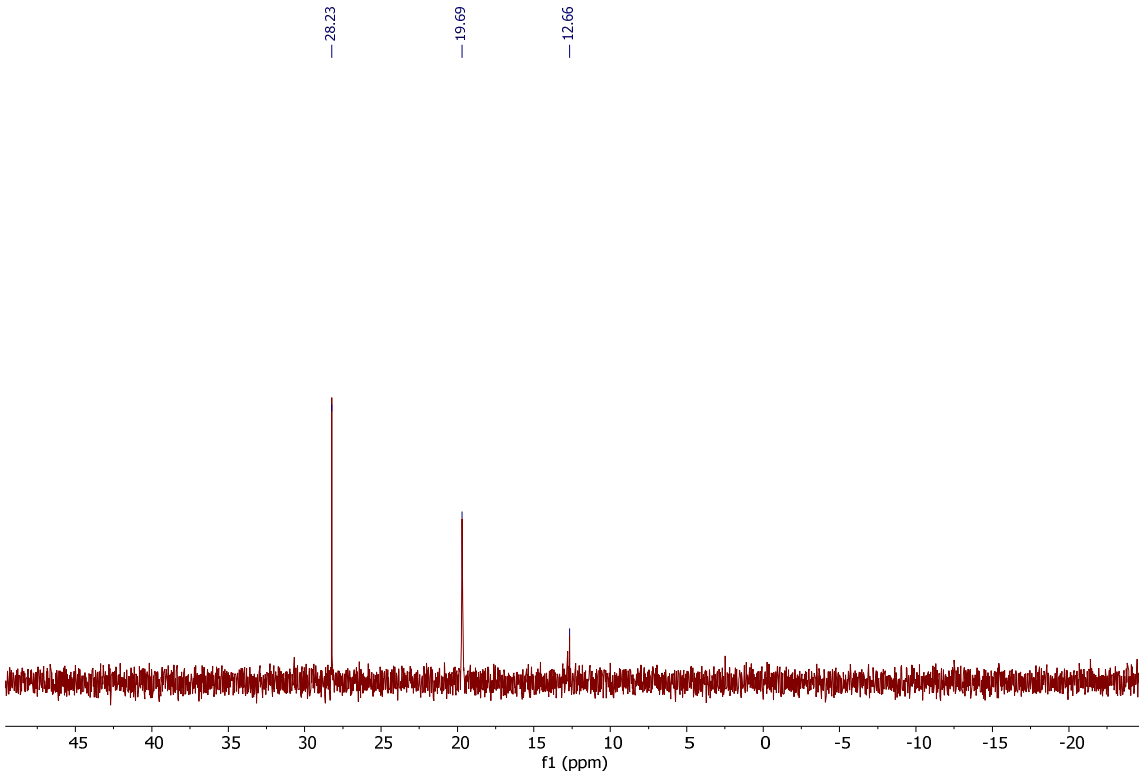

*Figure S 13: ^{31}P NMR (101 MHz, $CDCl_3$) of the reaction mixture of **5** after 1 h reaction time in toluene. (reaction mixture: 1 eq. ethyl isopropyl amine, 1 eq. **3**, 2 eq. TEA)*

Synthesis of 6

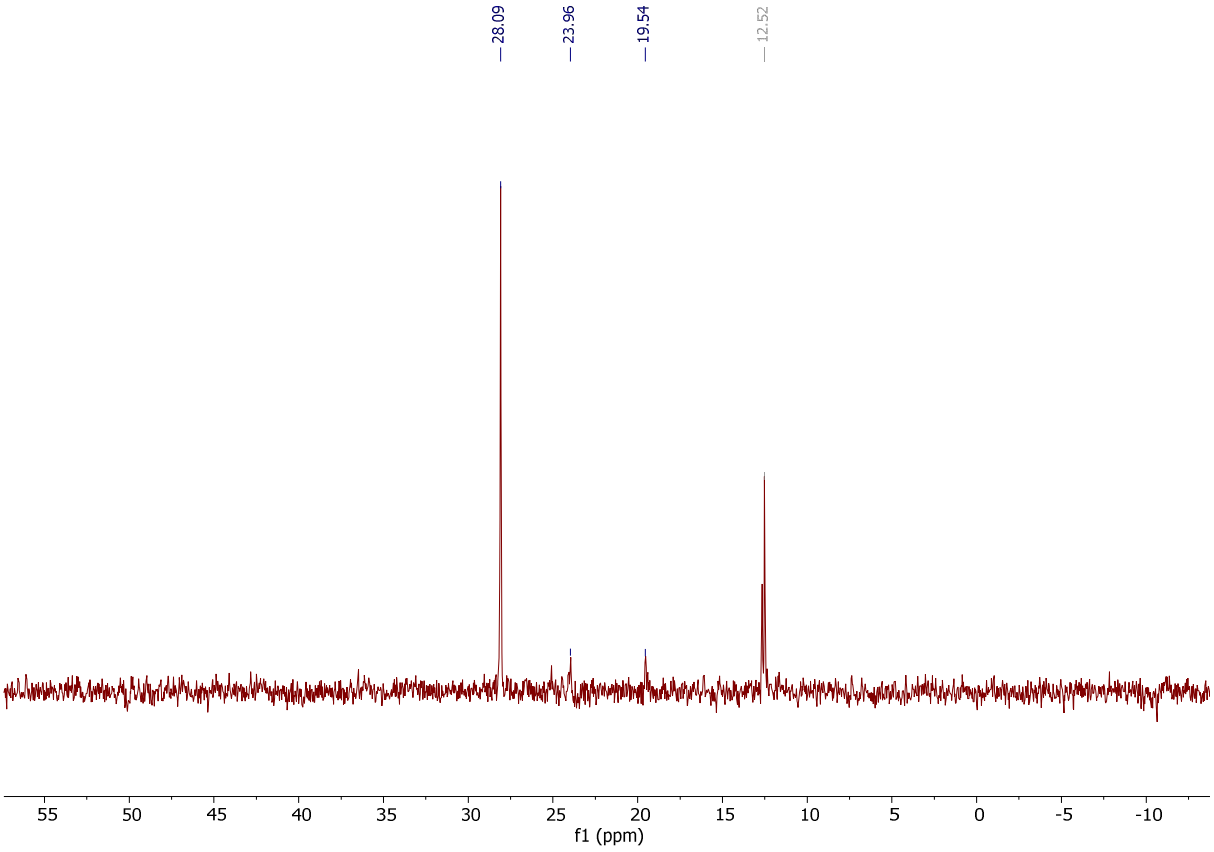

*Figure S 14: ^{31}P NMR (101 MHz, $CDCl_3$) of the reaction mixture of **6** after 1 h reaction time in toluene. (reaction mixture: 1 eq. diisopropyl amine, 1 eq. **3**)*

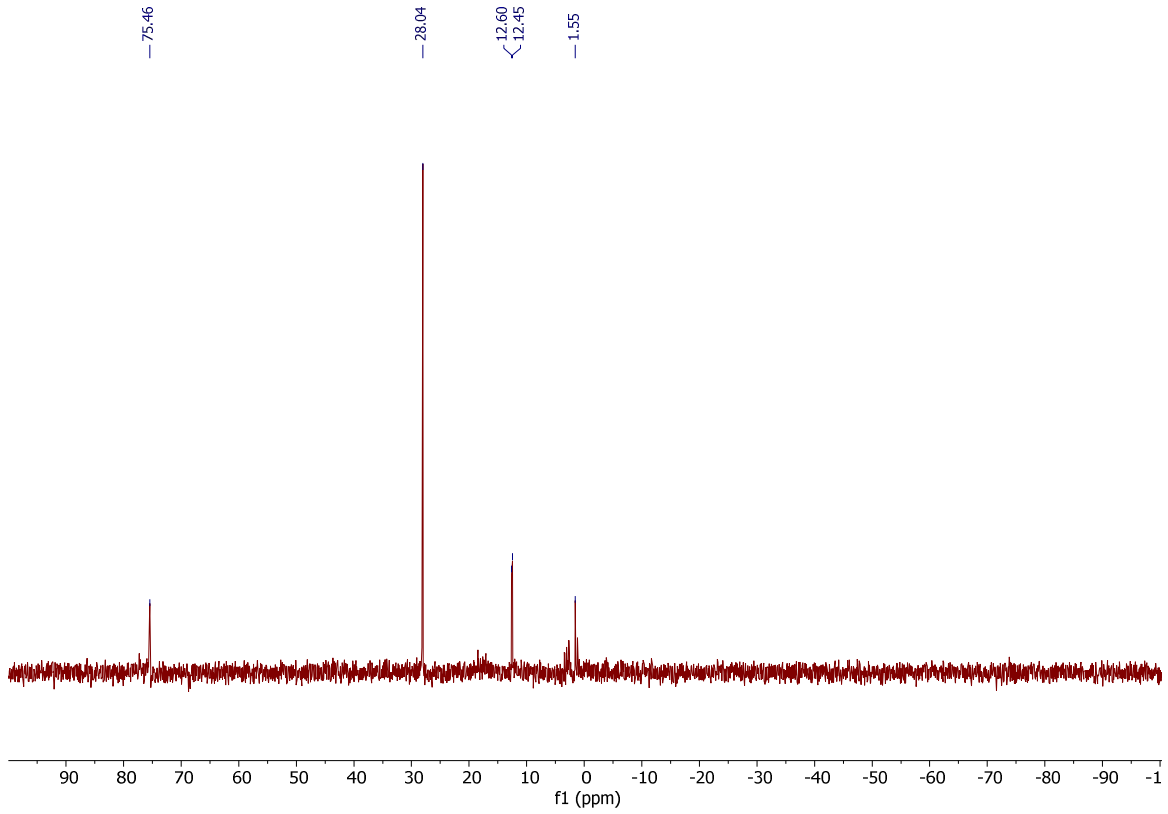

*Figure S 15: ^{31}P NMR (101 MHz, $CDCl_3$) of the reaction mixture of **6** after 20 h reaction time. Reaction mixture: 3 eq diisopropyl amine*

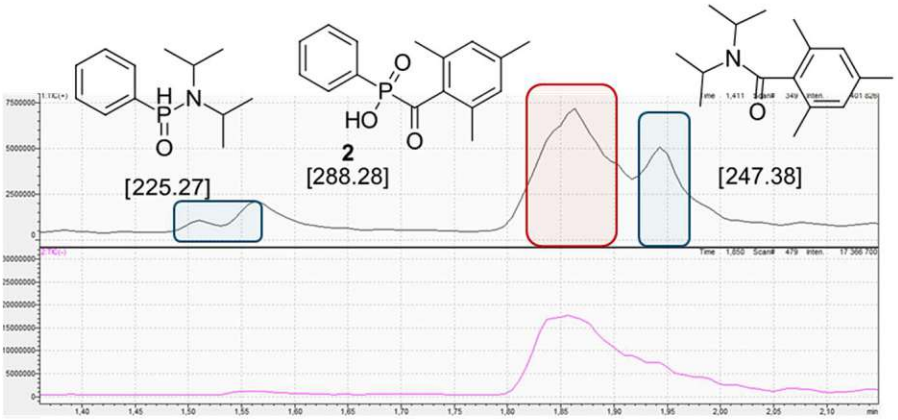

*Figure S 16: UPLC-MS of the reaction mixture **6** **6** after 20 h reaction time. Reaction mixture: 3 eq diisopropyl amine*

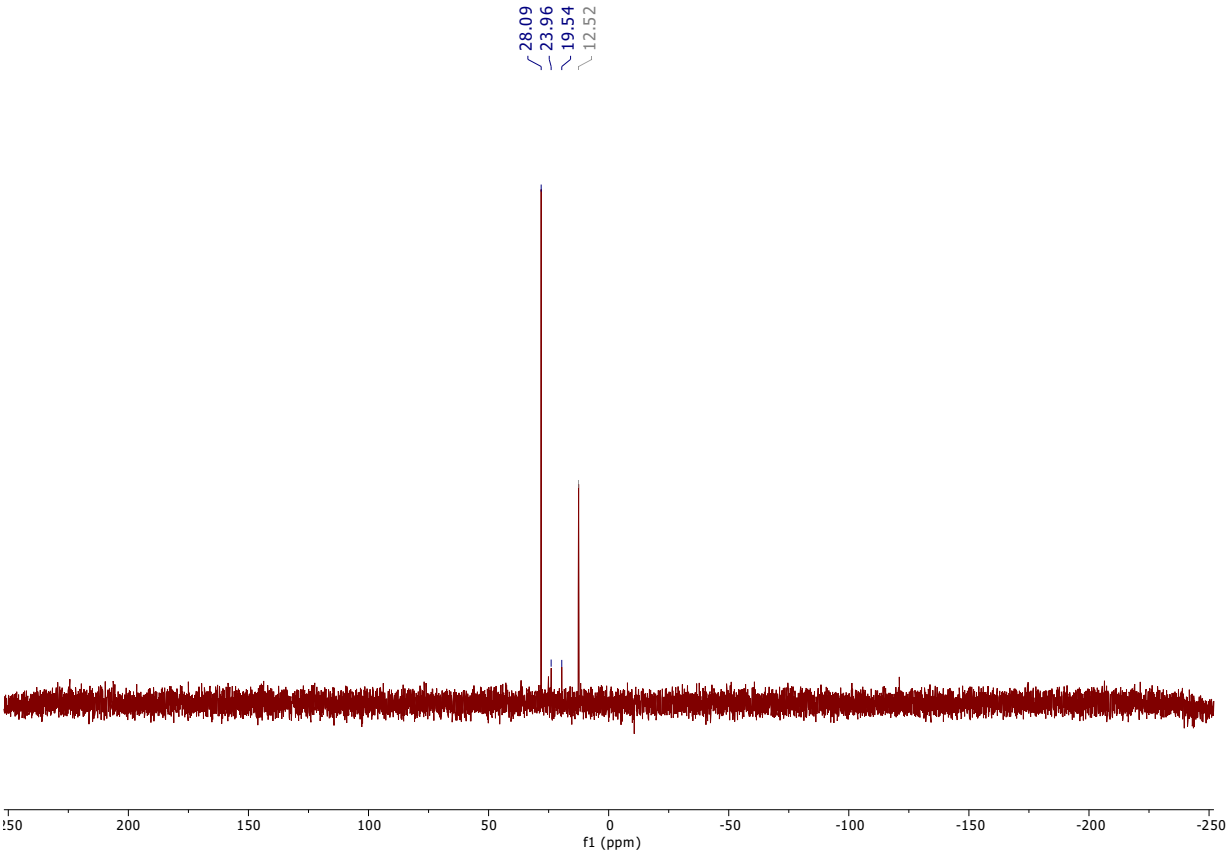

*Figure S 17: ^{31}P NMR (101 MHz, $CDCl_3$) of the reaction mixture of **6** after 3 h of reaction time. Reaction mixture: 1 eq. diisopropyl amine, 2 eq TEA, 1 eq. **3***

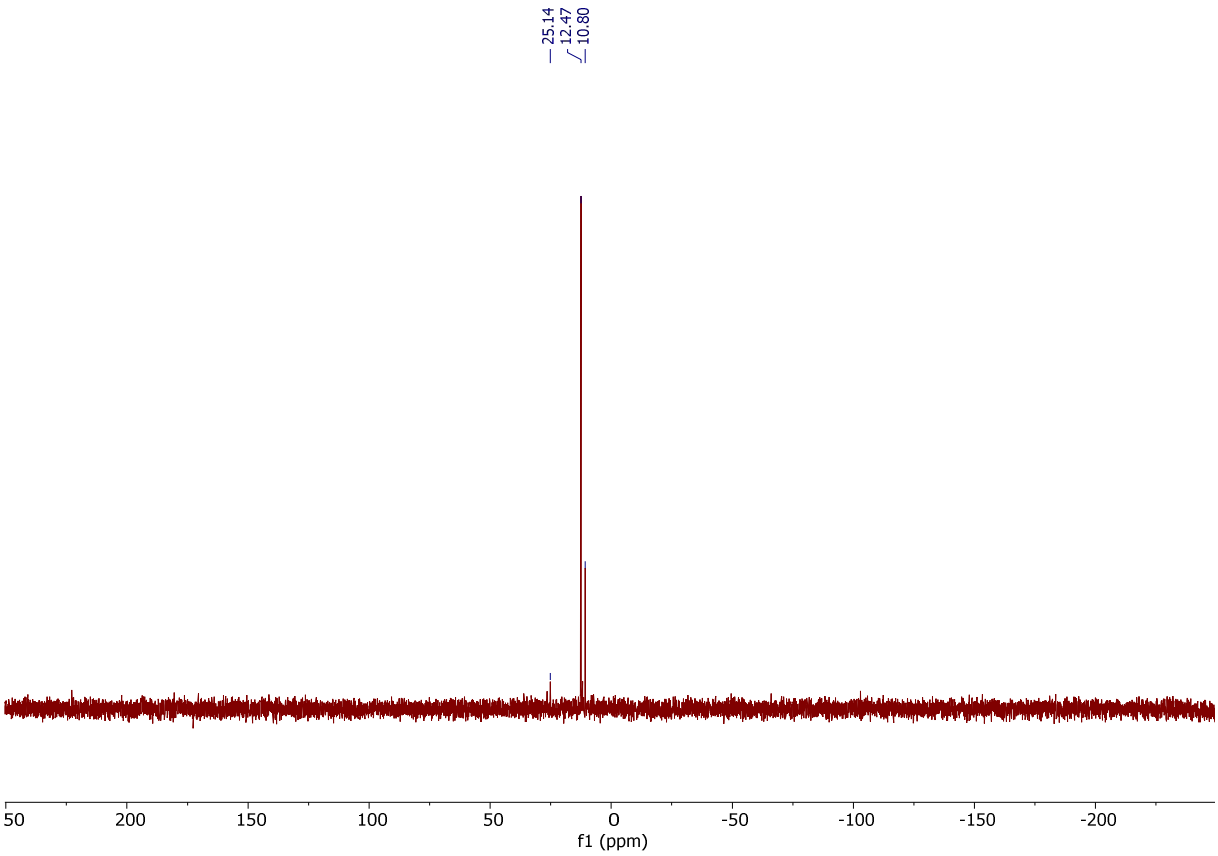

*Figure S 18: ^{31}P NMR (101 MHz, $CDCl_3$) of the reaction mixture of **6** after 18 h of reaction time. Reaction mixture: 1 eq. diisopropyl amine, 2 eq TEA, 1 eq. **3***

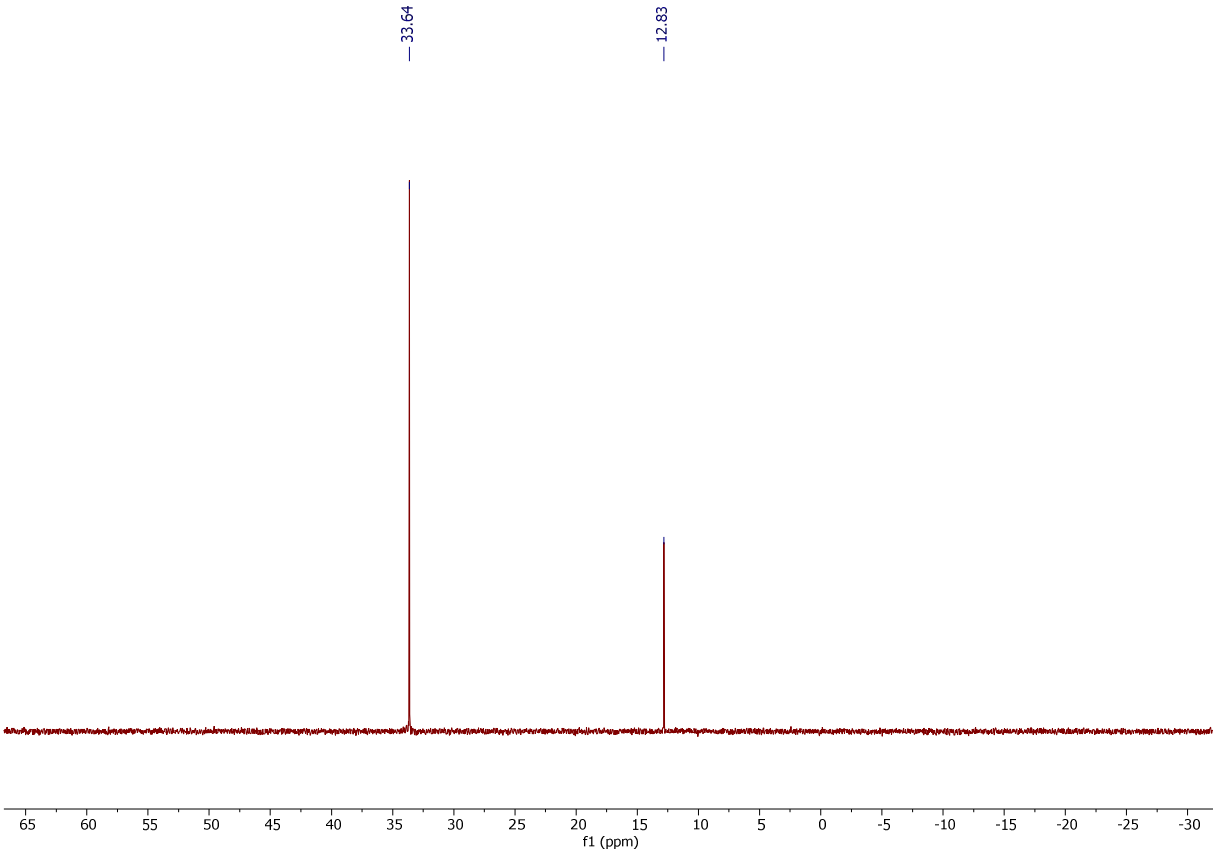

*Figure S 19: ^{31}P NMR (101 MHz, $CDCl_3$) of the reaction mixture **7** directly after thiophenol was added (0 min)*

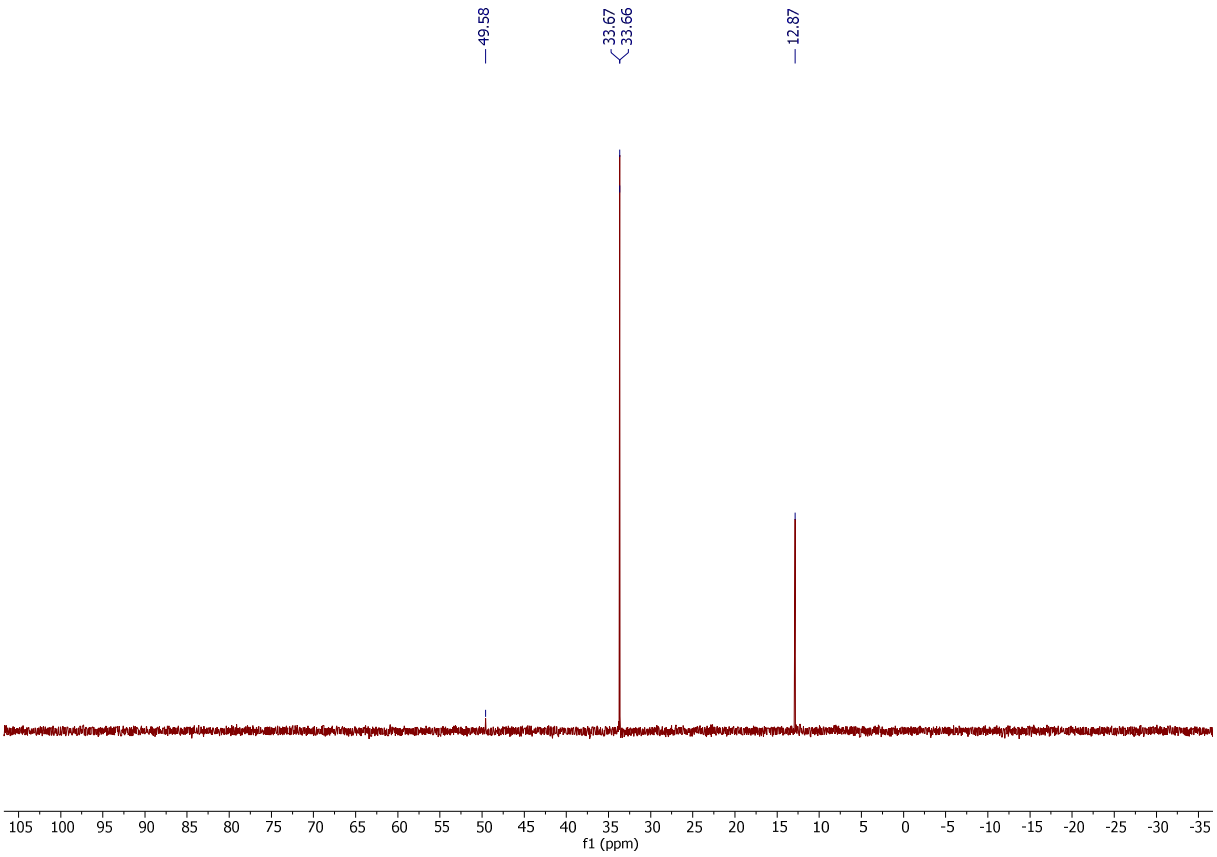

*Figure S 20: ^{31}P NMR (101 MHz, $CDCl_3$) of the reaction mixture **7** after 2 min of stirring.*

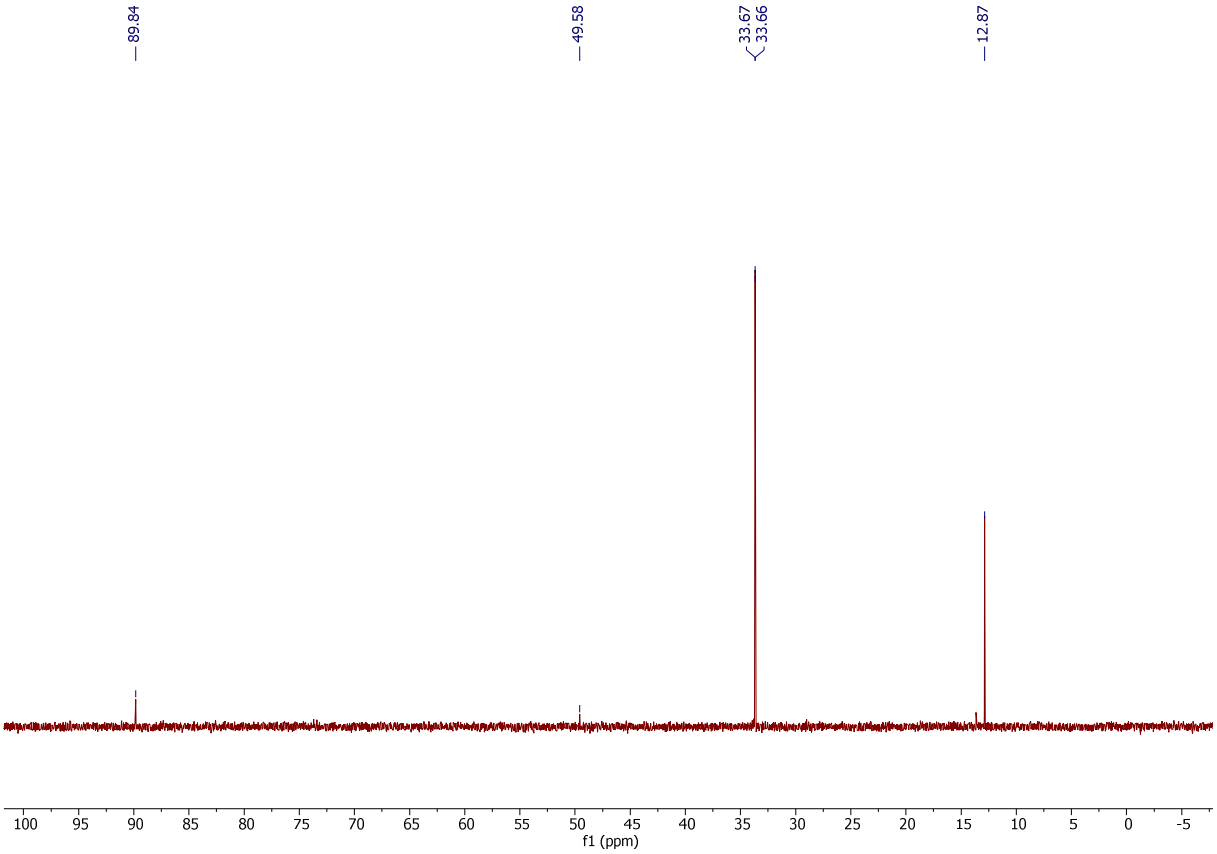

*Figure S 21: ^{31}P NMR (101 MHz, $CDCl_3$) of the reaction mixture **7** after 15 min of stirring.*

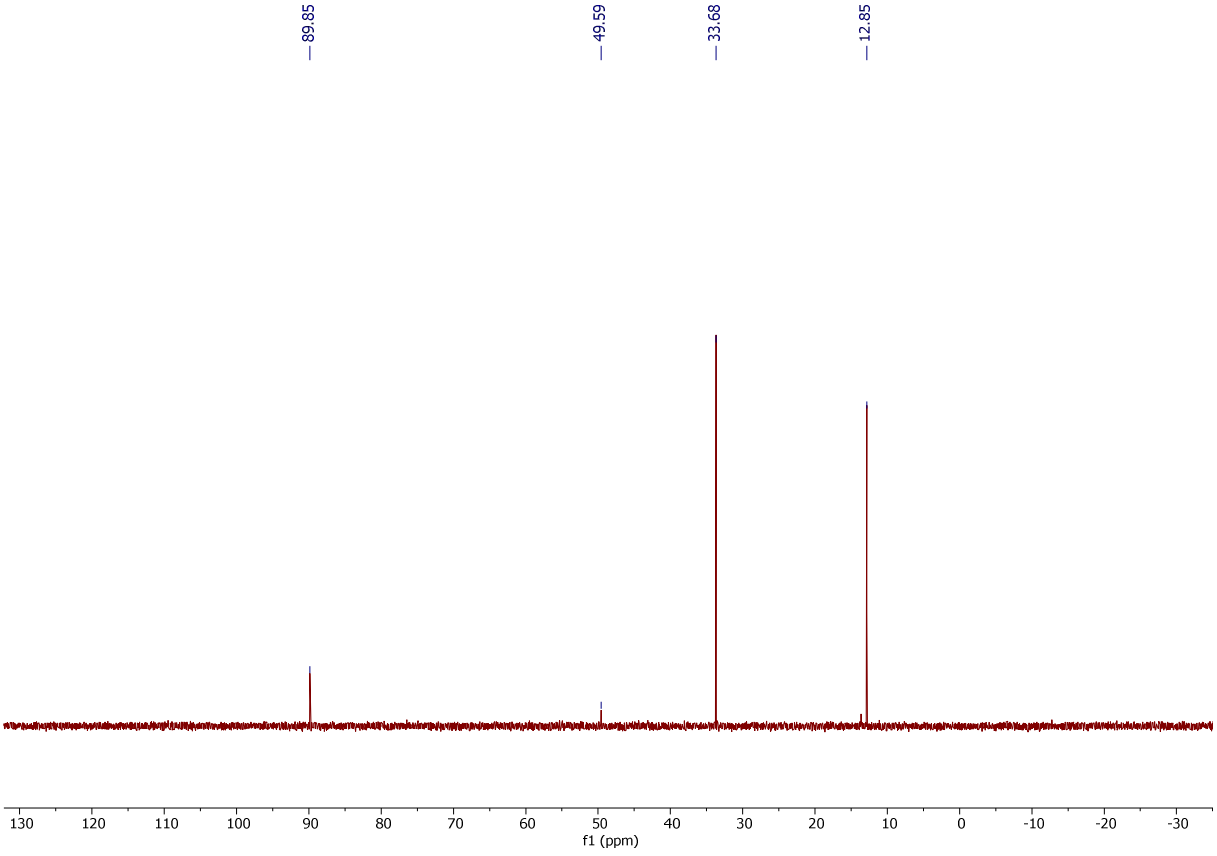

*Figure S 22: ^{31}P NMR (101 MHz, $CDCl_3$) of the reaction mixture **7** after 30 min of stirring.*

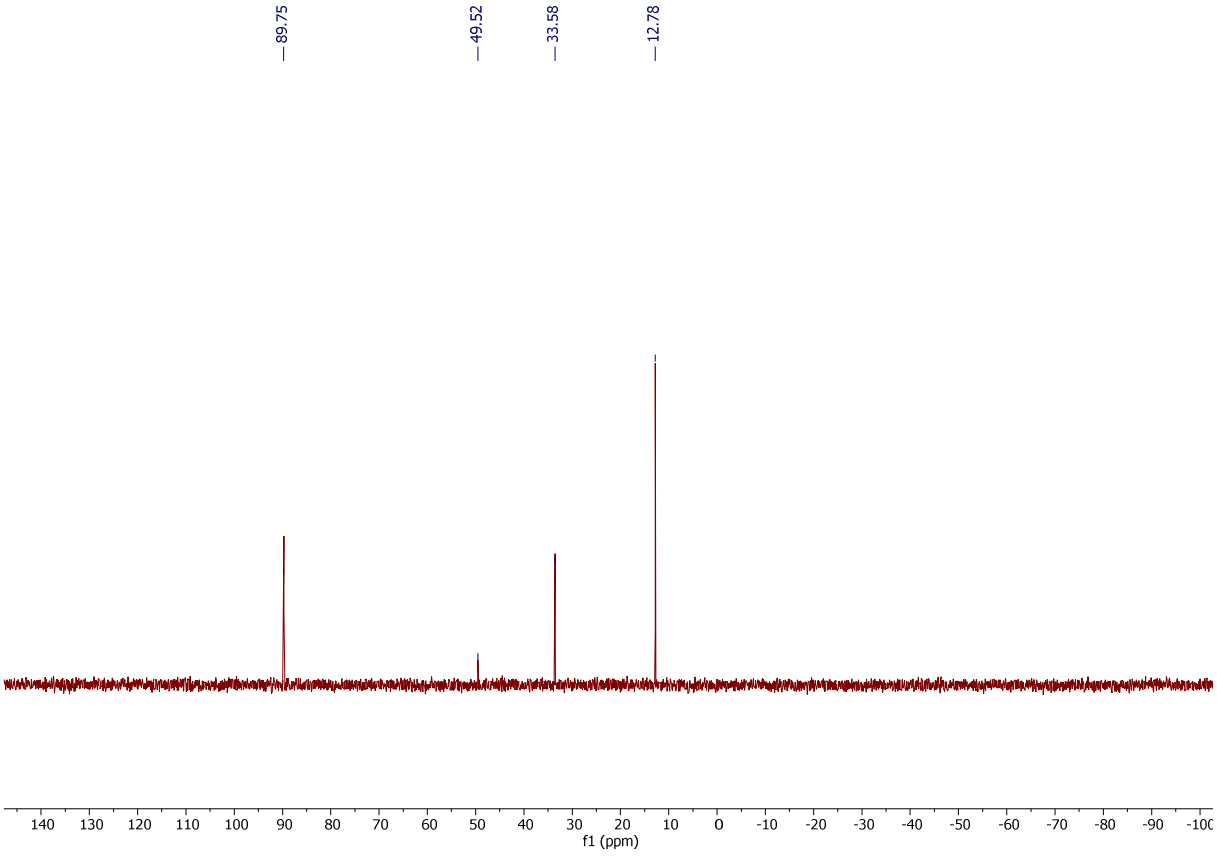

*Figure S 23: ^{31}P NMR (101 MHz, $CDCl_3$) of the reaction mixture **7** after 1 h of stirring.*

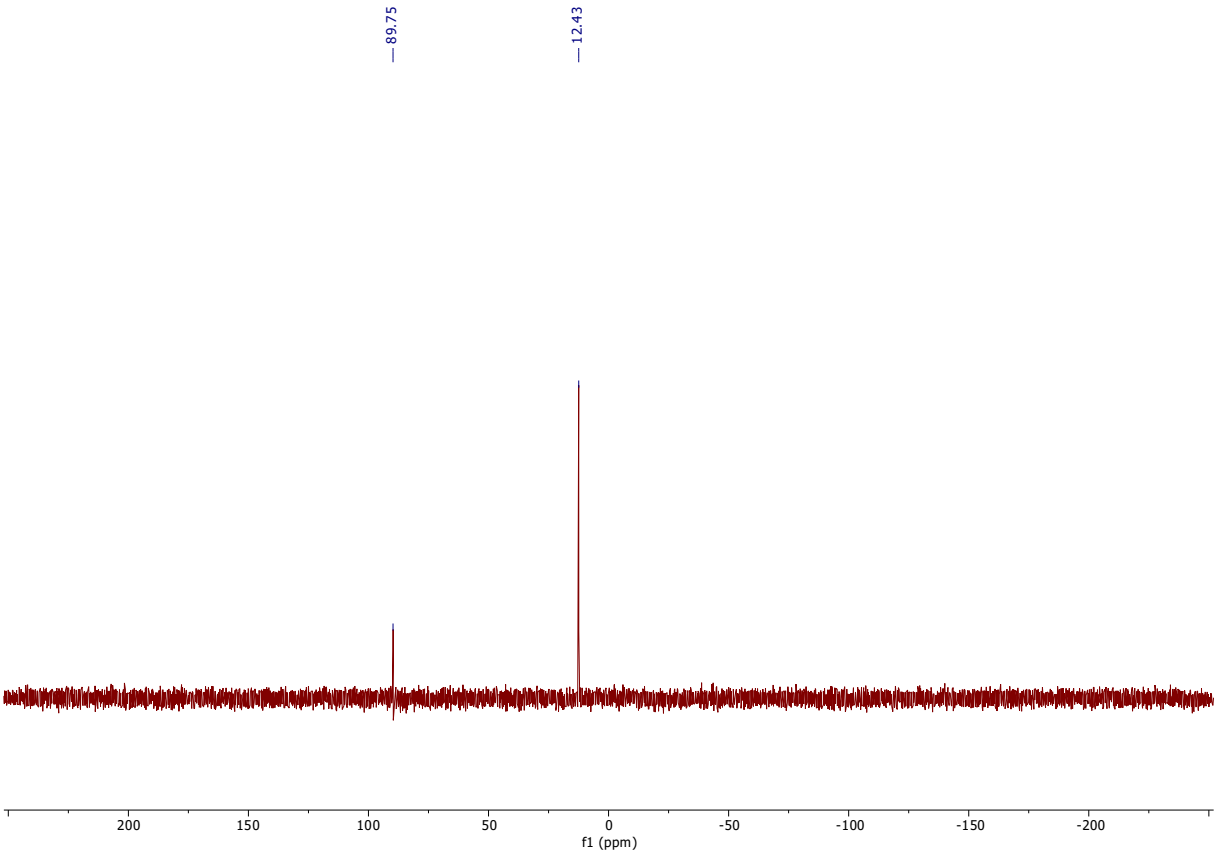

*Figure S 24: ^{31}P NMR (101 MHz, $CDCl_3$) of the product **7** after purification step*

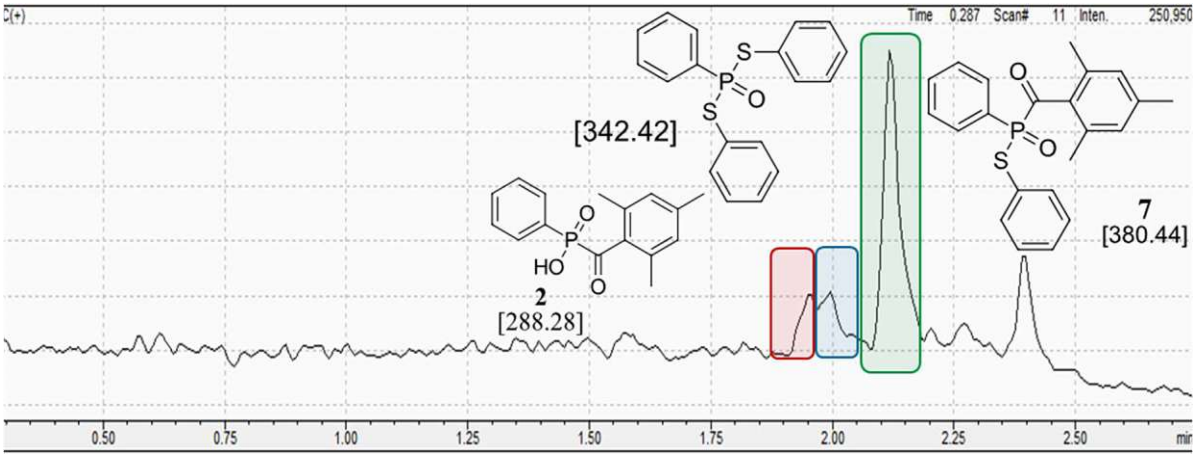

*Figure S 25: UPLC-MS analysis of the crude reaction mixture **7**.*

Synthesis of 8

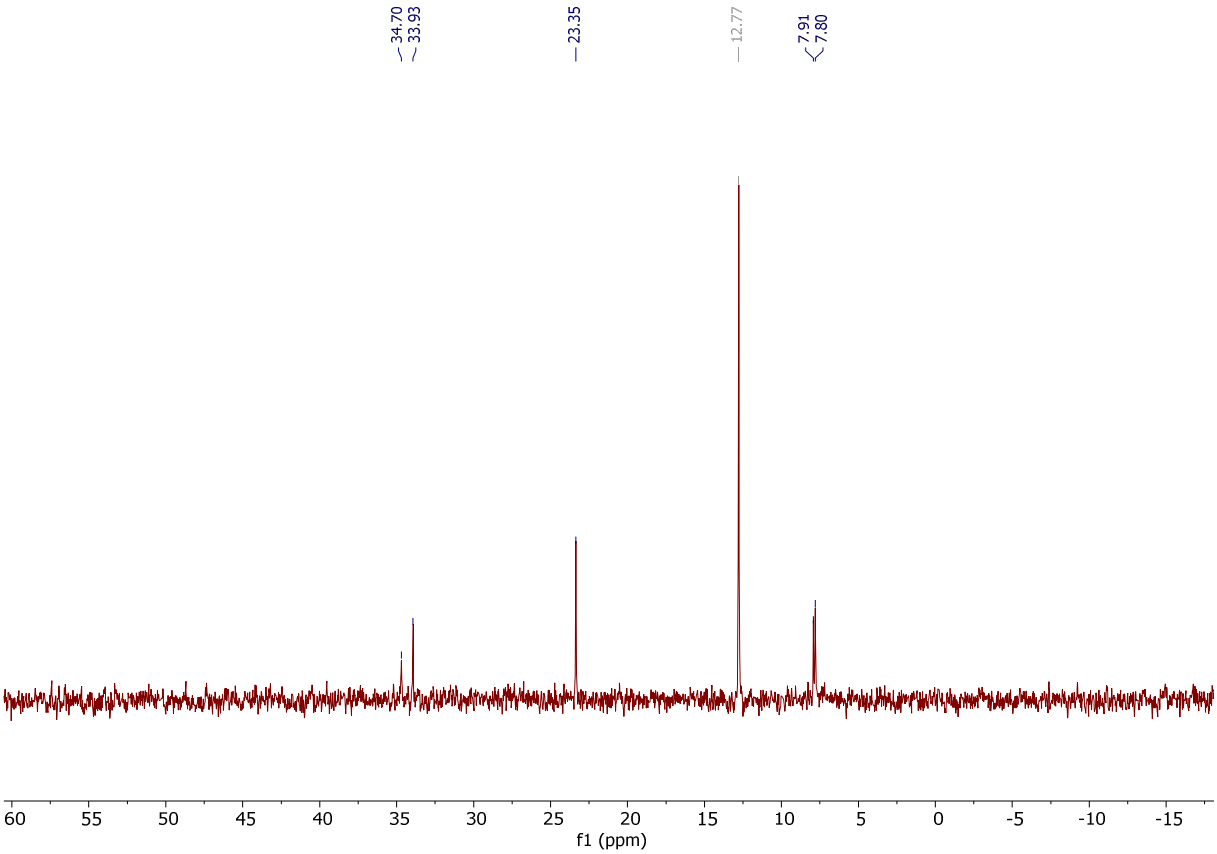

*Figure S 26: ^{31}P NMR (101 MHz, $CDCl_3$) of the reaction mixture of **8** after 1 h of reaction time*

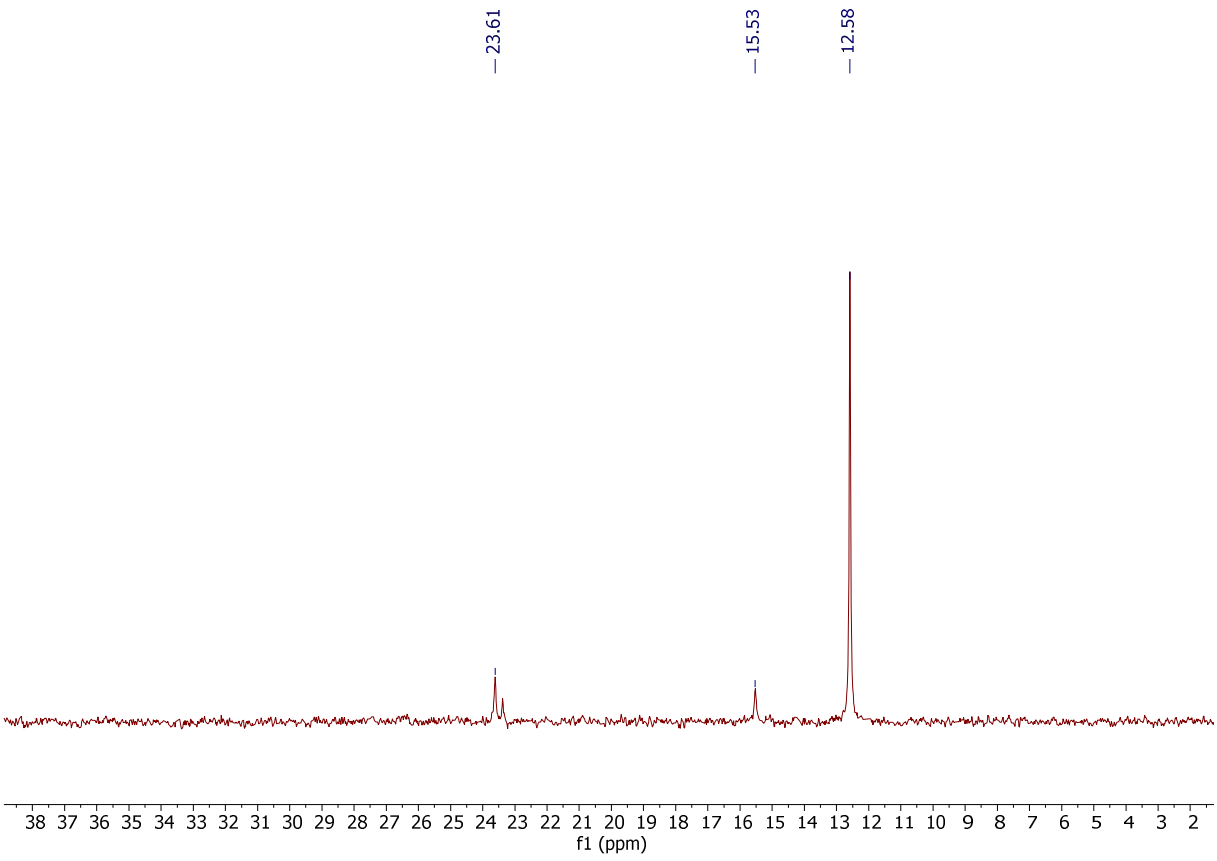

*Figure S 27: ^{31}P NMR (101 MHz, $CDCl_3$) of the reaction mixture of **8** after 7 days*

Synthesis of 9

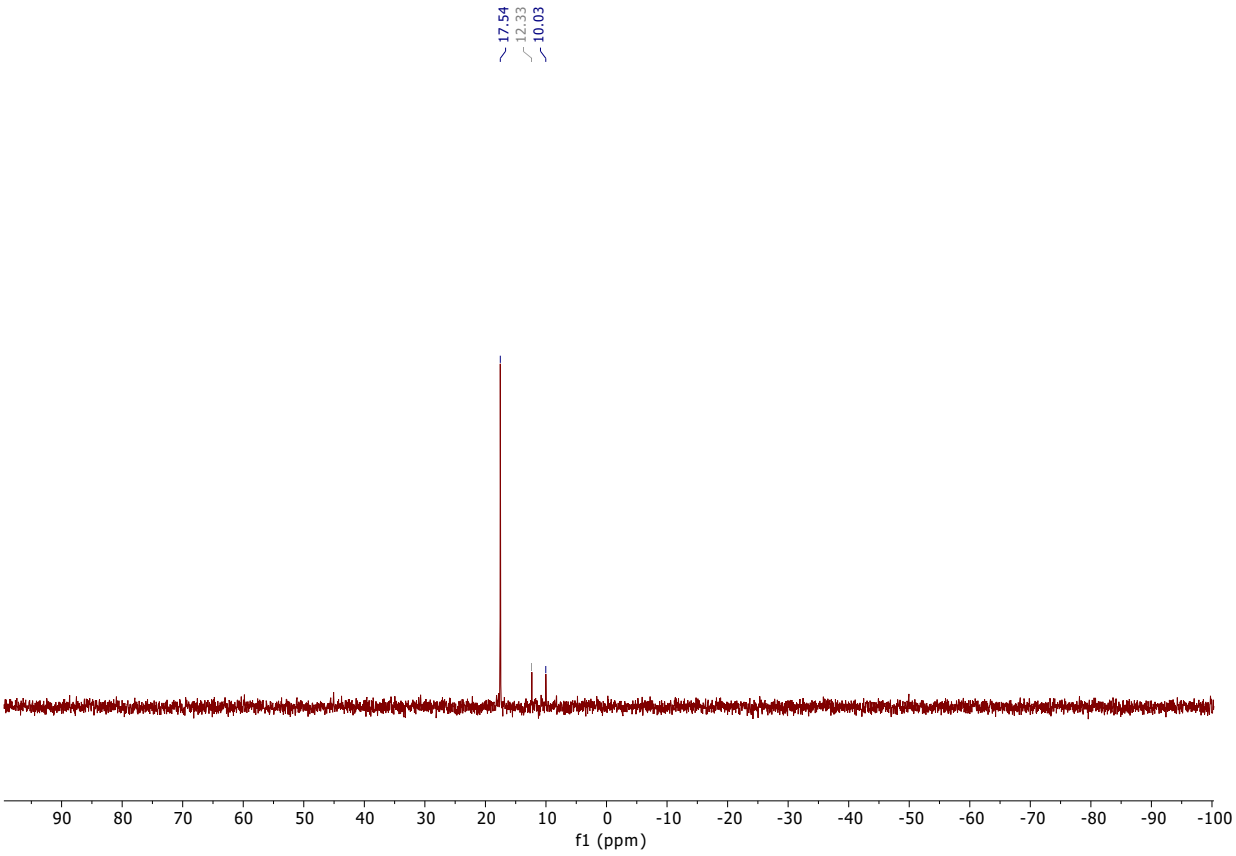

*Figure S 28: ^{31}P NMR (101 MHz, $CDCl_3$) of the reaction mixture **9** using standard synthesis procedure*

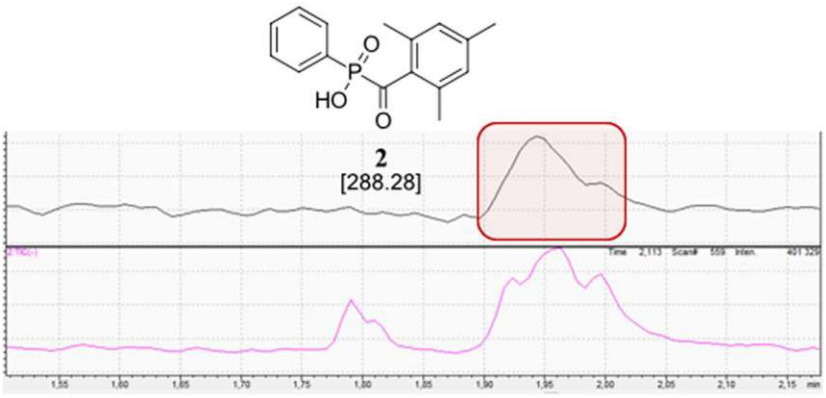

*Figure S 29: UPLC-MS of the reaction mixture **9** using general synthesis procedure*

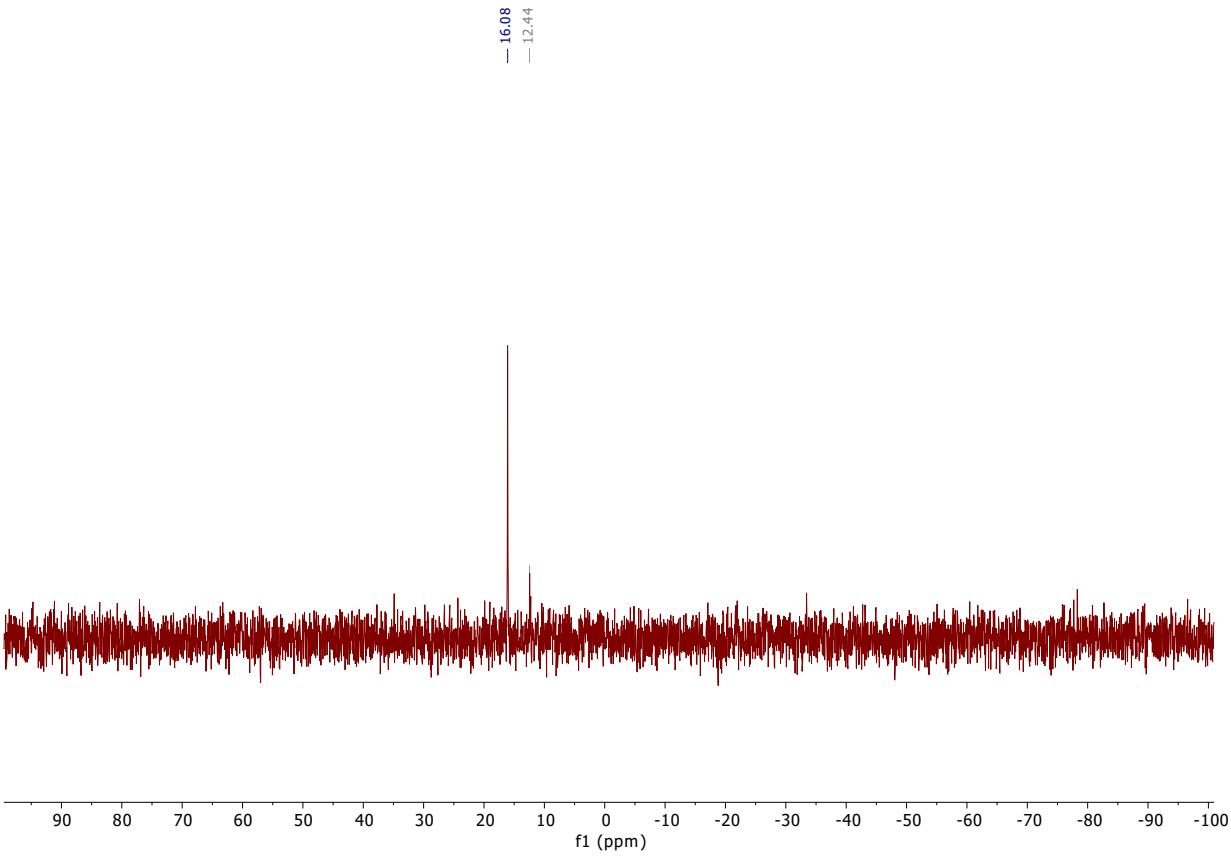

*Figure S 30: ^{31}P NMR (101 MHz, $CDCl_3$) of the reaction mixture of **9** using DCC synthesis procedure*

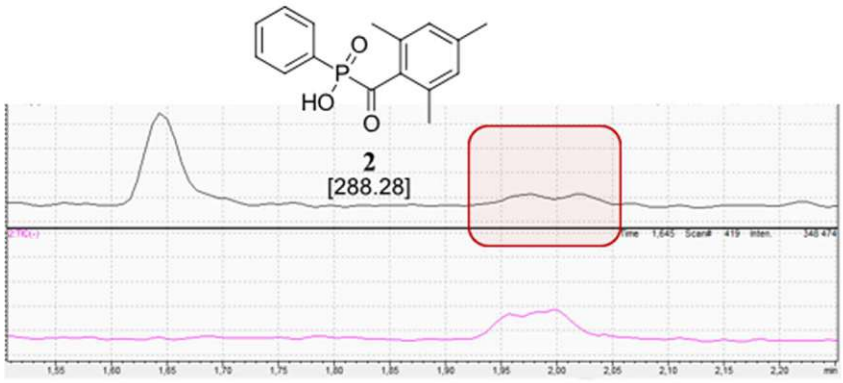

*Figure S 31: UPLC-MS of the reaction mixture **9** using DCC synthesis procedure*

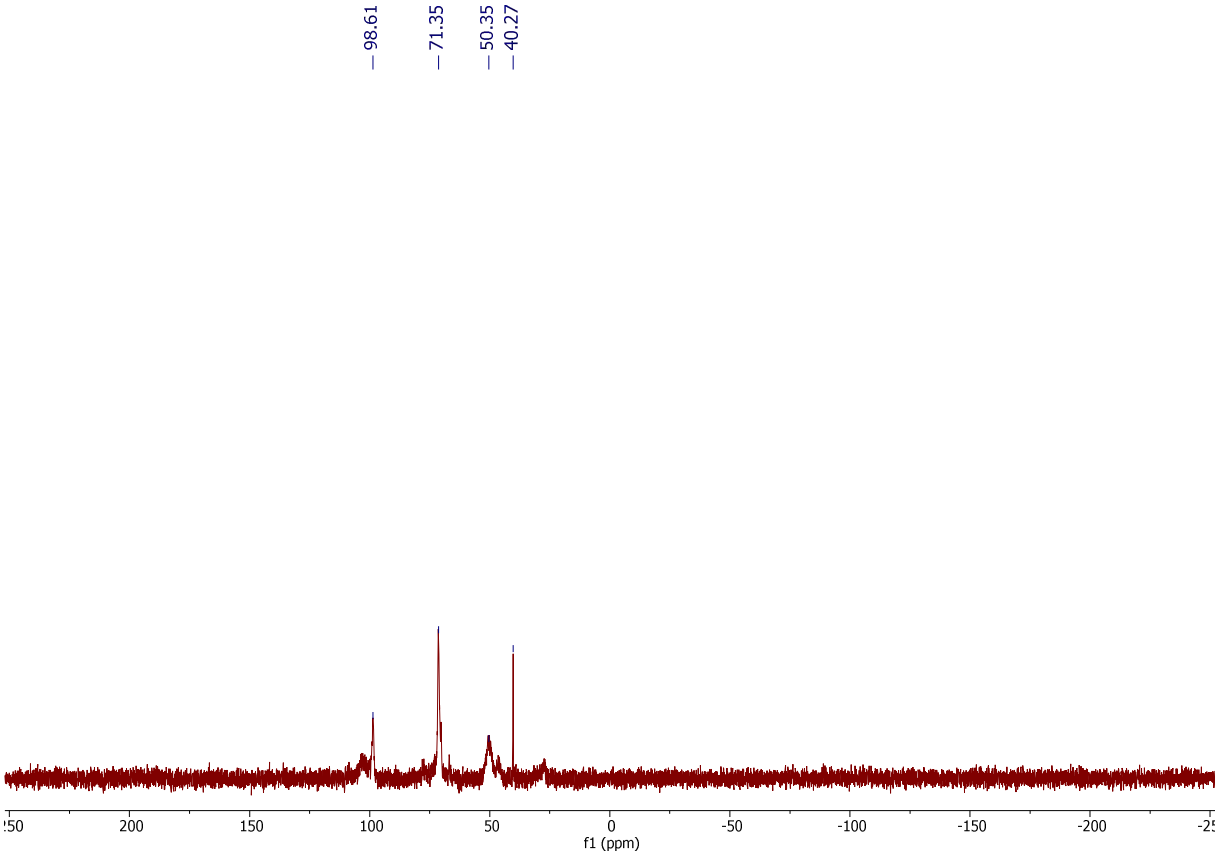

*Figure S 32: ^{31}P NMR (101 MHz, $CDCl_3$) of crude reaction mixture **10** before **3** was added.*

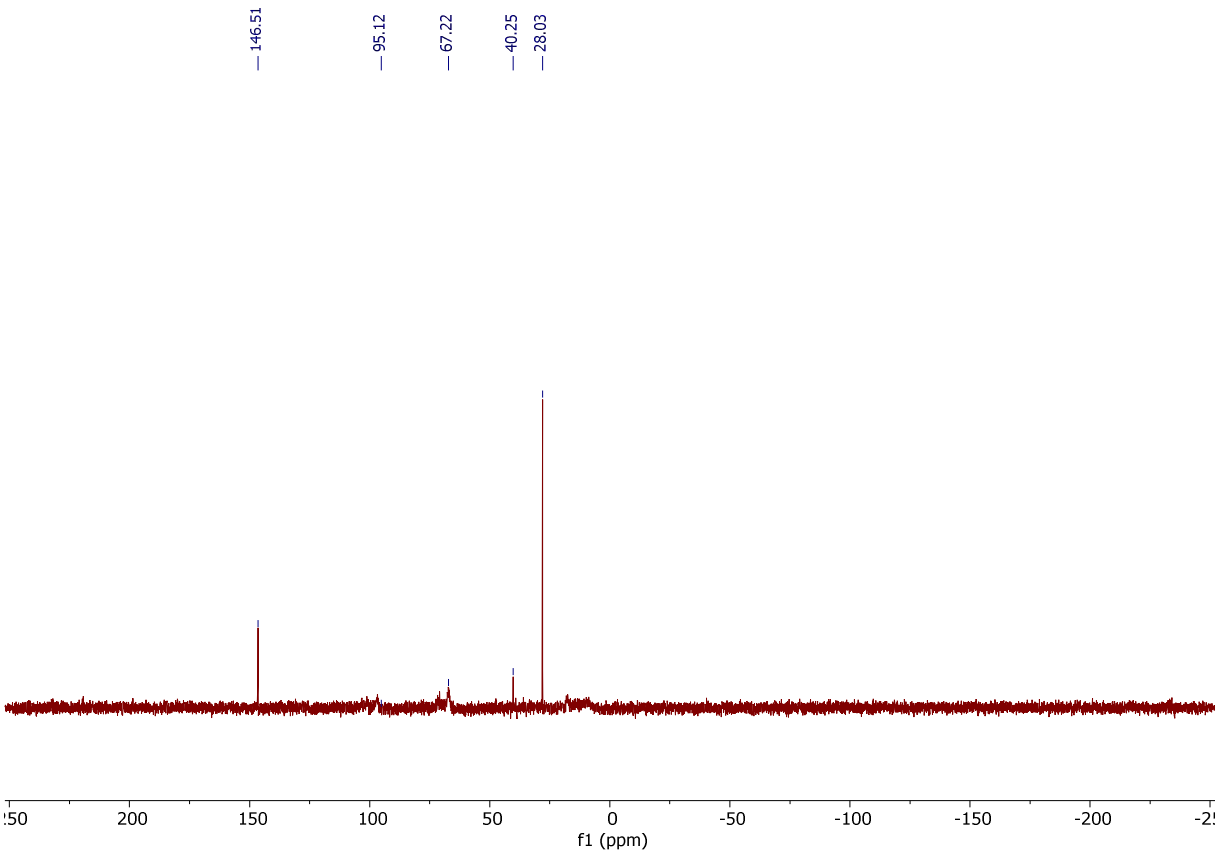

*Figure S 33: ^{31}P NMR (101 MHz, $CDCl_3$) of the reaction mixture **10** after the addition of **3***

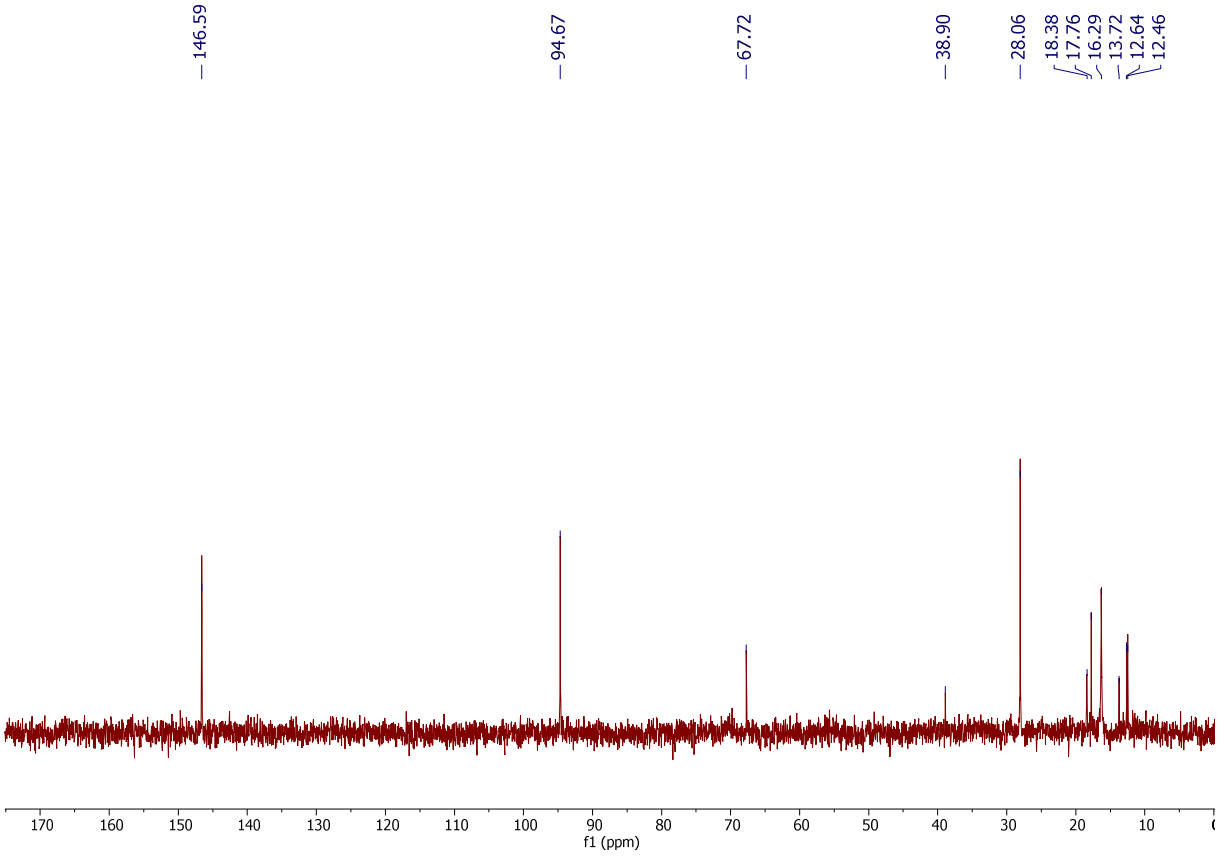

*Figure S 34: ^{31}P NMR (101 MHz, $CDCl_3$) of the reaction mixture **10** using lithium naphthalin approach.*

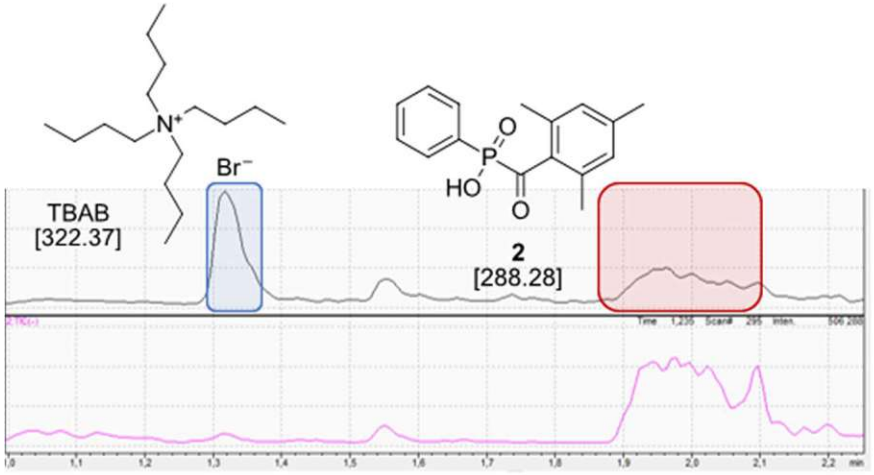

*Figure S 35: UPLC-MS measurement of reaction mixture **11 and 12** after 30 min of reaction time.*

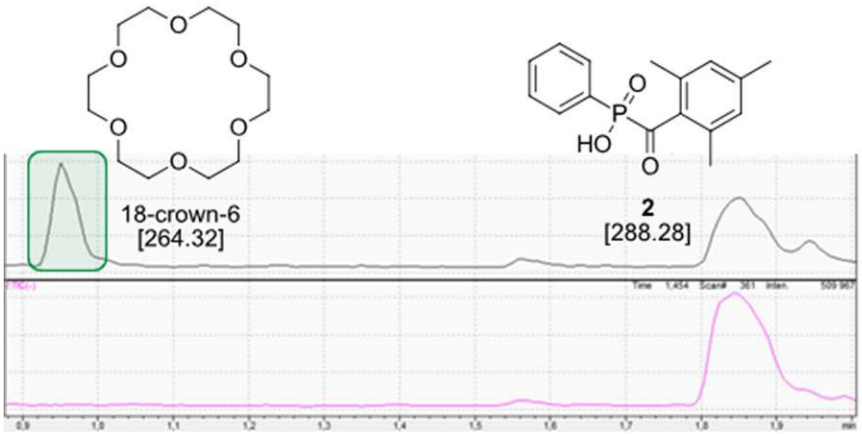

*Figure S 36: UPLC-MS measurement of reaction mixture **11** after 30 min of reaction time.*

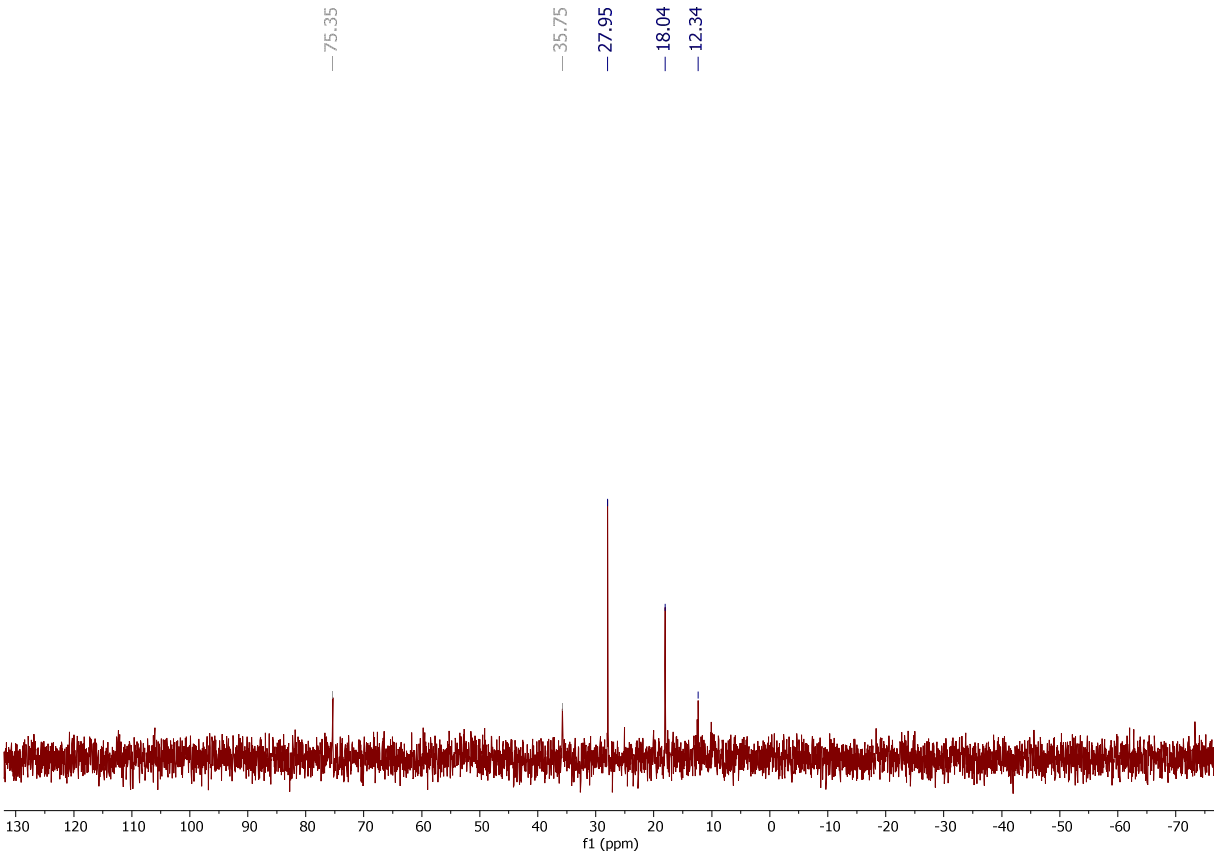

*Figure S 37: ^{31}P NMR (101 MHz, $CDCl_3$) of the reaction mixture **11** using 18-crown-6 approach after 30 min of reaction time*

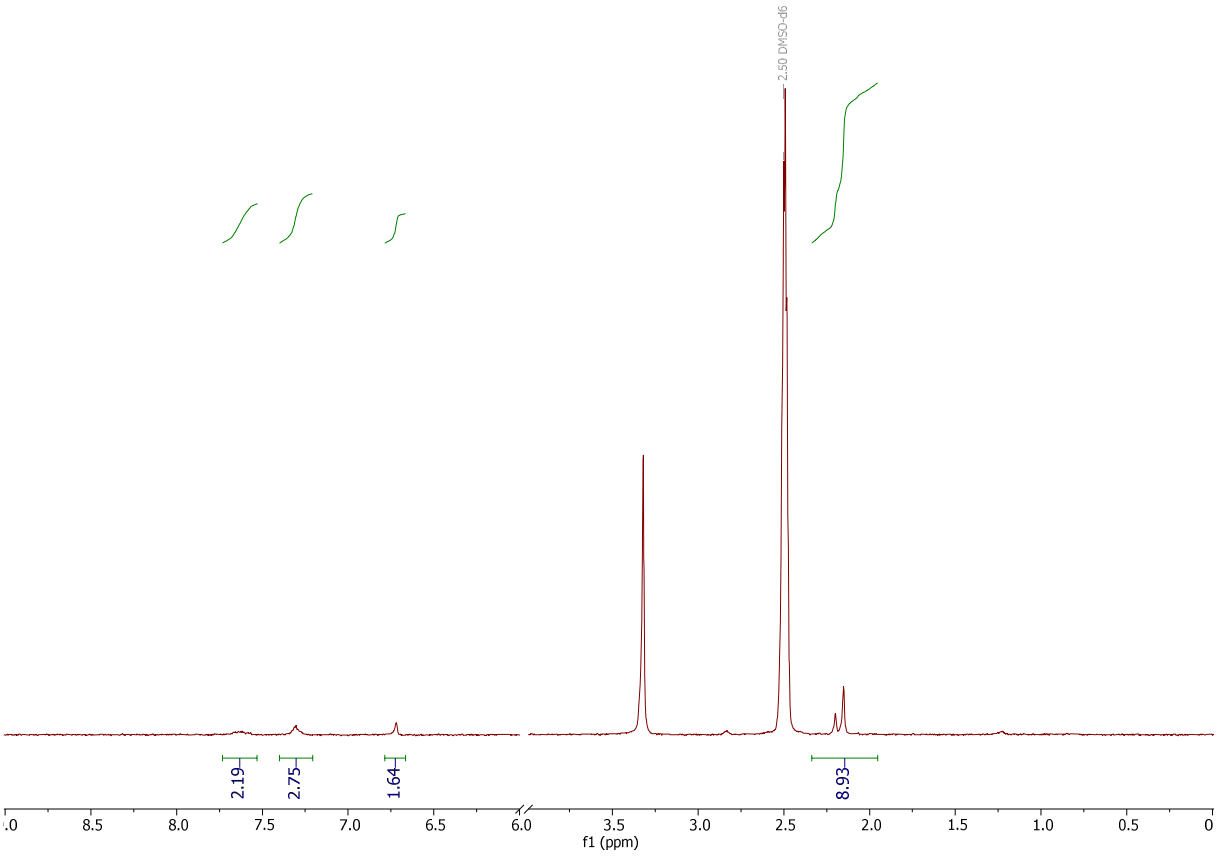

*Figure S 38: ^{1}H NMR (200 MHz, DMSO) of reaction mixture **11** using NaCN in ACN approach after 1 h of reaction time. The same results were obtained with NaSCN in ACN.*

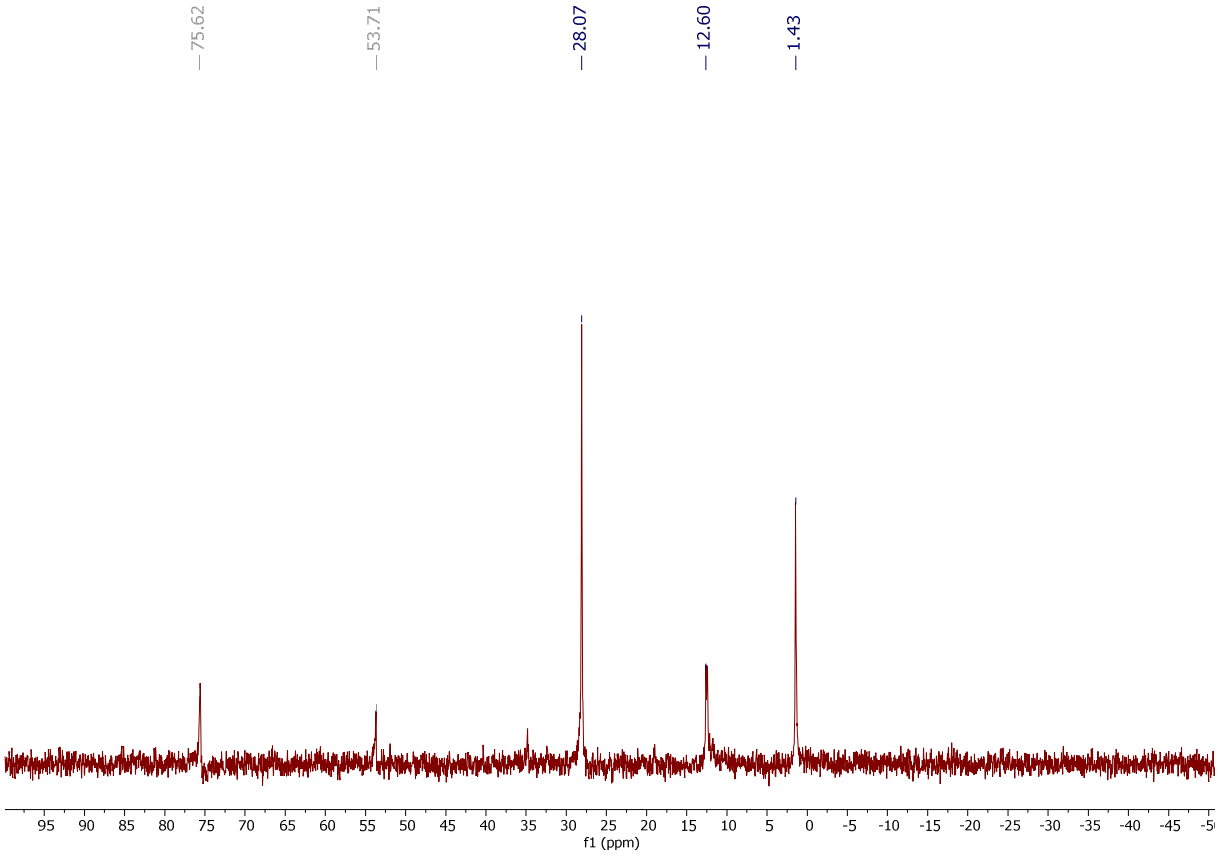

*Figure S 39: ^{31}P NMR (101 MHz, $CDCl_3$) of the reaction mixture **12** using KSCN in ACN approach after 4 h of reaction time*

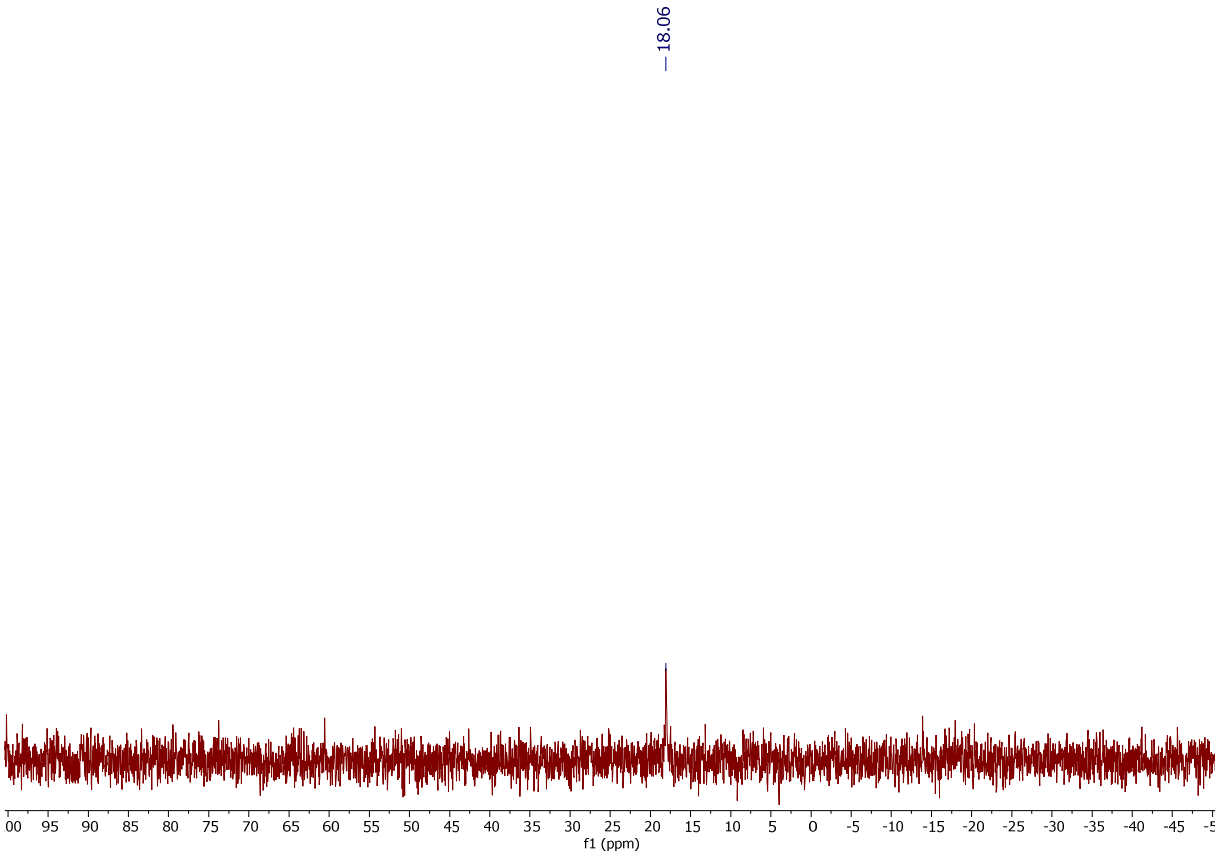

*Figure S 40: ^{31}P NMR (101 MHz, $CDCl_3$) of the reaction mixture **12** using KSCN in ACN approach after 14 days.*

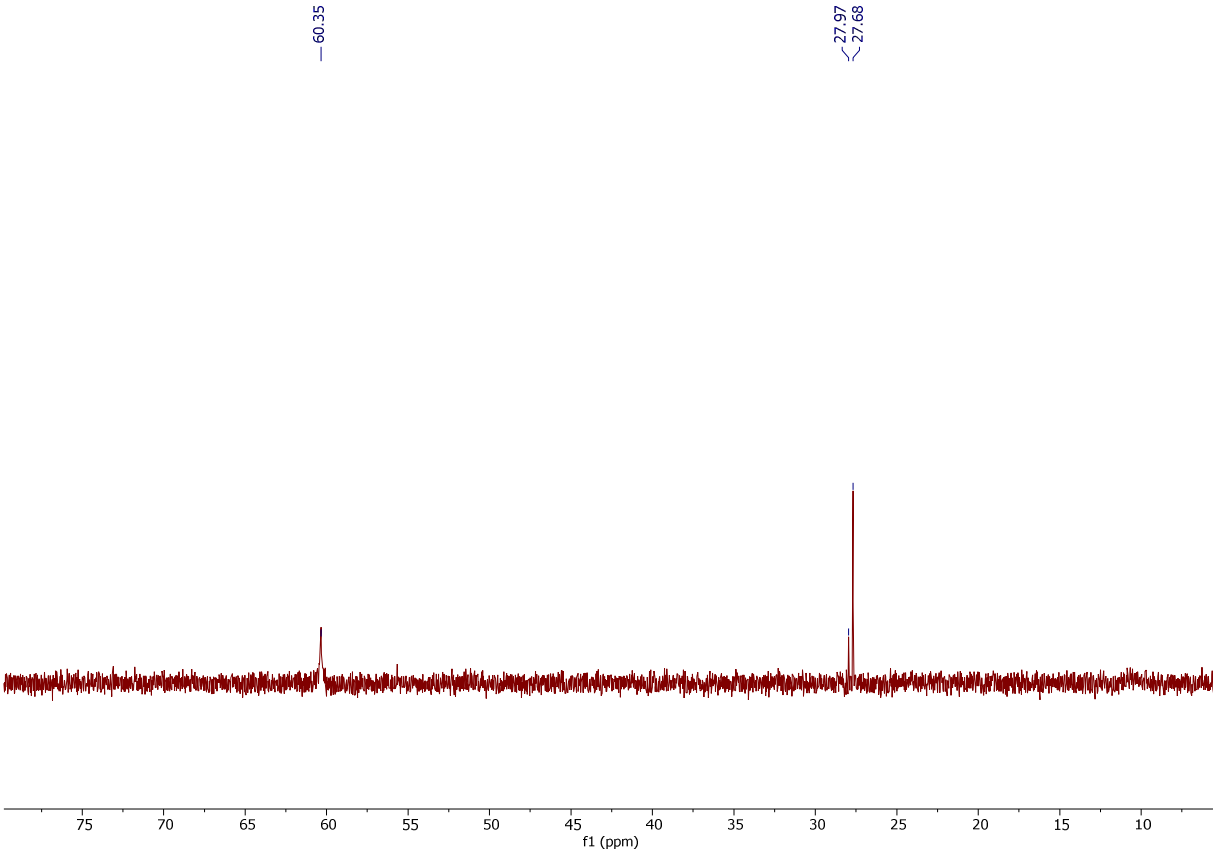

*Figure S 41: ^{31}P NMR (101 MHz, $CDCl_3$) of potassium salt intermediate for **13***

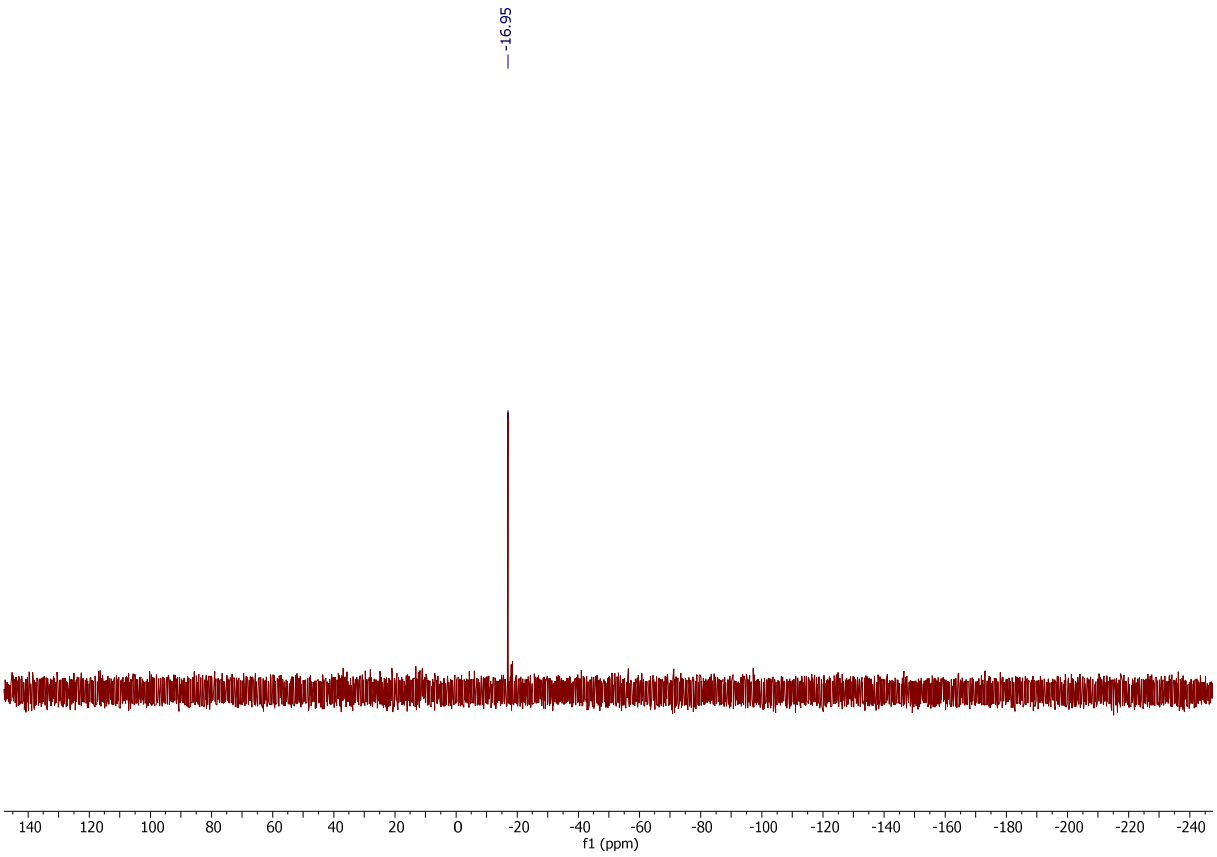

*Figure S 42: ^{31}P NMR (101 MHz, $CDCl_3$) of **13***

Synthesis of 14

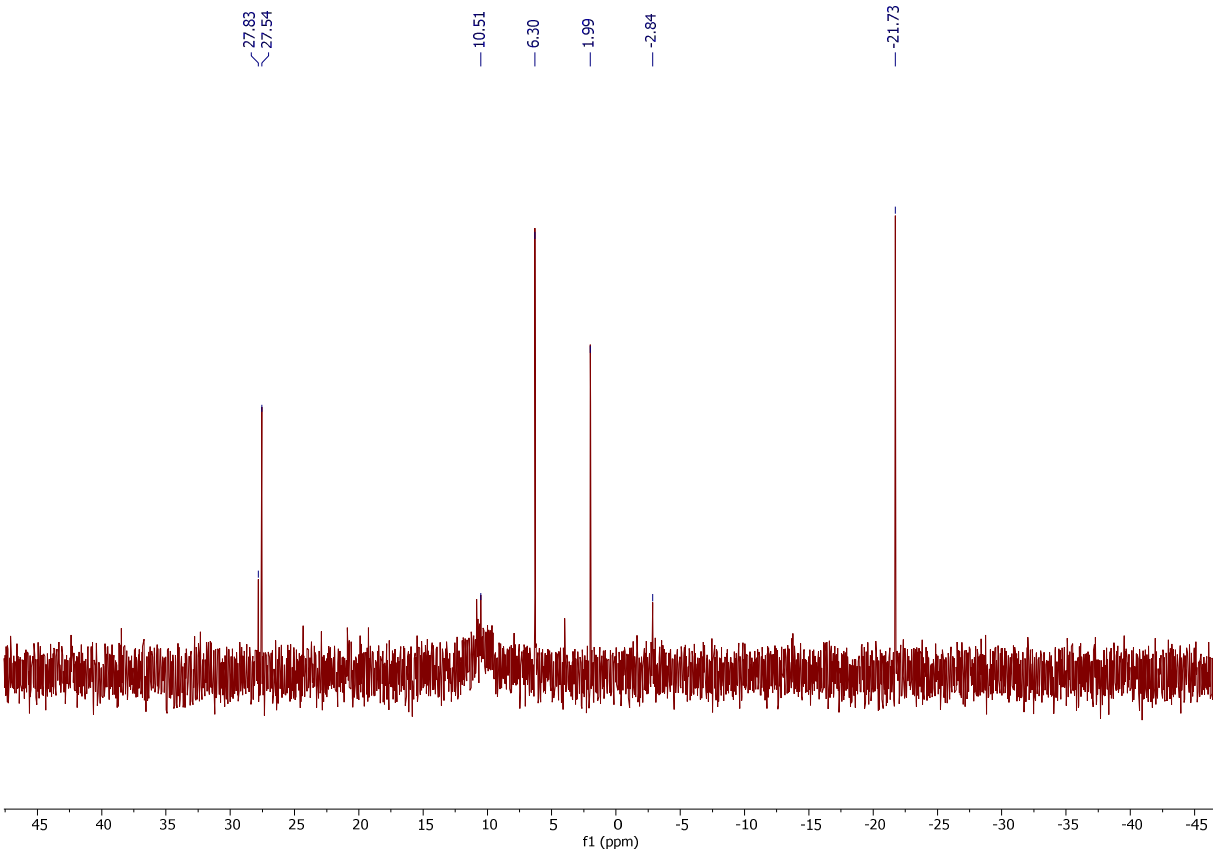

*Figure S 43: ^{31}P NMR (101 MHz, $CDCl_3$) of **14***

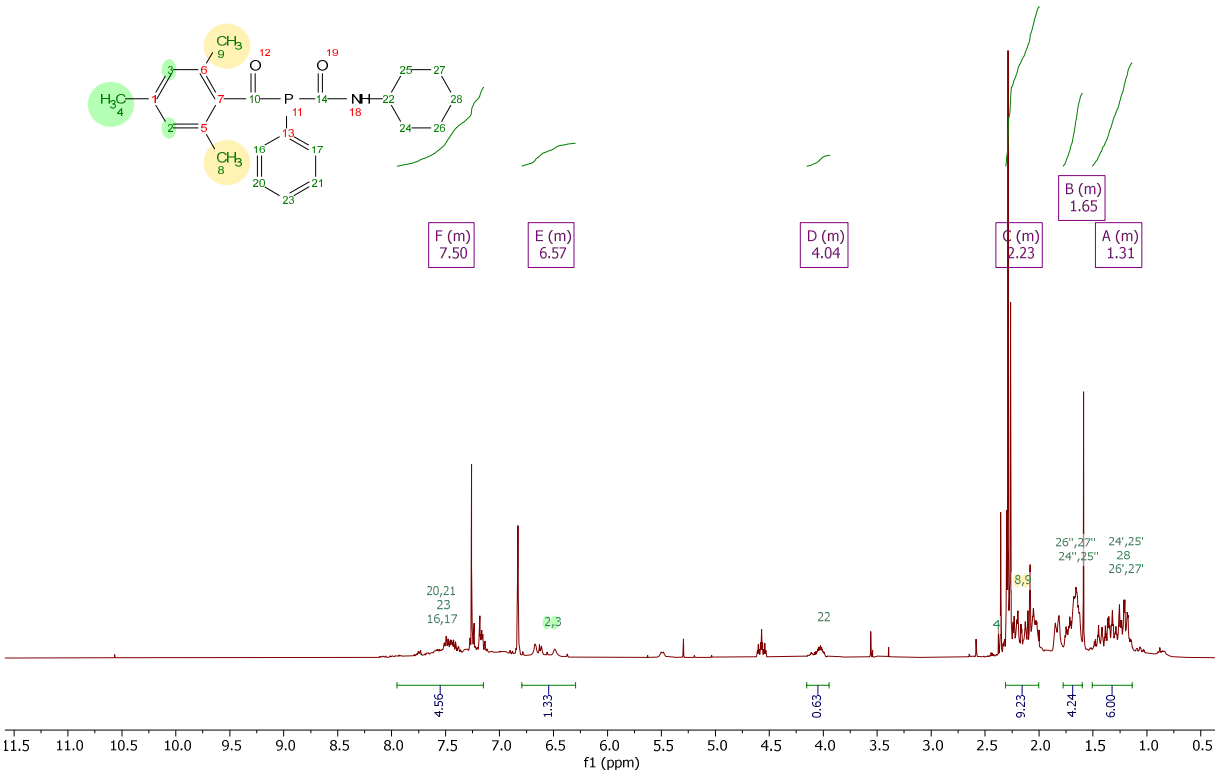

*Figure S 44: ^{1}H NMR (400 MHz, $CDCl_3$) of the crude product **14**.*

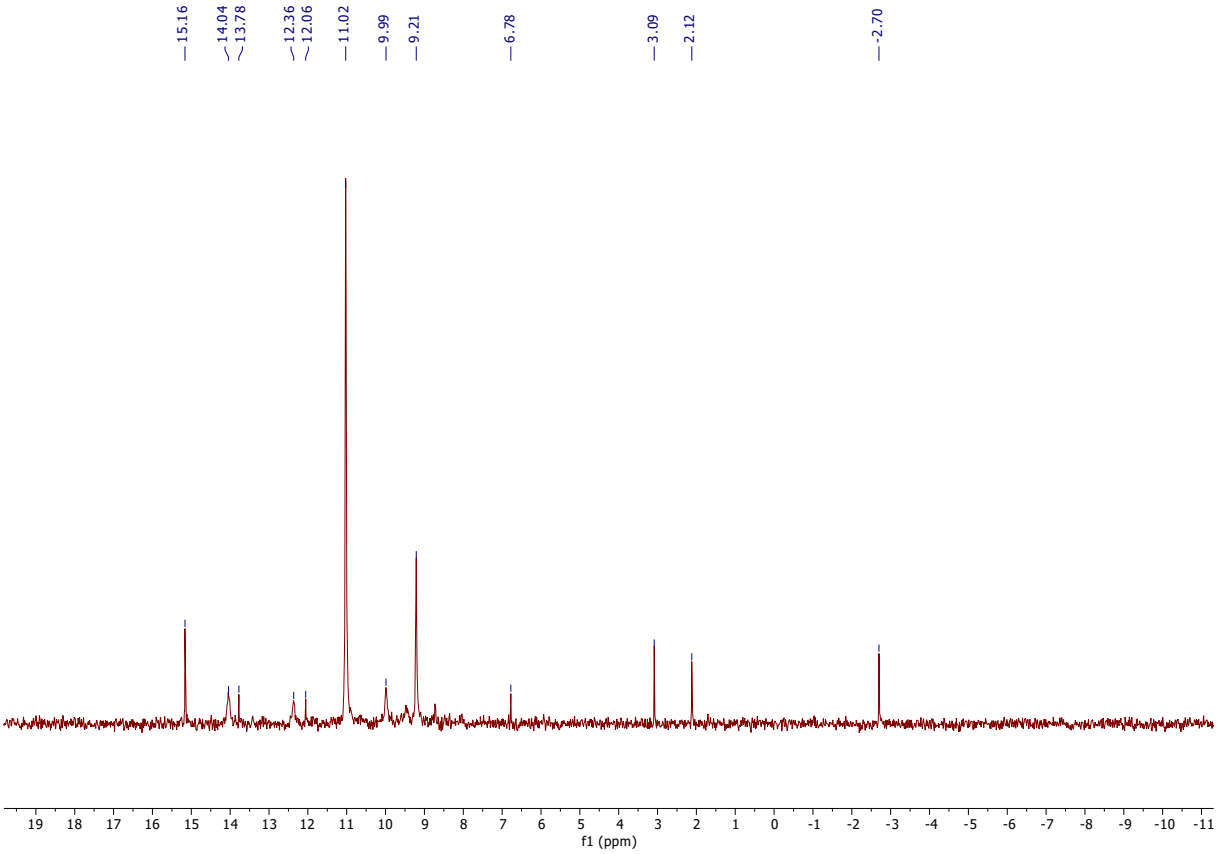

*Figure S 45: ^{31}P NMR (101 MHz, $CDCl_3$) of crude **15***

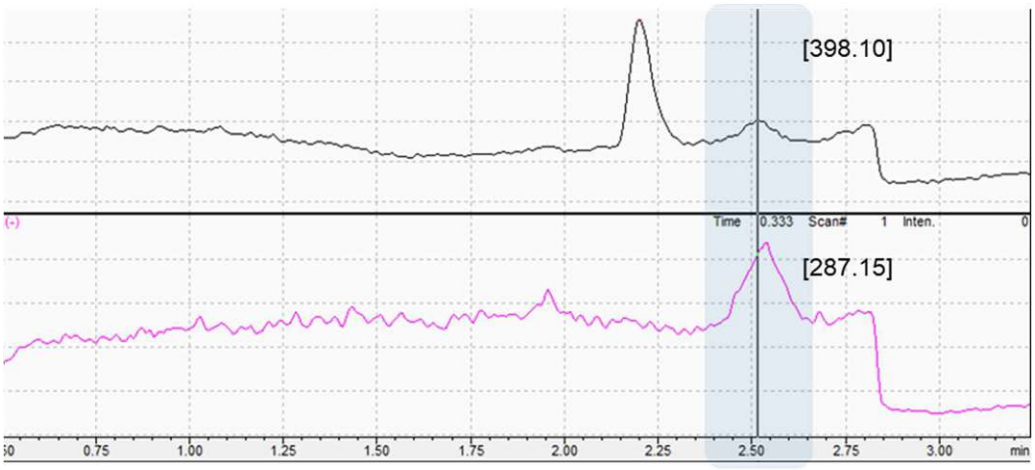

*Figure S 46: UPLC-MS of the crude product **15***

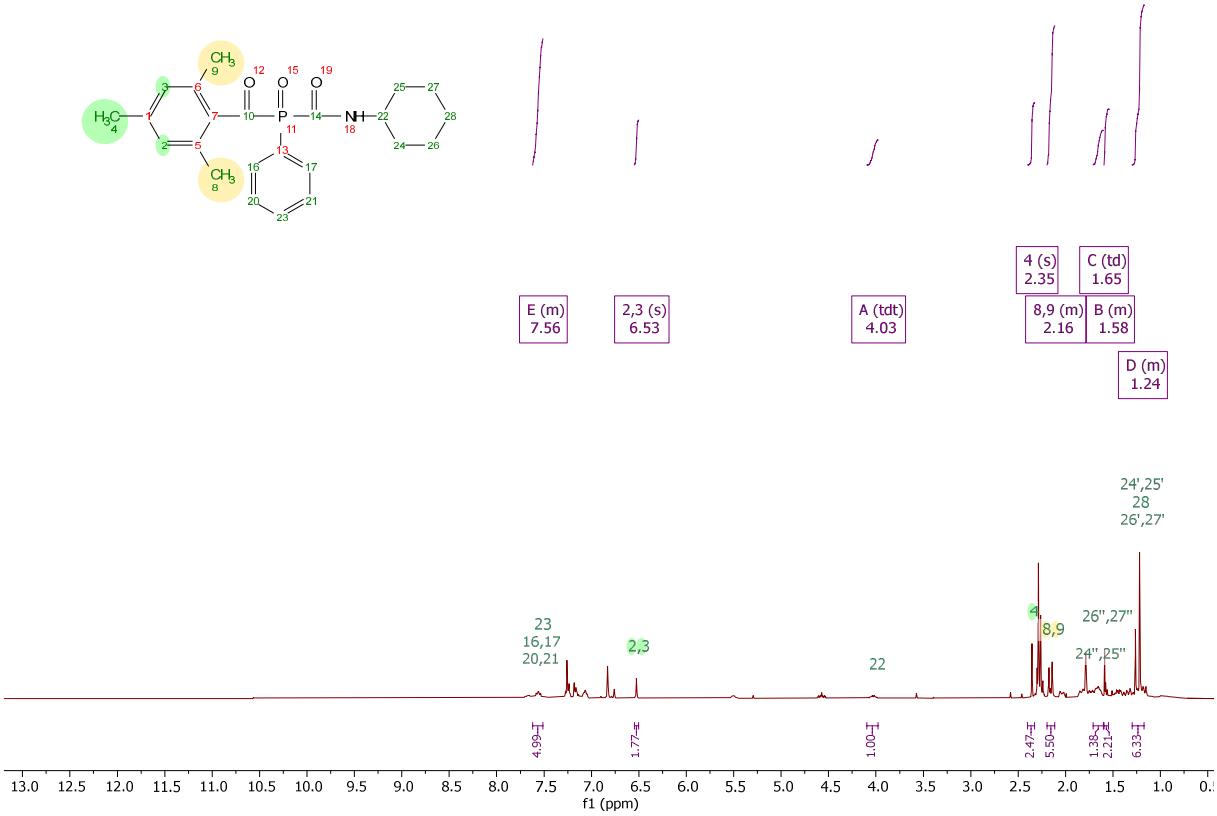

*Figure S 47: ^{1}H NMR (400 MHz, $CDCl_3$) of the crude product **15**.*

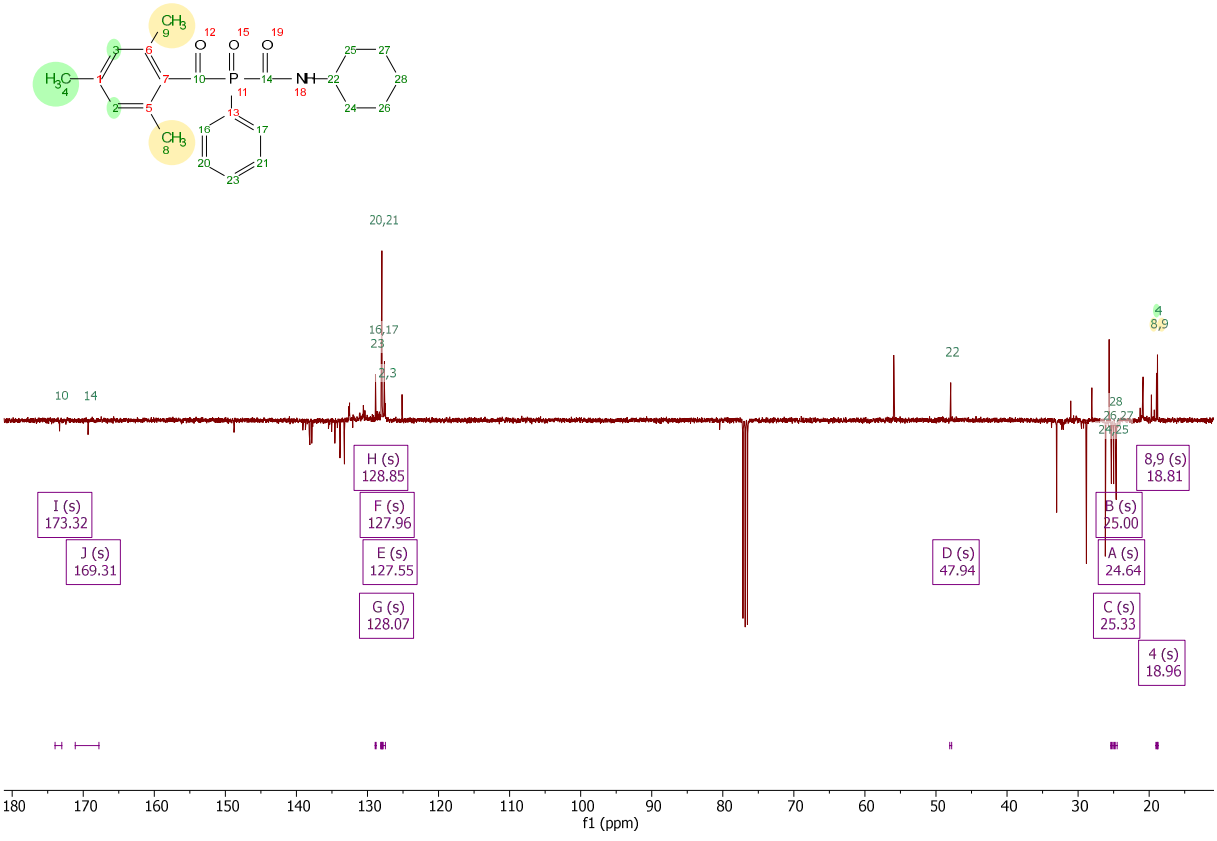

*Figure S 48: ^{13}C NMR (101 MHz, $CDCl_3$) of the crude product **15**.*

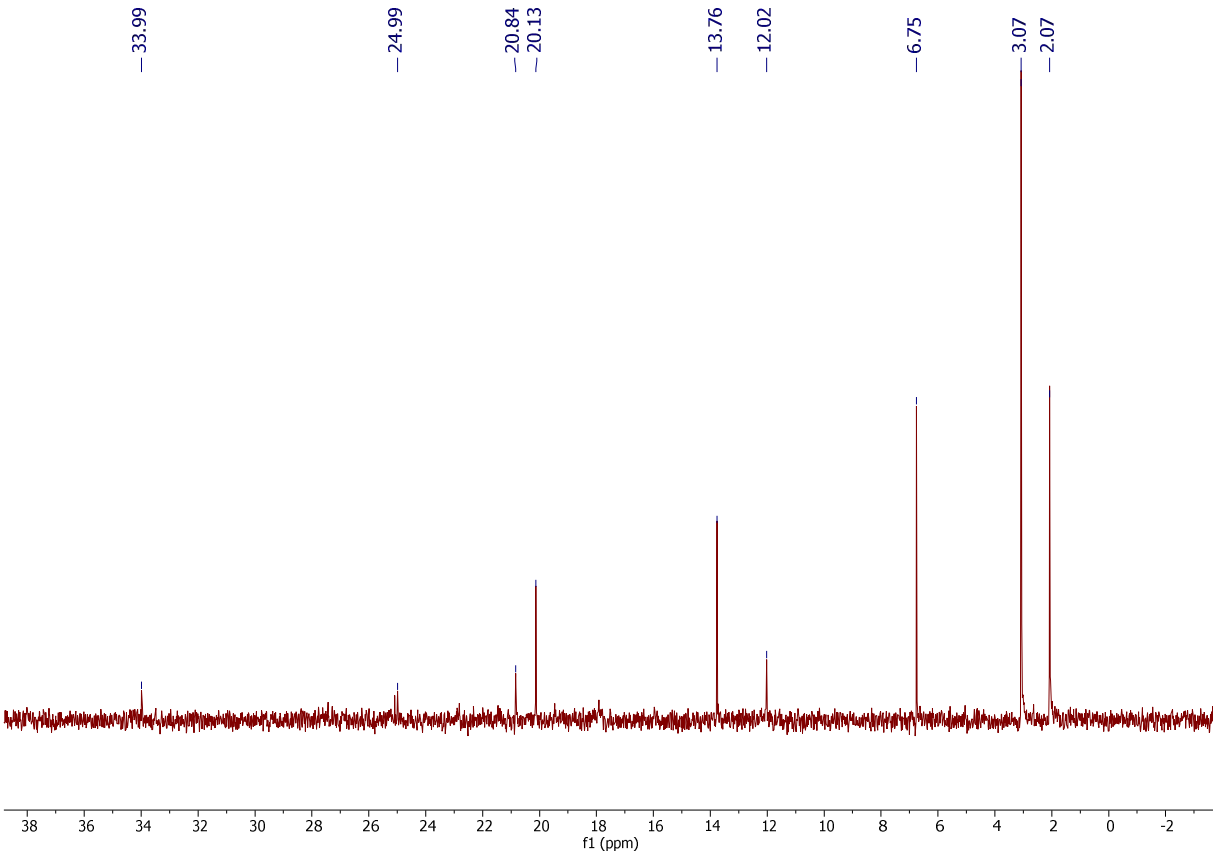

*Figure S 49: ^{31}P NMR (101 MHz, $CDCl_3$) of collected fraction **15.***

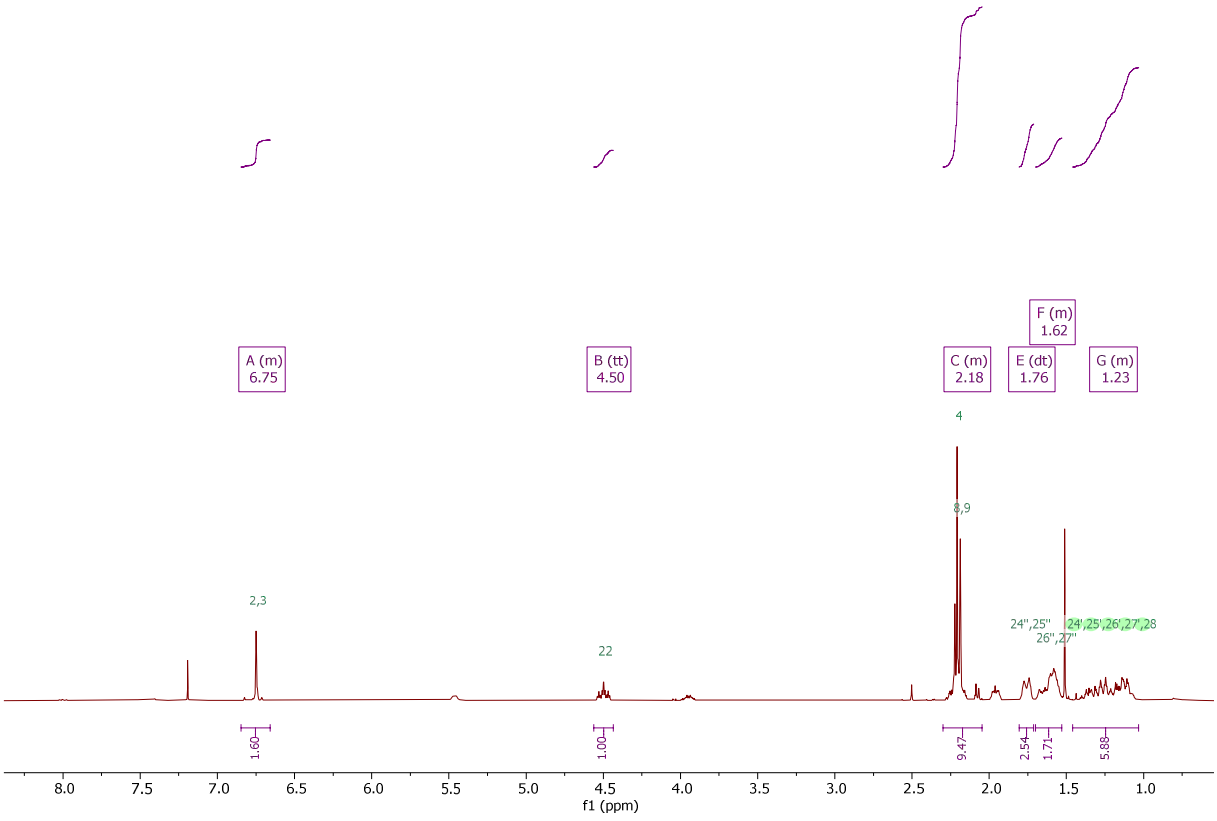

*Figure S 50: ^{1}H NMR (400 MHz, $CDCl_3$) of collected fraction **15.***